

**Equation of state of porous materials and hydrodynamics
applications**

By

Bishnupriya Nayak

PHYS01201104010

Bhabha Atomic Research Centre, Trombay, Mumbai

*A thesis submitted to the
Board of Studies in Physical Sciences*

*In partial fulfillment of requirements
for the Degree of*

DOCTOR OF PHILOSOPHY

of

HOMI BHABHA NATIONAL INSTITUTE



August 2017

STATEMENT BY AUTHOR

This dissertation has been submitted in partial fulfillment of requirements for an advanced degree at Homi Bhabha National Institute (HBNI) and is deposited in the Library to be made available to borrowers under rules of the HBNI.

Brief quotations from this dissertation are allowable without special permission, provided that accurate acknowledgement of source is made. Requests for permission for extended quotation from or reproduction of this manuscript in whole or in part may be granted by the Competent Authority of HBNI when in his or her judgment the proposed use of the material is in the interests of scholarship. In all other instances, however, permission must be obtained from the author.

Bishnupriya Nayak

DECLARATION

I, *Bishnupriya Nayak*, hereby declare that the investigation presented in the thesis has been carried out by me. The work is original and has not been submitted earlier as a whole or part for a degree/diploma at this or any other Institution/University.

Bishnupriya Nayak

To my parents and my brothers

ACKNOWLEDGEMENTS

I would like to express my gratitude to **Dr. D.M. Gaitonde** for his advice, encouragement and constant support at each stage of my Ph.D. studies during the last six years.

I am deeply grateful to **Director of Bhabha Atomic Research Centre, K.N. Vyas** for his kind support in completing the thesis.

It is an honour for me to thank **Dr. T. C. Kaushik, Dr. Dibyendu Das, Dr. K. D. Joshi, Dr. P. Modak** for their insightful comments and time to improve the coherence of the thesis. I am grateful to **Dr. G. Kondayya** for his useful suggestions and strong support. I sincerely thank **Dr. Saibal Basu**, former Dean and **Dr. B. K. Nayak**, present Dean of Physical and Mathematical sciences, HBNI for their help.

I am grateful to my thesis reviewers **Prof. Kunihiro Nagayama** and **Prof. Manjit Singh** for their valuable comments.

It is difficult to overstate my gratitude to **Dr. S.V.G. Menon** for his academic rigour, invaluable guidance, time, patience, wealth of experience. He is an incredible reservoir of knowledge. I have learned so much from him and one could not wish for a better guide. With his enthusiasm, inspiration, and his immense knowledge to explain things clearly and simply, he made **equation of state (EOS)** a joyful topic for me.

I wish to express my warm thanks to all of my friends for their suggestions. I am also indebted to the faculty and staff of Theoretical Physics Division, Bhabha Atomic Research Centre, for providing a stimulating and lively environment in which to learn and grow.

I owe my deepest gratitude to **my parents and my brothers** for their endless love, constant support and continuous encouragement. To them, I dedicate this thesis. I wish to thank my entire family for providing a loving and wonderful environment for me.

LIST OF PUBLICATIONS

Publications related to Thesis

1. B. Nayak, S.V.G. Menon, "Explicit accounting of electronic effects on the Hugoniot of porous materials", **J. Appl. Phys.** **119**, 125901 (2016).
2. B. Nayak, S.V.G. Menon, "Non-equilibrium theory employing enthalpy-based equation of state for binary solid and porous mixtures", **Shock Waves** **28** (2018) 141-151.
3. B. Nayak, S.V.G. Menon, "Generalized enthalpy based equation of state for multi-component mixtures", **AIP Advances** **7**, 045113 (2017).
4. B. Nayak and S. V. G. Menon, "Enthalpy-based equation of state for highly porous materials employing modified soft sphere fluid model", **Physica B: Physics of Condensed Matter** **529** (2017) 66-72.
5. B. Nayak and S. V. G. Menon, "Numerical simulation of shock propagation in porous materials using enthalpy-based equation of state", (To be Submitted in **J. Phys. D: Applied Physics**).
6. B. Nayak, "Expansion of dense plasma generated by shock waves in highly porous materials", **National Symposium on Plasma Science & Technology (PLASMA 2017)**.

Other Publications

1. B. Nayak and S. V. G. Menon, "Thermonuclear burn of DT and DD fuels using three-temperature model: Non-equilibrium effects", **Laser and Particle Beams** **30**, 517-523 (2012).
2. B. Nayak, "Reactivities of Neutronic and Aneutronic Fusion Fuels", **Annals of Nuclear Energy** **60**, 73-77 (2013).
3. B. Nayak and S. V. G. Menon, "Estimation of critical burn-up parameter for D-T fuel using three-temperature model", **DAE-BRNS National Laser Symposium** (2010).

ABSTRACT

Response of porous materials to impact loading is a research topic of current interest in various applications such as shock wave attenuation, ignition and detonation in energetic materials etc. Therefore, theoretical, numerical and experimental analyses have been carried out to study shock compression processes in porous substances. These processes require knowledge of equation of state (EOS) to predict the thermodynamic properties of the compressed material. A generalized enthalpy-based EOS model, including thermal contribution of electrons, from thermodynamic definitions is developed. The model shows significant difference in Hugoniot data with and without electronic contribution. We have developed an EOS model, which assumes equilibrium pressure and material velocity but non-equilibrium thermal effects, for binary mixtures by incorporating proper averaging of zero temperature isotherm and ionic enthalpy parameters for individual components. The binary mixture EOS is applied to metallic mixtures, mixtures of dissimilar solids and porous mixtures, and the results agree well with experimental data. The treatment of porous binary mixtures within the enthalpy-based EOS and single component criteria to obtain non-equilibrium temperatures in binary mixtures are done for the *first time*. An EOS model for multi-component mixtures, employing enthalpy-based approach, is proposed for the *first time*. Hugoniot parameters obtained from this model, for epoxy based composites, match well with existing experimental data. A modified soft sphere model for fluid phase is developed to apply generalized enthalpy-based EOS to higher porosities (porosity ≥ 3) when the compressed volume is higher than initial volume V_0 . The liquid-vapour co-existence curve of copper obtained from the model agrees with those from detailed molecular dynamics simulations. Also, we have modelled the effect of energy loss from shock, which occurs due to expansion of the shocked vapour, as a PdV term for the *first time*. The new model is applied to copper as prototype and accurate results are obtained in a wide range of porosity i.e. from 2 to 10. Also, numerical simulation of shock wave propagation in porous materials is done using enthalpy-based EOS. For solving all the three conservation equations i.e. mass, momentum and energy, flux corrected algorithm (which is monotone, conservative, positivity preserving algorithm, and also accurate up to 2nd order with time step) is implemented rather than the conventional finite difference approximation. Initial pressure rise, peak pressure and shock duration are accurately modelled in the simulation for the *first time*. The pressure-particle velocity curves obtained from simulation match well with experimental data. The peak pressure and shock velocity attenuate fast in porous solids, which is consistent with the theory.

SYNOPSIS

Introduction

Response of porous materials to impact loading is a research topic of current interest in various applications such as shock wave attenuation, ignition and detonation in energetic materials (e.g. porous granular explosives), synthesis of high performance materials, etc. Porous materials are extensively used in shock absorption and isolation applications due to their ability to mitigate shock pressure. The presence of the pores makes them good energy absorbers. Recent experimental studies have demonstrated pressure attenuates by 10-50 % when a shock wave travels through materials with even low porosity and hence these substances are potential candidates for light weight armor applications [1]. There are also other applications in material synthesis where porosity of the mixture is important. Therefore, theoretical and numerical analyses have been carried out to study shock propagation phenomena in porous substances at both continuum and particle levels. To describe these phenomena, knowledge of thermodynamic properties of the material is necessary. In order to predict the thermodynamic properties of the compressed material, which can be in solid, liquid or vapour phase, wide range equation of state (EOS) of the material is essential. The EOS is a thermodynamics relation between specific volume (V), temperature (T), pressure (P). A complete EOS also needs specific internal energy (E) expressed in terms of V and T . This is required to calculate several response functions like specific heats, Gruneisen parameter, etc. Generally, EOS can be represented as a combination of three components *i.e.* elastic or zero temperature isotherm, ionic thermal part and electronic thermal part. The contribution of electrons is also present in the zero temperature isotherm. High pressure EOS models for solids are well developed in comparison to that for porous materials.

Shock compression of porous materials involves three phases: a) elastic compression phase, b) plastic deformation or pore collapse phase and c) compression phase. *Elastic* deformation of material occurs under low pressure (or stress). This type of deformation involves only stretching or compression of the atom-atom bonds and hence the material returns to its original shape when the load is removed. When applied pressure is higher than the elastic limit, material is permanently deformed due to *plastic* deformation. In this phase the specific volume change is more due to collapse of pores. Finally, collapse of pores and overall compression increases the specific internal energy to a large extent. As a consequence, temperature of the substance increases appreciably. The specific volume of the matrix material reduces significantly in *compression* phase with higher applied pressure.

Porous materials are characterized by initial porosity α_0 , defined as the ratio of its initial specific volume (V_{00}) to initial specific volume of matrix material (V_0). When shock propagates in a porous material a large amount of heat is generated due to collapse of the pores. As a result, (*e.g.* when $\alpha_0 \geq 2$ for Cu) the compression curve shows anomalous behavior, wherein volume increases with increase in pressure rather than decreasing. So, pressure becomes multi-valued, i.e. multiple pressure values occur corresponding to the same specific volume in the Hugoniot curve (which is the locus of all the shocked states). The anomalous compressibility was first observed experimentally by Krupnikov and Kormer [2, 3]. Zeldovich and Raizer qualitatively showed that there is a limiting porosity beyond which the slope of the P-V Hugoniot curves change from negative to positive [4]. Kormer *et al* proposed a three term EOS consisting of zero temperature isotherm, ion thermal effects and electron thermal part such that different phases (solid, liquid and gas) are accounted approximately. This approach showed the anomalous behavior, however, several parameters need to be tuned to match experimental Hugoniot data. P- α model describes the dynamic compaction and compression of the porous material using same

EOS for both solid and distended phases [5]. Similarly, there are other approaches like the model of Carroll and Holt, Mie-Grüneisen EOS, *etc.*, to predict the behavior of shock compression of porous materials. These constitutive models *do not explain satisfactorily* the anomalous compressibility observed in Hugoniot. Thermodynamic modeling with specific volume and temperature as independent variables fails in describing the anomalous behavior.

Zubarev *et al* proposed a model along an isobaric path, where the specific internal energy (E) is related to specific volume (V) through a parameter η , to predict the Hugoniot of distended materials. Although they realized the need to treat pressure as independent variable, the significance and variation of η with P are not accounted in their work [6]. A similar approach is developed by Wu and Jing from thermodynamic considerations[7]. Their model, known as enthalpy-based EOS, relates specific enthalpy (H) and specific volume (V) through a material parameter χ which is a function of pressure. These authors computed χ using Grüneisen parameter and experimentally determined Hugoniot of the solid. Thus their aim was to extrapolate the solid Hugoniot to porous states. Viljoen *et al* simplified the method of calculating χ parameter, however, they omitted the Hugoniot elastic limit (HEL) and compaction regime (i.e., $V_{00} \geq V \geq V_0$). Their method was applied for Cu up to porosity 4 [8].

Huayun *et al* extended the method by splitting the enthalpy parameter (χ) into ionic (χ_i) and electronic (χ_e) components to account for thermal electronic effects explicitly [9]. However, their approach contain several errors [10], which may be summarized as follows. Total specific volume V of the compressed state has contributions from: (i) zero temperature isotherm, (ii) thermal ions and (iii) thermal electrons. Let V^* denote the first two contributions. To compute V^* , these authors assumed, a priori, that the fraction of specific enthalpy on the Hugoniot associated with ions is: $H^*/H = (V_{00} + V^*)/(V_{00} + V)$, where

H is total specific enthalpy and V total specific volume. While specific internal energy on the Hugoniot is partitioned between ions and electrons, this assumption has no justification. Then, they expressed thermal specific enthalpy of electrons as $H_{te}(V^*, T)$ where as it should be taken as $H_{te}(P, T)$. Further, in lieu of the correct weighting of χ_i and χ_e with constant pressure specific heats, they invoked arithmetic averaging of χ_i^{-1} and χ_e^{-1} , again, devoid of any reasoning. These observations provided the initial motivation for the research work.

Objectives of the study

- Development of a generalized enthalpy-based EOS, including explicit accounting of electronic effects, from general thermodynamic definitions.
- Extension of the EOS for binary solid and porous mixtures, together with non-equilibrium thermal effects in the components. While pressure and material velocity equilibrate fast between components, thermal energy equilibrates much slowly.
- Further development of the EOS for applications to multi-component mixtures ($N \geq 3$), *e.g.* epoxy based composites, which also have slight porosity.
- Development of the enthalpy-based EOS employing a modified soft sphere model for the fluid phase. For higher porosities, the shocked states lie in the fluid phase where final specific volume V is greater than V_0 .
- Analysis of dynamic behavior of materials under shock loading, employing the enthalpy-based EOS and a 1-D hydrodynamic code using the flux corrected transport (FCT) algorithm.

Overview of the thesis

Chapter 1 begins with a general introduction, explaining important applications of porous materials and the different phases involved in its shock compression. Earlier EOS models, research objectives, and brief description of research work are also covered.

In chapter 2, we derive a generalized enthalpy-based EOS, including electronic effects, from thermodynamic definitions: $(\partial V/\partial T)_P = (\chi/P)C_P$ and $(\partial H/\partial T)_P = C_P$, where C_P is constant pressure specific heat and χ is the effective enthalpy parameter. Now, χC_P and C_P contain thermal ionic and electronic effects and can be expressed as: $\chi C_P = \chi_i C_{P_i} + \chi_e C_{P_e}$ and $C_P = C_{P_i} + C_{P_e}$, where χ_i and χ_e are ionic and electronic enthalpy parameters and C_{P_i} and C_{P_e} are the constant pressure specific heats, respectively. The temperature dependence of χ_i is weak as illustrated in Fig. 2.1 for Cu, whereas χ_e is a constant in the range 0.37-0.44. We note that χ_i starts from small values at low pressures and approaches a value of about 0.32 around 200 GPa and remains fairly constant thereafter. The generalized enthalpy-based EOS requires temperature along Hugoniot to calculate thermal electron specific enthalpy H_{te} . So, specific volume V on the Hugoniot and temperature T are determined simultaneously, the latter using a finite difference method to solve the differential equation for temperature. Fig. 2.3 compares P-V curves for Cu for $\alpha_0=2$, with and without thermal electron terms. The initial specific volume $V_{00} \sim 0.224 \text{ cm}^3$ is compacted to solid specific volume $V_0 \sim 0.112 \text{ cm}^3$ with pressure less than 3 GPa. Electronic terms begins to contribute to the Hugoniot at around 50 GPa. The experimental data compares much better when electronic effects are added. At 0.09 cm^3 there is about 25 % increase in pressure (~ 300 to ~ 380 GPa) due to electronic contributions. This difference increases with pressure due to further thermal ionization and saturates only when Cu is fully ionized. The insert figure compares temperature on the

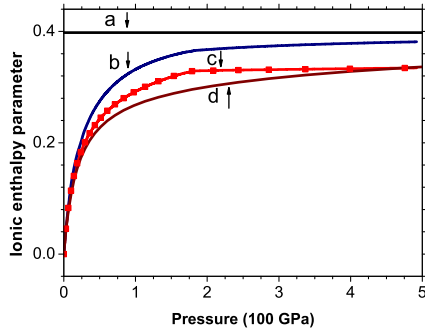


Figure 1: Variation of ionic enthalpy parameter χ_i with pressure for Cu. (a) $\chi_e = \Gamma_e / (\Gamma_e + 1)$ with $\Gamma_e = 0.66$. (b) Effective χ obtained using C_P weighting. (c) χ_i obtained from 3-component EOS model. (d) $\chi_i = P\Gamma_s/B_s$ obtained on Li's zero temperature isotherm [10].

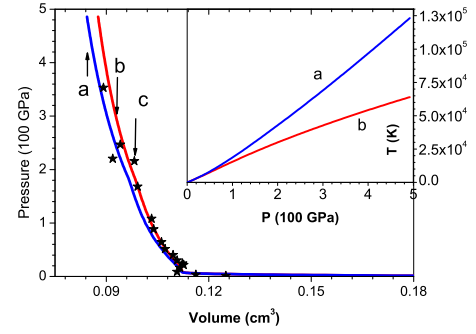


Figure 2: Comparison of P-V Hugoniot of Cu with porosity, $\alpha_0 = 2$. (a) Without electronic contribution. (b) With electronic contribution. (c) Experimental data [11]. Inset figure shows temperature on the Hugoniot. (a) Without electronic effects. (b) Including electronic effects [10].

Hugoniot with and without electronic contribution. The latter produces a dramatic reduction in temperature, e.g., by a factor of two for pressure ~ 300 GPa. This is due to the generation of more free electrons via thermal ionization and consequent increase in specific heat. We have used a three component EOS to calculate χ_i , electronic specific enthalpy H_{te} , and specific heats C_{Pi} and C_{Pe} . This consists of Li's 4-parameter zero temperature model, Cowan's ion model and McCloskey's parametrization of Thomas-Fermi calculations for electronic contributions. Further results on P-V curves and $U_s - U_p$ relations obtained from our approach match well with experimental data. Errors involved in earlier attempts by Huayun *et al* are also discussed in this chapter. The correct way to account electronic effects explicitly, and its applications, are *new* developments.

In chapter 3, we extend the EOS model to binary solid and porous mixtures by proper averaging of zero temperature isotherms and ionic enthalpy parameters. The model accounts for non-equilibrium temperatures in the components, and also includes electron thermal effects. This enthalpy-based EOS is well suited for mixtures because pressure equilibration is fast. We used the

finite-strain Birch-Muraghan formula for elastic component, and computed ionic enthalpy parameters along the zero temperature isotherm. Additionally, we employed a simple thermal model for ionic thermal specific enthalpy, defined by $E_{ti} = C_{Vi}(T - T_0)$ where T_0 is the ambient temperature. The formulation leads to an extra term in the expression for specific volume $V(P, T)$, which arises because of difference in specific enthalpies of ionic components. The mixture Hugoniot and equilibrium temperature in mixture are then readily obtained. We also proposed the *single component criteria* for obtaining non-equilibrium temperature in the components, which are then compared with equilibrium temperatures. The method is applied to obtain various Hugoniot parameters (i.e. P-V curves, T-P curves and U_s - U_p curves) for several types of materials: (i) metallic mixtures (tungsten-copper, iron-nickel), (ii) mixtures of compounds (calcite-water, paraffin-tungsten), and (iii) a porous mixture (tantalum carbide-carbon), with varying weight fractions. Results agree well with existing experimental data, which also include the slight initial curvature in U_s - U_p curves due to different compressibility of components. Our model also shows that temperatures of TaC-C porous mixture are much higher than in other mixtures due to effect of porosity. Development of the enthalpy-based binary mixture theory is *new*. Also, we used the *single component criteria* to obtain non-equilibrium temperatures for the *first time*.

Chapter 4 describes the EOS model for multi-component mixtures, and is a generalization of the formulation discussed above to arbitrary number of components. Here, we have employed a more accurate zero temperature isotherm for applications. We also have invoked the *single component criteria* to compute non-equilibrium temperatures of individual components. The thermal model is the same as mentioned above, i.e., $E_{ti} = C_{Vi}(T - T_0)$, because the pressures involved in the experimental data are low. The method is applied to two and three component epoxy based composite materials (Al_2O_3 -epoxy, Al-MnO₂-epoxy, Al-Fe₂O₃-epoxy). Last case has porosity of about 15 %. Our

approach provides much better agreement in comparison to earlier attempt by Zhang *et al*, which simply uses average zero temperature isotherm and thereafter follows the single component theory. The new term which arises due to ionic specific enthalpy differences becomes more important in multi-component mixtures. This gives 2-3 % difference in P-V curves for the epoxy based mixtures. This formulation and applications for a mixture with arbitrary number of components are *new* contributions.

In chapter 5, we have developed a modified soft sphere model for the fluid phase for applying the enthalpy-based EOS to higher porosities, *e.g.* $\alpha_0 > 2$ for Cu. The final shocked states in such cases lie in the fluid phase, *i.e.* the compressed specific volume V is higher than initial specific volume V_0 . Modification of the soft sphere model (originally due to Hoover *et al*) is mainly in the determination of all its parameters in terms of three experimental data, *viz.*, density, cohesive energy and bulk modulus of the solid at normal conditions. It also contains all the three EOS components, *i.e.* zero temperature, thermal ionic and thermal electronic terms. Isotherms obtained for Cu show the familiar van der Waals loops. The liquid-vapor co-existence curve of Cu obtained from the model is in good agreement with that determined from detailed molecular dynamics simulations. In applications to highly porous cases, we also introduced the effect of energy loss (as a term $-P \Delta V_m$) from shock that arises due to expansion of the shocked material to final specific volume. This has been observed experimentally in polystyrene. For Cu with $\alpha_0 = 2$, $\Delta V_m \sim 0$ since most of the shocked states are close to V_0 . Thereafter it increases linearly with porosity, indicating more expansion, but shows a saturating trend for higher α_0 . We expect this variation to be typical for other materials also. These values of ΔV_m have been deduced from the P-V curves. Finally, U_s-U_p curves and T-P curves are obtained for a wide range of initial porosity from 2 to 10. These results compare much better with existing experimental data as compared to all earlier calculations [10], which did not use models corre-

sponding to fluid phase. Our modification to soft sphere model, its use in the enthalpy-based EOS, and accounting for energy loss due to vapor expansion are all *new* developments.

In chapter 6 we study shock propagation via numerical simulations of the Euler equations describing conservation laws of mass, momentum and energy. The propagation of shock generates hydrodynamic motions in materials. As a consequence, the state variables such as density, pressure, specific internal energy, particle velocity etc., change in space and time. We numerically simulate shock propagation using Euler equations and EOS of the material. The approach we have implemented uses the Flux-Corrected Transport (FCT) algorithm to solve a system of coupled non-linear conservation equations [12]. FCT algorithm accommodates minimum numerical diffusion, and preserves monotone, conservative and positivity properties. It has 2^{nd} order accuracy with respect to time differencing. The algorithm does the simulation in two stages: a convective stage followed by an anti-diffusive stage. Details of mesh generation, discretization of continuity equations, boundary conditions, etc, are described in this chapter. We simulated impact experiments (Cu-impactor+Cu-target) employing Mie-Gruneisen EOS for normal solid and enthalpy-based EOS for porous substances. The simulation consisted of placing the target plate adjacent to the impactor, and specifying the impact velocity in all the meshes within the impactor. Initial pressure rise, peak pressure and shock duration are accurately modeled in the simulation and the pressure-time profiles compare well with experimentally measured data. Pressure vs. particle velocity curves of Cu obtained from simulation for various porosities match well with experimental data. Also, we show that the peak pressure and shock velocity attenuate fast for porous Cu even with low porosity like 1.1 and 1.3. This approach has great potential to predict shock wave parameters in porous materials. Our implementation of enthalpy-based EOS in numerical simulation is *new*.

Finally, chapter 7 of the thesis summarizes the work, discusses existing issues and possible directions for future research in this field.

- [1] K. Kitagawa, et al., "Attenuation Properties of Blast Wave Through Porous Layer", *Shock Waves*, 26th International Symposium on Shock Waves, Vol-1, 73-78, (2009).
- [2] K. K. Krupnikov, M. I. Brazhnik, and V. P. Krupnikova, *Sov. Phys. JETP*, **15**, 470, (1962).
- [3] S. B. Kormer, A. I. Funtikov, V. D. Urlin, and A. N. Kolesnikova, "Dynamic compression of porous metals and the equation of state with variable specific heat at high temperatures.", *Sov. Phys. JETP*, **15**(3), 477-488, (1962)
- [4] Ya.B. Zel'ovich and Yu. P. Raizer, "Physics of Shock Waves and High-Temperature Hydrodynamic Phenomena", Vol-II, Academic press, New York and London (1967).
- [5] W. Hermann, *J. Appl. Phys.*, **40**, 2490, (1969)
- [6] R.F. Trunin, "Shock Compression of Condensed Materials", Cambridge university press (1998).
- [7] Q. Wu and F. Jing, "Thermodynamic equation of state and application to Hugoniot predictions for porous materials.", *J. Appl. Phys.*, **80**(8), 4343-4349, (1996).
- [8] L. Boshoff-Mostert and H. J. Viljoen, "Comparative study of analytical methods for Hugoniot curves of porous materials", *J. Appl. Phys.*, **86**(3), 1245-1254, (1999).

- [9] Geng Huayun, Wu Qiang, Tan Hua, Cai Lingcang, and Jing Fuqian, J. Appl. Phys., **92**, 5917 (2002); J. Appl. Phys., **92**, 5924, (2002).
- [10] B. Nayak, S.V.G. Menon, J. Appl. Phys. **119**, 125901 (2016).
- [11] <http://www.ihed.ras.ru/rusbank/>
- [12] J. P. Boris, A. M. Landsberg, E. S. Oran and J. H. Gardner, "LCPFCT Flux-Corrected Transport Algorithm for Solving Generalized Continuity Equations", NRL/MR/6410-93-7192, NAVAL RESEARCH LABORATORY, (1993).

Contents

SYNOPSIS	viii
1 Introduction	1
1.1 Motivation	1
1.1.1 Equation of state	2
1.2 Background	4
1.2.1 Dynamic compaction of porous materials	4
1.2.2 Earlier models for porous substances	5
1.3 Research objective	14
1.4 Outline of thesis	15
2 Explicit accounting of electronic effects on the Hugoniot of porous materials	19
2.1 Introduction	19
2.2 Generalized enthalpy-based EOS	21
2.3 Porous Hugoniot	22
2.3.1 Numerical method	24
2.3.2 Method of Huayun <i>et al</i>	25
2.3.3 Three Component EOS	26
2.3.4 Calculation of χ_i , C_{Pi} , C_{Pe} and H_{te}	30
2.4 Results	31
2.5 Summary	35
3 Non-equilibrium theory employing enthalpy-based equation of state for binary solid and porous mixtures	37
3.1 Introduction	37

3.2	Generalized enthalpy-based EOS for binary mixtures	40
3.2.1	Individual component EOS	40
3.2.2	Binary mixture EOS	42
3.3	Binary mixture Hugoniot	44
3.3.1	Other approaches	45
3.3.2	Determination of temperature in binary mixture	47
3.3.3	Numerical method	48
3.4	Applications	48
3.4.1	EOS model	48
3.4.2	Metallic mixtures	51
3.4.3	Mixtures of compounds	52
3.4.4	Porous mixture	58
3.5	Summary	60
4	Generalized enthalpy-based equation of state for multi-component mixtures	62
4.1	Introduction	62
4.2	Generalized enthalpy-based equation of state for multi-component mixtures	65
4.3	Multi-component mixture Hugoniot	67
4.3.1	Single component criteria	69
4.3.2	Determination of temperature in mixture	70
4.3.3	Numerical technique	71
4.4	EOS models	71
4.5	Results	72
4.6	Summary	76
5	Enthalpy-based equation of state for highly porous materials employing modified soft sphere fluid model	81
5.1	Introduction	81
5.2	Enthalpy-based equation of state	83
5.2.1	Specific volume and temperature on Hugoniot	85
5.3	Modified soft sphere model	87
5.3.1	Generalized Lennard Jones model	88
5.3.2	Energy parameters and exponents	89

5.3.3	Total energy and pressure	91
5.4	Results and discussion	92
5.4.1	Ionic enthalpy parameter	92
5.4.2	Vapor-liquid phase diagram	94
5.4.3	Porous Hugoniot	96
5.5	Summary	100
6	Numerical simulation of shock propagation in porous materials using enthalpy-based equation of state	101
6.1	Introduction	101
6.2	Euler's conservation equations	103
6.2.1	Eulerian scheme	103
6.2.2	Lagrangian scheme	103
6.3	FCT Numerical Algorithm	104
6.3.1	Flux correction scheme	106
6.3.2	Two stage time integration	106
6.3.3	Difference equations	107
6.3.4	Boundary conditions	110
6.4	Equation of state	111
6.4.1	Mie-Grüneisen EOS	111
6.4.2	Enthalpy-based EOS	112
6.4.3	Explicit accounting of electronic effects	114
6.5	Simulation of impact experiments	115
6.5.1	Soild Cu experiment	116
6.5.2	Shock propagation in Soild Cu	116
6.5.3	Shock attenuation in Cu with 1.1 porosity	118
6.5.4	Shock attenuation in Cu with 1.3 porosity	119
6.5.5	Shock pressure vs. fluid speed	119
6.6	Summary	120
7	Conclusions and future work	122
7.1	Concluding remarks	122
7.2	Future scope	124
	Bibliography	125

List of Figures

1	Variation of ionic enthalpy parameter χ_i with pressure for Cu. (a) $\chi_e = \Gamma_e/(\Gamma_e+1)$ with $\Gamma_e = 0.66$. (b) Effective χ obtained using C_P weighting. (c) χ_i obtained from 3-component EOS model. (d) $\chi_i = P\Gamma_s/B_s$ obtained on Li's zero temperature isotherm [10].	xiii
2	Comparison of P-V Hugoniot of Cu with porosity, $\alpha_0 = 2$. (a) Without electronic contribution. (b) With electronic contribution. (c) Experimental data [11]. Insert figure shows temperature on the Hugoniot. (a) Without electronic effects. (b) Including electronic effects [10].	xiii
1.1	Potential energy vs. specific volume curve	3
1.2	Various phases occurring in compression curve for a porous material, taken from [1]. ρ_e is the final density achieved after applying the pressure p_e in the elastic compression phase and ρ_c is the final density achieved due to pressure p_c in the pore collapse phase.	5
1.3	Multivaluedness in pressure (P_1 and P_2) occurs in Hugoniot for Cu when $\alpha_0 \geq 2$	6
1.4	Hugoniot curves for different initial porosities. (a) Vertical dashed line represents limiting case i.e. $\alpha_\infty = 1 + 2/\Gamma_0$, (b) α_{01}, α_{02} refer to low porous solid, (c) α_{03}, α_{04} are high porosity cases.	7
1.5	Hugoniot curves for a very low porous material (red line), obtained from snow plow model, and for a normal solid (blue line).	8
1.6	Dynamic compression of porous solid using P- α compaction model, taken from [2]	10

2.1	Variation of ionic enthalpy parameter with pressure for Cu. (a) $\chi_e = \Gamma_e / (\Gamma_e + 1)$ with $\Gamma_e = 0.66$. (b) Effective χ obtained using C_P weighting (see text below Eq. (2.8)). (c) χ_i obtained from 3-component EOS model. (d) $\chi_i = P\Gamma_s / K_s$ obtained using Γ_s (see Eq. (2.22)) and zero temperature isotherm for K_s	31
2.2	Variation of electronic specific heat C_{Pe} with temperature T along the Hugoniot for Cu, using 3-component EOS model. Insert figure shows ionic specific heat C_{Pi} obtained using 3-component EOS model.	32
2.3	Comparison of P-V Hugoniot of porous Cu with porosity $\alpha_0 = 2$. (a) Without electronic contribution. (b) With electronic contribution. (c) Experimental data [3]. Insert figure shows temperature on the Hugoniot. (a) Neglecting electronic effects. (b) Including electronic effects.	33
2.4	Comparison of P-V curves of porous Cu. (a) $\alpha_0 = 1$, (b) $\alpha_0 = 2$, (c) $\alpha_0 = 3$, (d) $\alpha_0 = 4$, (e) $\alpha_0 = 7.2$, (f) $\alpha_0 = 10.03$. Symbols are experimental data [3].	34
2.5	Variation of temperature with pressure on the Hugoniot of porous Cu. (a) $\alpha_0 = 1$, (b) $\alpha_0 = 2$, (c) $\alpha_0 = 4$, (d) $\alpha_0 = 5.45$, (e) $\alpha_0 = 7.2$, (f) $\alpha_0 = 10.03$	34
2.6	Comparison of $U_s - U_p$ curves of porous Cu. (a) $\alpha_0 = 1$, (b) $\alpha_0 = 2$, (c) $\alpha_0 = 4$, (d) $\alpha_0 = 7.2$. Symbols are experimental data [3].	35
3.1	Variation of χ_{ik} with pressure for Cu, Fe, W, and Ni. χ_{ik} on the Hugoniot (curves-a). χ_{ik} obtained on the Birch-Murnagan isotherms (curves-b).	42
3.2	Ratio of enthalpy difference term to those preceding it in Eq. (3.9) for three W-Cu mixtures. $w_1/w_2 = 76/24$ (curve-a), $w_1/w_2 = 55/45$ (curve-b), $w_1/w_2 = 25/75$ (curve-c).	45
3.3	Variation of C_P with temperature along the Hugoniot of Cu, Fe, W, and Ni within the EOS model.	50
3.4	Pressure-volume Hugoniot of W-Cu mixtures. Curves from left to right are for: pure W, $w_1/w_2 = 76/24$, $w_1/w_2 = 68/32$, $w_1/w_2 = 55/45$, $w_1/w_2 = 25/75$ and pure Cu. Experimental data (symbols) are from Ref.[4].	51

3.5	Temperature-pressure curves for W-Cu mixtures. Average temperature (curve-a), temperature of Cu (curve-b), temperature of W (curve-c). Curve-a and curve-b merged together for $w_1/w_2=68/32$	52
3.6	Shock speed (U_s) vs. particle speed (U_p) for pure Cu (curve-a), pure W (curve-b), $w_1/w_2=76/24$ (curve-c), $w_1/w_2=68/32$ (curve-d), $w_1/w_2=55/45$ (curve-e), $w_1/w_2=25/75$ (curve-f). Experimental data (symbols) are from Ref.[4]. Curves b to f are shifted to right by 0.5 km/s successively for clarity.	53
3.7	Pressure-volume Hugoniot of Ni (curve-a) and Fe-Ni mixture with $w_1/w_2=74/26$ (curve-b). Experimental data (symbols) are from Ref.[4].	53
3.8	Temperature-pressure curves for Fe-Ni mixtures. Average temperature (curve-a), temperature of Fe (curve-b), temperature of Ni (curve-c).	54
3.9	Shock speed (U_s) vs. particle speed (U_p) for pure Ni (curve-a), $w_1/w_2=90/10$ (curve-b), $w_1/w_2 = 82/18$ (curve-c), $w_1/w_2 = 74/26$ (curve-d), and pure Fe (curve-e). Experimental data (symbols) are from Ref.[4]. Curves b to e are shifted to right by 0.5 km/s successively for clarity.	54
3.10	Pressure-volume Hugoniot of calcite (curve-a), calcite-water mixture with $w_1/w_2=90/10$ (curve-b), and water (curve-c). Experimental data (symbols) are from Ref.[4].	55
3.11	Temperature-pressure curves for calcite-water mixture with $w_1/w_2=90/10$. Temperature of calcite (curve-a), average temperature (curve-b), temperature of water (curve-c).	56
3.12	Shock speed (U_s) vs. particle speed (U_p) for calcite (curve-a) calcite-water mixture with $w_1/w_2=90/10$ (curve-b) and water (curve-c). Experimental data (symbols) are from Ref.[4]. Data for water (curve-c) are shifted to right by 1 km/s for clarity.	56
3.13	Pressure-volume Hugoniot of W (curve-a), paraffin-W mixture with $w_1/w_2=16/84$ (curve-b), $w_1/w_2=34/66$ (curve-c) and Paraffin (curve-d). Experimental data (symbols) are from Ref.[4]. . .	57

3.14	Temperature-pressure curves for paraffin-W mixture with $w_1/w_2=34/66$. Average temperature (curve-a), temperature of paraffin (curve-b), temperature of W (curve-c).	57
3.15	Shock speed (U_s) vs. particle speed (U_p) for W (curve-a), paraffin-W mixture with $w_1/w_2=16/84$ (curve-b), $w_1/w_2=34/66$ (curve-c) and paraffin (curve-d). Experimental data (symbols) are from Ref.[4]. Data for paraffin (curve-d), mixture (curve-c) and mixture (curve-b) are shifted to right by 1, 2, and 3 km/s for clarity.	58
3.16	Pressure-volume Hugoniot of TaC (curve-a), TaC-C mixture with $w_1/w_2=30/70$ and porosity 1.44 (curve-b), and carbon (curve-c). Experimental data (symbols) are from Ref.[5].	59
3.17	Temperature-pressure curves for TaC-C mixture with $w_1/w_2=30/70$ and porosity 1.44. Temperature of TaC (curve-a), average temperature (curve-b), and temperature of carbon (curve-c).	59
3.18	Shock speed (U_s) vs. particle speed (U_p) for TaC (curve-a), TaC-C mixture with $w_1/w_2=30/70$ and porosity 1.44 (curve-b), and carbon (curve-c). Experimental data (symbols) are from Ref.[5]. Data for mixture (curve-b) and carbon (curves-c) are shifted to right by 1 km/s, respectively, for clarity.	60
4.1	(A). Variation of χ with P for Al. (a) $\chi_e = \Gamma_e / (\Gamma_e + 1)$ with $\Gamma_e = 0.66$. (b) χ_i obtained from 3-component model [6]. (c) $\chi_i = P \Gamma_s / B_s$, where Γ_s is Gruneisen parameter of solid [7] and B_s bulk modulus, along zero temperature isotherm [6]. (B). Ratio of enthalpy difference term to those preceding it in Eq. (4.9) for two mixtures. (a.) Al-MnO ₂ -Epoxy, (b.) Al-Fe ₂ O ₃ -Epoxy.	68
4.2	Comparison of $P-U_p$ Hugoniot of single component materials, Epoxy, Al, MnO ₂ , Fe ₂ O ₃ , and Al ₂ O ₃ . Experimental data are from references [4, 5].	73

- 4.3 (A). Comparison of $P-U_p$ Hugoniot of two component mixtures of Alumina and Epoxy. (a) Al_2O_3 (0.454)-Epoxy, (b) Al_2O_3 (0.626)-Epoxy, (c) Al_2O_3 (0.708)-Epoxy. Experimental data are from references [4, 5]. (B). Temperature vs. pressure on the Hugoniot of two component mixture of Al_2O_3 and Epoxy with $w_1/w_2=0.454/0.546$. Graphs show component temperatures and average mixture temperature 75
- 4.4 (A). Comparison of $P-U_p$ Hugoniot of three component mixture of Al, MnO_2 and Epoxy with $w_1/w_2/w_3=0.251/0.537/0.212$. Experimental data are from references [4, 5] (B). Comparison of $P-U_p$ Hugoniot of three component mixture of Al, Fe_2O_3 and Epoxy with $w_1/w_2/w_3=0.126/0.374/0.5$. Experimental data are from references [4, 5]. 77
- 4.5 (A). Comparison of U_p-U_s curve of three component mixture of Al, MnO_2 and Epoxy with $w_1/w_2/w_3=0.251/0.537/0.212$. Experimental data are from references [4, 5] (B). Comparison of U_p-U_s curve of three component mixture of Al, Fe_2O_3 and Epoxy with $w_1/w_2/w_3=0.126/0.374/0.5$. Experimental data are from references [4, 5]. 78
- 4.6 (A). Temperature vs. pressure on the Hugoniot of three component mixture of Al, MnO_2 and Epoxy with $w_1/w_2/w_3=0.251/0.537/0.212$. Graphs show component temperatures and average mixture temperature. Temperatures for Al and MnO_2 are almost the same. (B). Temperature vs. pressure on the Hugoniot of three component mixture of Al, Fe_2O_3 and Epoxy with $w_1/w_2/w_3=0.126/0.374/0.5$. Graphs show component temperatures and average mixture temperature. 79

5.1	(A) Variation of χ vs. P for Cu. Curves a, b and c show χ using soft sphere model along the curves $V_1(P)$, $V_2(P)$ and $V_3(P)$ defined in the text. Curve-d shows χ along the solid Hugoniot obtained using U_s - U_p data. Inset figure shows variation of constant pressure specific heats C_{P_i} and C_{P_e} vs. temperature along $V_2(P)$. (B) Comparison of scaled cohesive energy vs. scaled inter particle distance $(V/V_0)^{1/3}$. Solid line: 4-parameter model [8], Symbols: generalized Lennard-Jones model Eq. (5.13)	93
5.2	(A) Isotherms of Cu using the modified soft sphere model: (a) $T=5000$ K, (b) $T=7000$ K, (c) $T=8236$ K and (d) $T=9000$ K. (B) Liquid-Vapor phase diagram of Cu within the modified soft sphere model. Symbols are simulation data [9]	95
5.3	(A) Pressure-volume cures $V_\lambda(P)$ defined in the text: Curves a, b, c and d depict V_{-1} , V_1 , V_2 and V_3 , respectively. (B) Percentage contribution of the enthalpy difference term in Eq. (5.8): Curves a, b and c are for $\alpha_0=3, 5$ and 7 , respectively.	97
5.4	(A) Variation of ΔV_m vs. initial porosity for Cu. (B) Comparison of pressure-volume curves of Cu for different initial porosities. (a) $\alpha_0=2$, (b) $\alpha_0=3$, (c) $\alpha_0=4$, (d) $\alpha_0=5.45$, (e) $\alpha_0=7.2$, (f) $\alpha_0=10.03$. Symbols are experimental data [3].	98
5.5	(A) Comparison of U_s - U_p curves of porous Cu. (a) $\alpha_0=2$, (b) $\alpha_0=3$, (c) $\alpha_0=4$, (d) $\alpha_0=5.45$, (e) $\alpha_0=7.2$, (f) $\alpha_0=10.03$. Curves b - f are shifted successively to right by 1 unit. Symbols are experimental data [3]. (B) Temperature vs. pressure on the Hugoniot of Cu. (a) $\alpha_0=2$, (b) $\alpha_0=3$, (c) $\alpha_0=4$, (d) $\alpha_0=5.45$, (e) $\alpha_0=7.2$, (f) $\alpha_0=10.03$	99
6.1	Simulation geometry for plate impact problems. Thicknesses of impactor and target plates are 3 mm and 20 mm, respectively, for shock attenuation calculations.	117
6.2	Pressure-time profiles: Solid lines are simulation results while symbols denote experimental data [10]. (Top) Impact velocity 0.645 km/s, (middle) Impact velocity 0.468 km/s, (bottom) Impact velocity 0.285 km/s	117

- 6.3 Attenuation of shock wave in solid-Cu of 20 mm thickness, impacted with 3 mm thick impactor with velocity 2 km/s. Pressure-time profiles are shown at different locations (see legend) from the impact surface. Note that the peak pressure remains unaltered even up to 15 mm. Negative pressure occur in the last two profiles because of the release wave reaching back from the rear surface. 118
- 6.4 Attenuation of shock wave in porous-Cu of 20 mm thickness (porosity 1.1), impacted with 3 mm thick impactor with velocity 2 km/s. Pressure-time profiles are shown at different locations (see legend) from the impact surface. Note that the peak pressure attenuates after the shock travels about 13 mm, and the shock velocity is lower compared to that in solid target. Negative pressure occur in the last profile because of the release wave reaching back from the rear surface. 119
- 6.5 Attenuation of shock wave in porous-Cu of 20 mm thickness (porosity 1.3), impacted with 3 mm thick impactor with velocity 2 km/s. Pressure-time profiles are shown at different locations (see legend) from the impact surface. Note that the peak pressure starts to attenuate after the shock travels about 7 mm, and the shock velocity is lower compared to that for porosity 1.1. Negative pressures are not visible because the shock wave and consequently the release wave are delayed. 120
- 6.6 Shock pressure vs. fluid speed in Cu. (a) normal solid, (b) porosity 1.13 and (c) porosity 1.414. Lines denote computed results while the symbols are experimental data [4]. 121

List of Tables

3.1	Material Parameters for Hugoniot calculations. Units: ρ_0 in g/cm^3 , B_0 in 100 GPa and C_V in $\text{J}/\text{g K}$	50
4.1	EOS parameters of components. ρ_0 [g/cm^3], B_0 [100 GPa] and C_V [$\text{J}/\text{g K}$]	73
6.1	Source terms in generalized continuity equation	105
6.2	Impact experiments on solid Cu	115
6.3	Material Parameters for Cu.	115

Introduction

1.1 Motivation

Porous materials are characterized by initial porosity α_0 , defined as the ratio of initial volume of porous solid (V_{00}) to initial volume of matrix material (V_0). The response of porous materials to impact loading is a research topic of current interest for various applications such as shock wave attenuation [11–14], compaction to detonation ignition in energetic materials, e.g. porous granular explosives [15–17], synthesis of high performance materials etc [18, 19]. These materials are extensively used in shock absorption and isolation applications due to their impact pressure mitigation properties. The presence of the pores makes them good absorbers. Recent experimental studies [20] have demonstrated that shock pressure attenuates by 10-50 % when a shock travels through porous solid and hence these substances are potential candidates for light weight armor applications. In addition, there are many practical applications such as shock initiation of heterogeneous explosives, attenuation of blast waves, material synthesis employing shock-induced chemical reactions, etc, in which porous mixtures are very useful. Therefore, theoretical and numerical analyses have been carried out to study shock compression processes in porous substances at both continuum and particle levels [11, 12, 15, 16, 21, 22]. For describing these phenomena, knowledge of thermodynamic properties of the medium is necessary. In order to predict the thermodynamic properties of the compressed material which either can be in solid or liquid or vapour phase, wide range of equation of state (EOS) of material is essential. High pressure EOS models for solids are well developed in comparison to that of porous materials.

1.1.1 Equation of state

The EOS is a thermodynamics relationship among specific volume (V), temperature (T), pressure (P) and specific internal energy (E) of the material under study. It can be represented as a combination of three parts or components.

$$P(V, T) = P_c(V) + P_{ti}(V, T) + P_{te}(V, T) \quad (1.1)$$

$$E(V, T) = E_c(V) + E_{ti}(V, T) + E_{te}(V, T) \quad (1.2)$$

where P_c , P_{ti} , and P_{te} are the cold or elastic component, ionic thermal component, and electronic thermal component of the total pressure and E_c , E_{ti} , and E_{te} are the corresponding components of the total specific internal energy. The above mentioned equations do not consider electron-phonon interaction since its contribution is negligible. Brief descriptions of each component are given below.

1.1.1.1 Elastic component

The cold components, P_c and E_c , depend only on specific volume or density and represent the total pressure or total specific internal energy of a substance at absolute zero temperature. Hence they are known as cold pressure and cold specific internal energy. These components arise due to interactions between atoms, i.e. different kinds of bondings [23–25]. Therefore the state of mechanical equilibrium of a solid at zero temperature, corresponds to a minimum in potential energy curve at specific volume V_{c0} , as shown in Fig. 1.1, is characterized by the mutual compensation of the inter-atomic forces of attraction and repulsion. The potential energy curve shows that if the specific volume V is greater than V_{c0} , which is the volume at equilibrium, then attractive forces predominate over repulsive part. At a large volume ($V \gg V_{c0}$) the potential energy becomes the binding (cohesive) energy. Similarly, the repulsive forces increase with decrease of inter atomic separation and it becomes ∞ when $V \rightarrow 0$. It is obvious from first law of thermodynamics that the cold energy and pressure are related as

$$P_c(V) = -\frac{dE_c(V)}{dV} \quad (1.3)$$

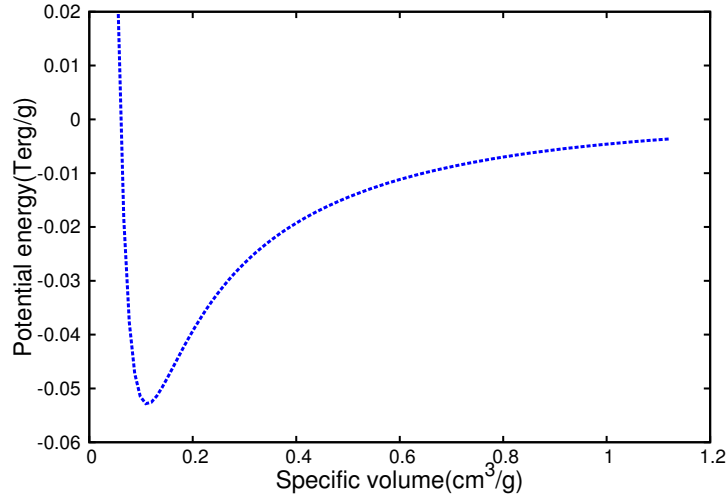


Figure 1.1: Potential energy vs. specific volume curve

Although there are various approaches to predict cold energy (or cold pressure) of a material, the most accurate one is the first principle calculation based on density functional theory (DFT) [26–32]. Since the calculations are computationally intensive, many semi-empirical or semi-analytical models have been proposed by several authors to describe the elastic component [8, 33–45]. The models developed by Birch, Rose, Vinet and Li have been used by many researchers in high energy density (HED) community [8, 33, 35–37]. The mentioned models are described in the subsequent chapters.

1.1.1.2 Ionic thermal component

At finite temperature ($T \neq 0$), the atoms of a material are set into motion due to heating. When temperature is not very high atoms vibrate about their equilibrium positions. The vibrations remain harmonic as long as vibrational energy ($\sim k_B T$ per atom, where k_B is the Boltzmann constant) is significantly less than the height of potential barrier, represents the repulsive forces between the neighbouring atoms, which is order of one or several electron volts for a solid at normal density. The vibrational energy can be comparable with height of the potential barrier at temperatures of the order of ten or several tens of thousands of degrees. At higher temperature the atoms are almost free from their lattice sites and move randomly within the substance. Furthermore, when heating is accompanied with compression the height of the barrier increases sharply thereby treating the thermal motion of the atoms in a compressed ma-

terial as harmonic even up to 20,000-30,000°K as evident from experiments. Although various models have been proposed for ionic thermal part the most widely used ones are Cowan and Johnson model [46, 47] for the compressed solid (i.e. $V < V_0$). Soft sphere model [48, 49] is most commonly employed for expanded states (i.e. $V > V_0$). These models are described in the next chapters.

1.1.1.3 Electronic thermal component

When $T \geq 1$ eV the contribution of thermal excitation of electrons to pressure and specific internal energy becomes important. Thomas and Fermi had introduced first the statistical model for atomic electrons in determining the contribution from electrons to EOS of matter [50–52]. The model is often used in hydrodynamic codes to simulate HED systems due to its simplicity, clarity and validity over a wide range of densities and temperatures.

However, evaluating electronic pressure and energy from in-line solution of Thomas-Fermi equations is computationally expensive. So, McCloskey proposed fitting formulas for P_{te} and E_{te} using solution of Thomas and Fermi, obtained by Gilvarry and Latter [53–55]. The formula obtained by Gilvarry is valid in low temperature limit (i.e. $T \ll T_f$ where T_f is the Fermi degeneracy temperature) whereas Latter's fit describes the electronic thermal properties in high temperature limit i.e. $T \gg T_f$. The McCloskey fits, which provide a continuous transition from low temperature to high temperature limit, are given in chapter 2.

1.2 Background

1.2.1 Dynamic compaction of porous materials

Shock compression of porous materials involves three phases, elastic compression phase, plastic or pore collapse phase and compression phase as shown in Fig. 1.2 [1].

- (a) *Elastic compression phase*: Under low pressure (or stress), elastic deformation of matrix material occurs. This type of deformation involves only

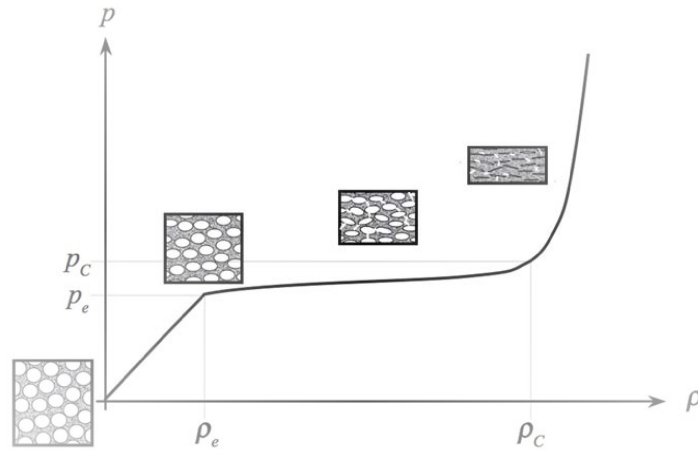


Figure 1.2: Various phases occurring in compression curve for a porous material, taken from [1]. ρ_e is the final density achieved after applying the pressure p_e in the elastic compression phase and ρ_c is the final density achieved due to pressure p_c in the pore collapse phase.

stretching or compression of the atom-atom bonds and hence material returns to its original shape after removing the load.

- (b) *Plastic or pore collapse phase:* When applied pressure is little more the material is permanently deformed due to plastic deformation. In this phase the volume change is more due to collapse of pores which increases the internal energy to a large extent. As a consequence temperature of the substance increases appreciably.
- (c) *Compression phase:* When applied pressure is high enough the volume of the matrix material reduces with compression.

1.2.2 Earlier models for porous substances

Shock compression of porous materials generates a large amount of heat because of collapsing of the pores. As a result, e.g. copper, when $\alpha_0 \geq 2$, the compression curve shows anomalous behavior, where volume increases with increase in pressure rather than decreasing. So, multivaluedness in pressure, i.e. multiple pressure values corresponding to a single volume, occurs in Hugoniot curve as indicated in Fig. 1.3. The anomalous compressibility was first observed experimentally and reported in the literature by Krupnikov and Kormer [56, 57]. Although many constitutive models have been developed to

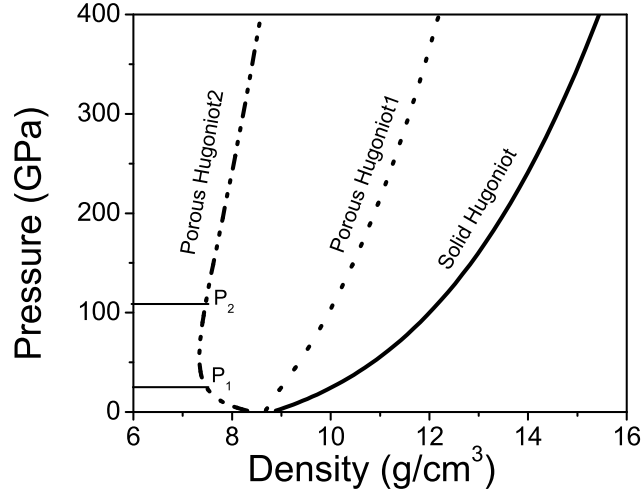


Figure 1.3: Multivaluedness in pressure (P_1 and P_2) occurs in Hugoniot for Cu when $\alpha_0 \geq 2$

predict the behavior of shock compressed porous materials, most of them fail in describing the anomalous behavior. Some of them are mentioned below.

1.2.2.1 Zeldovich and Raizer approach

In order to describe the anomalous behavior, Zeldovich and Raizer used the Hugoniot equation in which pressure and internal energy due to electrons, and initial energy of the medium are neglected. The equation is in the following form

$$P_H(V, V_{00}) = \frac{P_c(V) - (\Gamma_0/V)E_c(V)}{1 + 0.5 \Gamma_0(1 - \alpha_0 V_0/V)} \quad (1.4)$$

where P_c and E_c are the elastic components of the matrix material and Grüneisen coefficient Γ_0 is a constant. Actually the above equation does not reproduce anomalous compressibility.

P_c and E_c are zero at V_0 , and so the numerator in Eq. (1.4) vanishes at V_0 . It is positive for $V < V_0$ because it has a negative slope $-B_0/V_0$ (B_0 is bulk modulus) at V_0 . Now, the denominator of Eq. (1.4) mainly contains the factor $V/V_0 - \alpha_0/(1+2/\Gamma_0)$. For compressive states, ($V/V_0 < 1$) V/V_0 has the minimum value $\alpha_0/(1+2/\Gamma_0)$ where P_H becomes infinity. Thus, maximum density increase, within Zeldovich model, is $1+2/\Gamma_0$ for normal solids ($\alpha_0 = 1$). For porous materials with $\alpha_0 < (1+2/\Gamma_0)$, the Hugoniot is similar to that of nor-

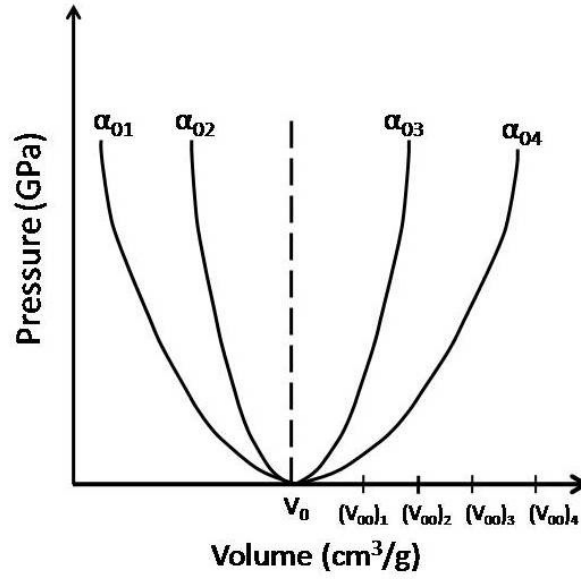


Figure 1.4: Hugoniot curves for different initial porosities. (a) Vertical dashed line represents limiting case i.e. $\alpha_\infty = 1 + 2/\Gamma_0$, (b) α_{01}, α_{02} refer to low porous solid, (c) α_{03}, α_{04} are high porosity cases.

mal solids. It reduces to a vertical line at V_0 when $\alpha_0 = (1+2/\Gamma_0)$. For higher porosities when $\alpha_0 > (1+2/\Gamma_0)$, porous Hugoniot lies in the expanded states with $V/V_0 > 1$, as shown schematically in Fig. 1.4 (cases of α_{03} and α_{04}). Note that the numerator of Eq. (1.4) is negative for $V > V_0$. These cases correspond to anomalous Hugoniot mentioned earlier. A similar approach has been proposed by Lee to compute Hugoniot data for porous systems where reference state is the Hugoniot of the normal solid (not cold component) [58]. The model gives accurate result up to α_∞ (i.e. $1 + 2/\Gamma_0$), which is its limitation. These approximate models give only qualitative results, although they indicate the possibility of anomalous expansion.

1.2.2.2 Model of Kormer *et al*

When porous substances are compressed, the compressed materials may finally be in liquid or dense gaseous phase due to large heating. Therefore Kormer *et al* proposed a three term EOS consisting of contributions from zero temperature isotherm, ion thermal motion and electron thermal excitation such that the different phases are accounted approximately [57]. Their model accommodated the temperature and density dependence of ionic heat capacity and Grüneisen parameter. Specifically, the ion heat capacity within the

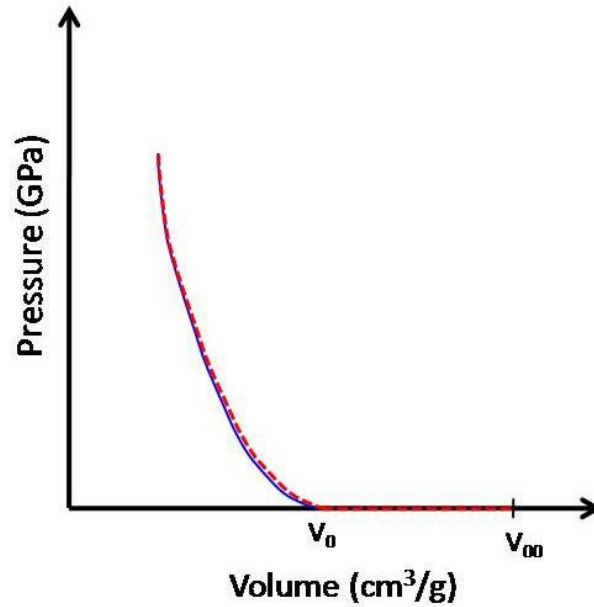


Figure 1.5: Hugoniot curves for a very low porous material (red line), obtained from snow plow model, and for a normal solid (blue line).

model shows variation from $3R$ in solid phase, where R is the gas constant, to $3R/2$ in the gaseous phase. The electron EOS was obtained from numerical fits to Thomas-Fermi model calculations by Latter [55]. This approach indeed showed the anomalous behavior, however, many parameters need to be tuned to match experimental Hugoniot data.

1.2.2.3 Snow plow model

The model describes the dynamic behavior of a porous solid by relating the mechanical process occurs through momentum transfer from an applied pressure impulse to a snow [59]. The model assumes no resistance to compaction i.e. the porous material compacts to its solid density at negligible stress. After compaction, the solid is assumed to be incompressible (an ideal single-stage locking material) until a new density state is obtained due to much greater stress and the resultant Hugoniot is essentially same with a non porous sample, as illustrated in Fig. 1.5. Therefore the model is appropriate for very low porous substances where pores are completely collapsed under shock loading.

1.2.2.4 P- α model

In reality, most of the distended solids show resistance to compaction thereby achieving only partial compaction. The partially compacted states are described by P- α model, developed by W. Hermann in 1969, where α is the instantaneous porosity defined as the ratio of specific volume of porous material (V_p) to specific volume of the corresponding solid material (V_s) at same pressure and temperature [11]. The model assumes that the EOS, neglecting shear strength, relating pressure, specific volume and specific internal energy (E) is same for a material in its porous and non-porous state, and the form is given by

$$P = g(V_s, E) = g(V_p/\alpha, E) \quad (1.5)$$

In order to describe the dynamic behavior of a porous solid completely, Eq. (1.5) should be supplemented with a relation for α . The factor α can be specified as a function of P and E i.e. $\alpha = f(P, E)$, but along a normal Hugoniot, where variation of E is implicit, it can be expressed as $\alpha = f(P)$. The value of α lies between α_0 and 1. In elastic range, $\alpha(P)$ can be determined by solving the following differential equation numerically,

$$\alpha' = \frac{\alpha}{B_0} \left(1 - \frac{\alpha}{h^2}\right), \quad h = \frac{C_e - C_0}{C_0(\alpha_0 - 1)} + 1 - \alpha \quad (1.6)$$

where B_0 , C_0 are bulk modulus and bulk sound speed in solid at $P=0$, $V=V_{s0}$, and C_e is the elastic wave velocity at $P=0$, $\alpha=\alpha_0$, $V=V_{s0}$. In plastic range, $\alpha(P)$ is, described by a quadratic fit, given by

$$\alpha = 1 + (\alpha_p - 1) \left[\frac{P_s - P}{P_s - P_e} \right]^2 \quad (1.7)$$

where P_e , P_s refer to pressure values at elastic and plastic limit, and $\alpha=\alpha_p$ at $P=P_e$ as illustrated in Fig. 1.6. The material constants for iron, at porosity 1.63, are $V_{s0}=0.128 \text{ cm}^3/\text{g}$, $C_0=4.63 \text{ mm}/\mu\text{sec}$, $C_e=3.0 \text{ mm}/\mu\text{sec}$, $P_e=1.55 \text{ kbar}$ and $P_s=12 \text{ kbar}$.

Fig. 1.6 depicts dynamic compaction of a porous solid using P- α model. Several stages involved in this model are:

- (i) For highly porous materials, most elastic compression occurs due to elas-

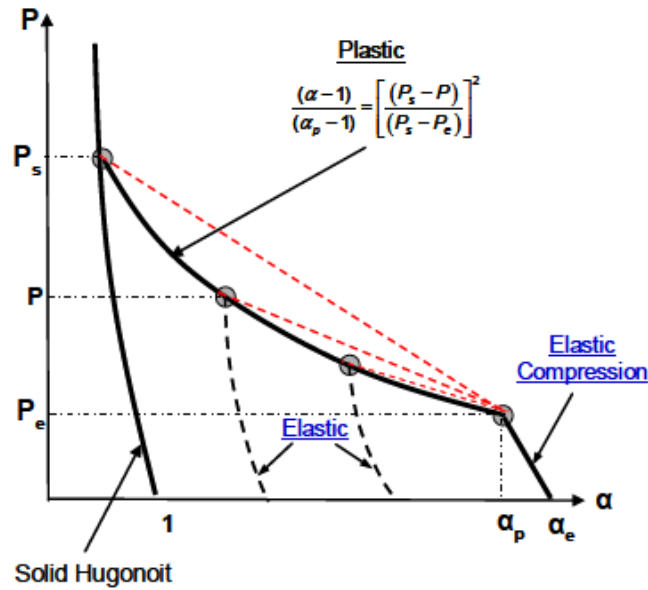


Figure 1.6: Dynamic compression of porous solid using P - α compaction model, taken from [2]

tic buckling of the cell walls.

- (ii) The onset of permanent volume change coincides with the onset of plastic deformation of the cell walls at pressure P_e , which is the yield strength of the porous material.
- (iii) Dynamic compaction then moves along Rayleigh lines to end states on the plastic curve until the pressure reaches the fully compacted state at the solid compaction pressure P_s or is released to a partially compacted state.
- (iv) Also unloading from partially compacted state is elastic where end state is at a relatively smaller specific volume than the starting volume.

Although this model accounts for the presence of pores, by expressing specific volume of porous substance as sum of specific volume of parent matter and volume of the voids, but mesoscale features such as size or shape of individual voids, distribution of voids etc are not taken into account. The drawback of the model is the assumption that same EOS relation holds for both solid and porous materials.

1.2.2.5 Model of Carroll and Holt

Carroll and Holt [12] modified the constitutive equation, proposed by Hermann, by a factor $1/\alpha(P)$ where $\alpha(P)$ represents pore collapse relation. The modified form is given by

$$P = \frac{1}{\alpha} g(V/\alpha, E) \quad (1.8)$$

They proposed an empirical fit for $\alpha(P)$ which includes initial elastic (reversible) behavior, subsequent plastic (irreversible) behavior, and asymptotically tends to one at high pressure to describe compaction of porous substances. The pore collapse relation is given as

$$\alpha(P) = \begin{cases} \alpha_0, & 0 < P < P_{cri} \\ \frac{1}{1 - \exp(-3P/2Y_s)}, & P_{cri} < P < \infty \end{cases} \quad (1.9)$$

where Y_s is the yield strength of the matrix material and P_{cri} is the elastic critical pressure of the porous material beyond which compaction initiates. The expression of P_{cri} is as follows.

$$P_{cri} = \frac{2}{3} Y_s \ln \left(\frac{\alpha_0}{\alpha_0 - 1} \right) \quad (1.10)$$

The calculation of $\alpha(P)$ depends on material constant Y_s and pore geometry through initial porosity α_0 rather than many material constants as mentioned in Eq. (1.6) and (1.7). Hence this empirical fit is a preferable one to describe pore collapse.

1.2.2.6 Mie-Grüneisen EOS

Mie-Grüneisen EOS relates pressure and specific internal energy of a state at a given specific volume by Grüneisen parameter $\Gamma(V)$. The formula is given by

$$P - P_r = \frac{\Gamma(V)}{V} (E - E_r), \quad \Gamma(V) = V \left(\frac{\partial P}{\partial E} \right)_V \quad (1.11)$$

where P_r and E_r are pressure and energy of a reference state, either a zero temperature isotherm or a Hugoniot or an isentrope.

$\Gamma(V)$ measures the change in pressure of a system produced by a change in spe-

cific internal energy at constant volume. The temperature dependence of this parameter, through E and P , is negligible. Although several fitting formulas for Γ have been proposed in literature the most commonly used fits are suggested by Slater, Dugdale-McDonald and Vashchenko-Zubarev [60–62]. The SDMVZ formula is given by

$$\Gamma(V) = \frac{q-2}{3} - \frac{V}{2} \frac{d^2(P_c V^{2q/3})/dV^2}{d(P_c V^{2q/3})/dV} \quad (1.12)$$

where $q=0, 1, 2$ stands for Slater, Dugdale-McDonald and Vashchenko-Zubarev formulas respectively. It is obvious from Eq. (1.11) that multiple values of pressure can't be reproduced for a single volume.

The above mentioned models could not explain anomalous compressibility observed in Hugoniot. Hence thermodynamic modeling with volume and temperature as independent parameters fails in describing anomalous behavior.

1.2.2.7 Model of Zubarev *et al*

To predict the Hugoniot for distended materials Zubarev *et al* [63] proposed a model along an isobaric path. In this approach, the specific internal energy is related to specific volume through a parameter $\eta(P)$, similar to the Grüneisen parameter [64, 65], for a given pressure. The expression is as follows.

$$V - V_r(P) = \frac{\eta(P)}{P} [E(P, V) - E_r(P)], \quad \eta(P) = P \left(\frac{\partial V}{\partial E} \right)_P \quad (1.13)$$

Here $E_r(P)$ and $V_r(P)$ refers to specific internal energy and volume on a reference curve. Although they realized the need to treat pressure as independent variable but the significance and variation of $\eta(P)$ with P are not mentioned by these authors.

1.2.2.8 Model of Wu and Jing

A similar approach is developed by Wu and Jing [66] from thermodynamic consideration for extrapolating solid Hugoniot to porous states. The model relates specific enthalpy and specific volume through a material parameter χ , known as enthalpy parameter, as a function of pressure. The form of the EOS

is given by

$$V - V_c(P) = \frac{\chi(P)}{P} [H(P, T) - H_c(P)] \quad (1.14)$$

where $V_c(P)$ and $H_c(P)$ are, respectively, specific volume and specific enthalpy on zero kelvin isotherm. The EOS, named as enthalpy-based EOS, was originally proposed by Rice and Walsh to calculate the Hugoniot of water up to the pressure 250 kbar [67]. Using the Carroll and Holt model prescriptions, and the Hugoniot elastic limit, they extended the zero temperature isotherm of the solid to the porous regime, thereby making their approach suitable for compaction as well as compression parts in shock loading.

The χ parameter remains same for porous and non porous solids since it depends on pressure. They computed the parameter using Grüneisen parameter and isentropic bulk modulus along solid Hugoniot to obtain Hugoniot data of several metals. The details calculation of χ parameter are given in chapter 2.

1.2.2.9 Model of Viljoen *et al*

Viljoen *et al* simplified the Wu and Jing method of calculation of χ parameter without accounting the Hugoniot elastic limit (HEL) as well as compaction regime. The parameter is computed using zero kelvin isotherm and solid Hugoniot, which employs Mie-Grüneisen EOS. Then the same χ is used in Eq. (1.14) to determine Hugoniot data for porous systems at different initial porosities [68]. The method gives reasonable results up to porosity 4 for Cu.

1.2.2.10 Model of Huayun *et al*

Huayun *et al* extended the Wu and Jing method by splitting the enthalpy parameter χ into ionic and electronic components to obtain the electronic contribution explicitly [69, 70]. However, the expression of enthalpy-based EOS proposed by them contains several errors.

In chapter 2, a correct set of equations, including effect of electrons explicitly, are derived. Also, we have pointed out the errors made by Huayun *et al* in deriving enthalpy-based EOS with electronic contribution and the expression for volume on Hugoniot, and brought out the correct contribution of thermal

electrons due to excitations. Thus explicit treatment of electrons is correctly done for the *first time* as explained in chapter 2.

1.3 Research objective

Propagation of shock in distended solids produces a large amount of heat. Thus temperature of the shocked state increases appreciably which enhances thermal ionization of electrons. Then electron contribution becomes significant in calculating thermodynamic properties of the shock loaded material. The earlier models have not considered effect of electrons in thermodynamic modeling of porous systems. We have developed a generalized enthalpy-based EOS model, including electronic effect explicitly, from thermodynamic definitions to predict Hugoniot data for highly porous substances. Our model shows significant difference in Hugoniot data with and without electronic contribution for Cu when $\alpha_0 \geq 2$.

Understanding the propagation of shock waves in heterogeneous materials (mixtures) is of considerable interest in many applications such as impact, blast and material synthesis etc. To describe these phenomena, EOS of mixture is essential. We have developed an EOS model for binary mixtures employing generalized enthalpy-based EOS model for individual components. The model is applied to various binary mixtures including tantalum carbide-carbon (TaC-C) porous mixture to determine Hugoniot parameters (i.e. Hugoniot curves, T vs. P , shock (U_s) and particle velocity (U_p) curves etc). Our model predicts correct equilibrium temperature on mixture Hugoniot, e.g. temperature of TaC-C porous mixture is much higher than the temperatures of other mixtures due to effect of porosity.

An EOS model for multi-component mixtures, employing enthalpy-based approach, is proposed to study shock wave propagation in composite materials. The model is applied to epoxy based composites, which are slightly porous in nature, to calculate Hugoniot data. The P vs. U_p and U_s vs. U_p data obtained from our model match well with existing experimental data.

For higher porosities, e.g. $\alpha_0 \geq 3$ for Cu, the shock states lie in the fluid phase where compressed volume is higher than initial volume V_0 . To describe this feature an appropriate fluid model is needed. Therefore we have developed a modified soft sphere model for enthalpy-based approach [48, 49], incorporating the effect of energy loss from the shock due to expansion of the shocked material as observed experimentally for polystyrene [71]. The new model is applied to Cu as prototype to predict Hugoniot parameters and it gives accurate result in a wide range of porosity i.e. from initial porosity 1 to 10.03.

Propagation of shock waves in condensed matter is a topic of great importance in high energy density systems, like stellar structures, inertial confinement fusion, nuclear weapons, etc. The propagation of shock generates hydrodynamic motions in the materials. As a consequence, the state variables such as density, pressure, internal energy, particle velocity etc., of the material change in space and time. The profiles of the state variables are important in analyzing dynamic behavior of material under shock loading. We have studied the shock wave propagation in normal and porous Cu via numerical simulations of the Euler equations describing conservation laws of mass, momentum and energy.

1.4 Outline of thesis

The thesis is organized as follows. In chapter 2, we have derived the generalized enthalpy-based EOS, including electronic effects, from thermodynamic definitions, i.e. $(\partial V/\partial T)_P = (\chi/P)C_P$ and $(\partial H/\partial T)_P = C_P$, where C_P is constant pressure specific heat. Here the Hugoniot relation across shock front and equation for temperature along Hugoniot are solved simultaneously to calculate P-V curve and its corresponding temperature for porous copper at different initial densities. We have compared P-V Hugoniot with and without thermal electrons for Cu with $\alpha_0=2$ to depict its significant contribution due to porosity. A three component EOS is used to calculate ionic enthalpy parameter, electronic specific enthalpy, specific heat at constant pressure due to ions and electrons. For cold component, we have considered Li 4-parameter EOS which is valid in compression as well as expansion regime. We have used Cowan's model and McCloskey fitting for ionic and electronic contribution, which are

accurate in a wide range of density and temperature. All these models are discussed in detail in this chapter. The results obtained from our model agree well with experimental data. Also, the errors involved in earlier attempts, by Huayun *et al*, in deriving enthalpy-based EOS with electronic contribution and the inconsistency in the expression for volume on Hugoniot using conservation laws across shock front are brought out.

In chapter 3, we have developed a method to calculate Hugoniot for binary mixtures using generalized enthalpy-based EOS formulations, derived for binary mixtures by introducing proper averaging of zero temperature isotherm and enthalpy parameters. The EOS model accounts for non-equilibrium thermal effects with the assumption that both pressure and material velocity are in equilibrium. It contains an extra term arises because of difference in ionic specific enthalpies of individual components of the mixture. Moreover, the contribution of the difference term is very small in Hugoniot but temperatures occurring in that term are important in other applications such as shock induced chemical reactions, structural phase transitions, dissociations etc. This enthalpy-based EOS is well suited for mixtures because pressure equilibrium is fast. The binary mixture EOS is applied to various mixtures, metallic, mixtures of compounds, mixtures of dissimilar solids, porous mixtures, and the results agree well with experimental data. The treatment of porous binary mixtures within the enthalpy-based EOS is done for the *first time*. Also, for the *first time*, single component criteria for each component is used to obtain non-equilibrium temperature in binary mixtures.

Chapter 4 describes a method to compute Hugoniot of multi-component mixtures using enthalpy-based EOS, derived for multi-component mixtures. In the present method, the non-equilibrium temperature and thermal electronic effects are accounted explicitly. Here, single component criteria is proposed to compute non-equilibrium temperatures of individuals components. The EOS model is applied to epoxy based composite materials to calculate Hugoniot data. The method calculates the mixture Hugoniot accurately, when correct set of EOS parameters, i.e. initial density, bulk modulus, pressure derivative of bulk modulus, Grüneisen parameter, constant volume specific heat, at ambient condition are supplied. Also the term, which arises due to ionic specific

enthalpy difference becomes more important in multi-component mixtures, which gives 2-3 % difference in P-V curve as shown for epoxy based two and three component mixtures.

In chapter 5, we have developed a modified soft sphere model for fluid phase to apply generalized enthalpy-based EOS to higher porosities ($\alpha_0 \geq 3$). The modification is mainly the determination of all the parameters of the soft sphere model in terms of three experimental data, viz., density, cohesive energy and bulk modulus of the solid at normal conditions. Our generalized soft sphere model contain all the three components, i.e. cold, ionic and electronic, in EOS. The liquid-vapor co-existence curve of copper obtained from the model shows good agreement with those from detailed molecular dynamics simulations. Also, we have modeled the effect of energy loss from shock, which occurs due to expansion of the shocked vapor to the final volume, for high porosity cases, as a PdV term. Pressure-volume curves and shock speeds vs. particle speeds results obtained from the model, with these modifications, compare well with experimental data. Our approach uses accurate models corresponding to fluid phase, and incorporates energy loss due to vapor expansion in a general way (PdV work) for the *first time*.

In chapter 6 we study shock wave propagation in condensed matter, via numerical simulations of the Euler equations describing conservation laws of mass, momentum and energy. The propagation of shock generates hydrodynamic motions in the materials. Here we use Lagrangian approach to study material motion. The approach uses Flux-Corrected Transport (FCT) algorithm to solve system of coupled non-linear conservation equations rather than the conventional finite difference approximation. The FCT algorithm is a monotone, conservative, positivity preserving algorithm and is also accurate up to 2nd order with respect to time step. The algorithm does the simulation in two stages: a convective stage followed by an anti-diffusive stage. The details of mesh generation, discretization of continuity equation, boundary conditions are mentioned in this chapter. We have simulated impact experiments (Cu-impactor+Cu-target) employing Mie-Gruneisen EOS for normal solid and enthalpy-based EOS for porous substances. Initial pressure rise, peak pressure and shock duration are accurately modeled in the simulation. The simulation

results (i.e. peak pressure, shock and particle velocity etc) for solid as well as low porous Cu match well with analytical ones, obtained from *impedance matching techniques*. The peak pressure and shock velocity attenuate fast for porous Cu even with low porosity i.e. 1.1 and 1.3, which is consistent with theory. Our approach can predict shock wave properties of porous materials as the EOS is based only on a few experimental data of the solid at normal conditions. To illustrate this aspect, we have determined pressure vs. particle speed curves for two porosities from simulations and compared them with experimental data.

Existing issues and future research scope are listed in chapter 7.

Explicit accounting of electronic effects on the Hugoniot of porous materials

2.1 Introduction

Shock compression of porous materials involves initial compaction, which closes the pores, followed by compression of the matrix material [58]. Recent molecular dynamics simulations of model porous systems show the microscopic mechanisms involved during the process of void collapse [72, 73]. Initial shocking of solid matrix, shock break out at the void interfaces, and subsequent collisional energy dissipation of the ejecta pave way for initiation of hot spots and local heating [74]. Thus very high temperatures are indeed produced on shock loading of porous materials. Because of high temperature rise, porous solids show anomalous behavior, i.e. volume increases with applied pressure rather than decreasing, under shock loading for higher initial porosity [23]. The anomalous behavior leads to multiple values of pressure in Hugoniot as illustrated in the previous chapter. Hence thermodynamic modeling, employs specific volume (V) and temperature (T) as independent parameters, can't explain this special feature.

The need to use pressure as the independent variable for obtaining the Hugoniot of porous materials from their corresponding solid counterparts was shown by Oh and Persson [64]. However, this was already realized in the 1970's by Zubarev *et al* [63]. In this approach, the specific internal energy is related to specific volume through a parameter η , as a function of pressure, which is similar to the Gruneisen parameter [64, 65]. The use of isobaric path to extrapolate the Hugoniot of normal solids to that including porosity effects was developed in detail by Wu and Jing, from thermodynamic consideration [66]. Their equation of state (EOS), known as enthalpy-based EOS, relates specific

enthalpy H and specific volume through enthalpy parameter χ which depends only on pressure. Thermodynamic consistency requirements show that if χ depends only on pressure, the constant pressure specific heat C_P can be either a constant or a function of entropy $S(P, T)$ [75]. This scheme has also been applied to treat mixtures using an average zero temperature isotherm [76]. It is also found to be useful to describe the Hugoniot of preheated solids [77]. Further applications have been to describe Hugoniot of porous compounds such as SiO_2 , UO_2 , B_4C and Ta_2O_5 [78, 79]. The Wu-Jing approach was simplified by Viljoen *et al* without accounting Hugoniot elastic limit and isentropic bulk modulus to predict Hugoniot data for porous systems [68].

The developments briefly described above do not consider thermal electron excitation explicitly [80]. Though this effect is implicitly present in the Hugoniot of the solid, electronic contribution is negligible in the P-V curve up to few hundred GPa pressures. Huayun *et al* extended Wu-Jing method by introducing separately enthalpy parameters χ_i and χ_e for the ionic and electronic components, however, their proposed EOS contain several errors [69, 70]. Developing the correct set of equations within the generalized enthalpy-based EOS is one of the aims of the present chapter. This approach needs simultaneous evaluation of P-V curve and temperature. We present a numerical method for practical implementation of the scheme, which needs enthalpy parameters χ_i and χ_e and constant pressure specific heats C_{P_i} and C_{P_e} of ions and electrons. A three component EOS is used for determining these parameters.

The chapter is organized as follows. In section 2.2 we derive the generalized enthalpy-based EOS. It is then applied to obtain Hugoniot of porous materials in section 2.3. A simple numerical method for simultaneous solution of temperature and P-V curve is presented here. Errors in the approach of Huayun *etal* are discussed. The three component EOS, method of calculation of constant pressure specific heats and enthalpy parameters are also outlined in this section. Results on porous copper are given in section 2.4. Finally, section 2.5 summaries the work.

2.2 Generalized enthalpy-based EOS

A brief account of the enthalpy-based EOS, wherein P and T are independent variables, is presented here. The parameter χ and constant pressure specific heat C_P are defined as $(\partial V/\partial T)_P = (\chi/P)C_P$ and $(\partial H/\partial T)_P = C_P$, respectively. The product χC_P as well as C_P contain thermal ionic and electronic effects as it is based on total specific volume and enthalpy. However, it is possible to split these into separate ionic and electronic components as $\chi C_P = \chi_i C_{P_i} + \chi_e C_{P_e}$. Here C_{P_i} and C_{P_e} are, respectively, the constant pressure ionic and electronic specific heats, and $C_P = C_{P_i} + C_{P_e}$. This decomposition also shows that the effective χ , which includes ionic and electronic effects, is to be obtained by weighting the separate components with constant pressure specific heats. Now, integrating from zero temperature, specific volume V and specific enthalpy H can be expressed as

$$V(P, T) = V_{cs}(P) + \int_0^T \frac{1}{P} \chi_i(P, \tau) C_{P_i}(P, \tau) d\tau + \int_0^T \frac{1}{P} \chi_e(P, \tau) C_{P_e}(P, \tau) d\tau \quad (2.1)$$

$$H(P, T) = H_{cs}(V) + \int_0^T C_{P_i}(P, \tau) d\tau + \int_0^T C_{P_e}(P, \tau) d\tau. \quad (2.2)$$

Here the reference state parameters V_{cs} and $H_{cs} = E_{cs}(V_{cs}) + PV_{cs}$ denote, respectively, the zero temperature specific volume and specific enthalpy of the solid at pressure P . Volume V_{cs} is to be obtained by inverting the zero temperature isotherm of the solid, and is defined by: $P_{cs}(V_{cs}) = P$.

The Gruneisen parameter for thermal electrons Γ_e is adequately represented by a constant which assumes values in the range 0.6-0.8 [57]. Therefore, $\chi_e = \Gamma_e / (\Gamma_e + 1)$ is independent of temperature. Though this property is not true for ionic part, the dependence of χ_i on temperature is rather weak. This has been demonstrated by comparing its variation with pressure on the Hugoniot and zero temperature isotherm for Al [75]. We have done a similar comparison for Cu in Fig. 2.1 (also see discussion in section 2.4). So we approximate $\chi_i(P, \tau)$ in the first integral of Eq. (2.1) by its value $\chi_i(P, T)$ at the upper limit of the integral. The leading error involved in this approximation is $\sim \chi'_i(T) C_{P_i}(T) T^2$, where $\chi'_i(T)$ is the temperature derivative. After invoking this approxima-

tion, Eqs. (2.1) and (2.2) can be combined together to obtain the generalized enthalpy-based EOS:

$$V = V_{cs} + \frac{1}{P}\chi_i(P, T)H_{ti}(P, T) + \frac{\chi_e}{P}H_{te}(P, T) \quad (2.3)$$

$$= V_{cs} + \frac{1}{P}\chi_i(P, T)(H - H_{cs} - H_{te}) + \frac{\chi_e}{P}H_{te}(P, T) \quad (2.4)$$

where H_{ti} and H_{te} are, respectively, thermal ionic and electronic specific enthalpy. Using the general defining equation $\chi = P(\partial V / \partial H)_P$, the ionic parameter χ_i can also be expressed as $\chi_i = P\Gamma_i / K_{Si}$, where K_{Si} and Γ_i are, respectively, the iso-entropic bulk modulus and Gruneisen parameter of ions. Γ_i , which is generally taken as a function of volume V , is to be expressed in terms of P using the EOS of the material. This transformation makes χ_i a function of temperature as well. However, this dependence could be made implicit if it needs to be computed only along some specific P-V curve such as an isentrope, where temperature variation is implicit [75]. Wu and Jing computed χ_i along the solid Hugoniot to calculate Hugoniot data of porous substances.

2.3 Porous Hugoniot

Initial porosity characterizing the material is defined as $\alpha_0 = V_{00} / V_0$, where V_0 is the initial volume of the solid while V_{00} is the extended volume including that of the pores. Before applying Eq. (2.4) to porous materials, it is necessary to extend it to the region $V_0 \leq V \leq V_{00}$. This is obtained using instantaneous porosity $\alpha(P)$, given by Carroll and Holt [12]:

$$\alpha(P) = \begin{cases} \alpha_0, & 0 < P < P_{cri} \\ \frac{1}{1 - \exp(-3P/2Y)}, & P_{cri} < P < \infty \end{cases} \quad (2.5)$$

where Y denotes the strength of the matrix material, which for Cu is ~ 0.4 GPa and P_{cri} is the elastic critical pressure of the porous material beyond which compaction initiates. The expression of P_{cri} is as follows.

$$P_{cri} = \frac{2}{3}Y \ln \left(\frac{\alpha_0}{\alpha_0 - 1} \right)$$

Starting with a specified pressure P , first $\alpha(P)$ and volume of solid $V_{cs} \leq V_0$ are determined, which then provides the porous volume $V_c = \alpha(P)V_{cs}$. The modified P - α model is then used to get the extended zero temperature isotherm $P_c(V) = P_{cs}(V)/\alpha(P)$. This approximation assumes that $E_c(V)$ is the same as that of the solid matrix in the range $V_0 \leq V \leq V_{00}$ [58]. For pressures above ~ 1 GPa, it is unnecessary to use extended V_c and $P_c(V)$ because $\alpha(P)$ would be very close to unity.

The porous Hugoniot is readily obtained by combining Eq. (2.4) with the expression for enthalpy along the Hugoniot:

$$H = E_{00} + \frac{1}{2}P_{00}(V_{00} - V) + \frac{1}{2}P(V_{00} + V) \quad (2.6)$$

where E_{00} and P_{00} are, respectively, the energy and pressure at initial volume V_{00} . The parameters corresponding to Hugoniot elastic limit can be incorporated in it by taking $P_{00} = P_{hel}$ and $E_{00} = P_{hel}(V_{00} - V_{hel})/2$. The resulting V-P curve is given by

$$V = 2V_c \frac{1 - \chi_i}{2 - \chi_i^*} + \frac{\chi_i}{2 - \chi_i^*} \left(V_{00}(1 + P_{00}/P) + \frac{2}{P}(E_{00} - E_c(V_c)) \right) + \frac{2}{P} \frac{\chi_e - \chi_i}{2 - \chi_i^*} H_{te}(P, T) \quad (2.7)$$

where pressure and temperature dependence of H_{te} is shown explicitly, and $\chi_i^* = \chi_i(1 - P_{00}/P)$. This expression reduces to those given by Wu and Jing and Viljoen when either $\chi_e = \chi_i = \chi$ or $H_{te} = 0$ [66, 68]. Eq. (2.7) is to be solved together with the differential equation for Hugoniot temperature along isobaric path, viz.,

$$\frac{dT}{dP} - \frac{\chi}{P}T(P) = \frac{1}{2C_P} \left((V_{00} - V) + (P - P_{00})dV/dP \right) \quad (2.8)$$

Here, $\chi = (\chi_i C_{Pi} + \chi_e C_{Pe})/C_P$ is the effective enthalpy parameter and ions and electrons are assumed to be in thermal equilibrium. This equation is similar to the Walsh-Christian differential equation in which V is the independent variable. The expression for the latter is given by [81]

$$\frac{dT}{dV} - \frac{\Gamma_{ef}}{V}T(V) = \frac{1}{2C_V} \left((P - P_{00}) + (V_{00} - V)dP/dV \right) \quad (2.9)$$

where Γ_{ef} is the effective Gruneisen parameter, defined as $\Gamma_{ef}=(\Gamma_i C_{Vi}+\Gamma_e C_{Ve})/C_V$.

Assuming a linear relation between shock and particle speeds, and Debye-Gruneisen thermal EOS, Nagayama has evolved a method for obtaining Hugoniot temperature [82]. However, we shall not pursue this method here because, for the case of porous materials, (i) significant curvature is found in the variation of shock speed with particle speed, and (ii) melting transition and electronic effects needed to be accounted, modify the equations for thermal energy or enthalpy.

2.3.1 Numerical method

We employ a simple finite difference method to solve the coupled equations. Using forward differencing, Eq. (2.8) can be written in discrete form as:

$$T_n = \frac{T_{n-1} + 0.5 \left((V_{00} - V_n) \Delta P + (P_n - P_{00})(V_n - V_{n-1}) \right) / C_{P,n}}{1 - \Delta P \chi_n / P_n} \quad (2.10)$$

Here the subscript n on different variables denotes their values at $P_n = P_{00} + n \Delta P$ where ΔP is an increment in pressure, and $n = 1, 2, 3$, etc. Numerical values of V_n corresponding to P_n is to be computed from Eqs.(2.7) as

$$V_n = V_n^* + \frac{2}{P_n} \frac{\chi_e - \chi_{i,n}}{2 - \chi_{i,n}^*} H_{te}(P_n, T_n) \quad (2.11)$$

The term V_n^* , which represents the first two terms in Eq. (2.7), is the volume on the Hugoniot excluding electronic effects. Now, if thermal electron energy E_{te} is expressed in terms of P and T , then $H_{te} \equiv (\Gamma_e + 1)E_{te}$. Alternatively, H_{te} may be obtained by integrating $C_{Pe}(P_n, \tau)$ from 0 to T_n , and could be done in a recursive manner. Therefore, Eqs. (2.11) and (2.10) have to be evaluated iteratively at each P_n . Starting with a guess value of T_n , say T_{n-1} , first V_n is computed using Eq. (2.11). Then Eq. (2.10) is used to get an improved value of T_n . These two steps are then repeated until values of T_n between successive steps are within a prescribed error. We find that few iterations are adequate to get converged values of T_n and V_n . The whole process is repeated for all $n = 1, 2, 3$, etc., thereby obtaining volume, pressure and temperature on the Hugoniot in a consistent manner.

2.3.2 Method of Huayun *et al*

In attempting to include electronic effects in enthalpy-based EOS, Huayun *et al* obtained an incorrect expression for V . In comparison to Eq. (2.7), these authors obtain [69, 70]

$$V = V^* + \frac{\chi_e}{P} H_{te} \quad (2.12)$$

where V^* denotes the first two terms in Eq. (2.7). More explicitly, χ_e appears in the last term of Eq. (2.12), while we obtain $2(\chi_e - \chi_i)/(2 - \chi_i)$. This difference has important consequences. Their equation does not yield the expression given by Viljoen when $\chi_i = \chi_e = \chi$. That is an error because, in this limit, the basic Eqs. (2.3) and (2.6) show that there is only a single effective parameter χ and the expression for V must reduce to that given by Viljoen. In the high temperature limit, when ions and electrons obey ideal mono atomic gas laws, $\Gamma_i = \Gamma_e = 2/3$ and so $\chi_i = \chi_e = 2/5$, Eq. (2.7) gives correct results; for example, it yields the limiting volume ratio $(V/V_{00})_{min} = \chi_i/(2 - \chi_i) = 1/4$. This case does not produce high temperature limiting ratio from Eq. (2.12) because $\chi_e = \Gamma_e/(\Gamma_e + 1)$ and $H_{te} = (\Gamma_e + 1) E_{te} = (\Gamma_e + 1) P_{te} V / \Gamma_e$, and so one ends up with $V^* = V(1 - P_{te}/P)$. The root cause of these errors is that Huayun *et al* neither use Eq. (2.4) nor Eq. (2.6) in their approach. Instead they use Eq. (2.12) together with the closing relations for V^* :

$$V^* = V_c + \frac{\chi_i}{P} (H^* - H_c) \quad (2.13)$$

$$H^* = E_{00} + \frac{1}{2} P_{00} (V_{00} - V^*) + \frac{1}{2} P (V_{00} + V^*) \quad (2.14)$$

The first is enthalpy EOS for the ionic part while the second is enthalpy on the Hugoniot computed at V^* . It is obvious that that total enthalpy on the Hugoniot is to be calculated at V , and used with the complete EOS for ions and electrons. These authors also expressed H_{te} in terms of V and T , and not in terms of P and T . Then they evaluate $H_{te}(V, T)$ at V^* , which has no justification. Furthermore, they used an ad-hoc effective parameter $\chi = (\chi_i \times \chi_e) / (\chi_i + \chi_e)$. This expression does not yield χ when $\chi_i = \chi_e = \chi$, and so is wrong. Thus, their approach is basically incorrect, irrespective of the effect of errors on numerical results. Therefore we shall not dwell on it any further.

2.3.3 Three Component EOS

Three component EOS models of varying degrees of sophistication are currently available for describing thermodynamic parameters in hydrodynamic analyses [46, 49, 83]. Pressure and energy, expressed in terms V and T , are split into three components, namely, (i) cold component, (ii) ionic thermal component, and (iii) electronic thermal component:

$$P(V, T) = P_c(V) + P_{ti}(V, T) + P_{te}(V, T) \quad (2.15)$$

$$E(V, T) = E_c(V) + E_{ti}(V, T) + E_{te}(V, T) \quad (2.16)$$

2.3.3.1 Cold component

Li *et al* proposed empirical fits for P_c and E_c by fitting data, obtained from *ab initio* calculations, with four experimental parameters i.e. equilibrium volume V_0 , cohesive energy E_{coh} , bulk modulus B_0 and its pressure derivative B'_0 [8]. The expressions are:

$$P_c(V) = \frac{3B_0(1-x)}{x^2}(1-3\delta a + \delta a^2)e^{-a}, \quad x = \left(\frac{V}{V_0}\right)^{1/3}, \quad a = \eta(x-1) \quad (2.17)$$

$$E_c(V) = -E_{coh}(1+a+\delta a^3)e^{-a}, \quad \eta = \left(\frac{9B_0V_0}{E_{coh}}\right)^{1/2}, \quad \delta = \frac{B'_0-1}{2\eta} - \frac{1}{3} \quad (2.18)$$

This model provides accurate values of the zero temperature energy and pressure over compressed as well as expanded states for a variety of materials [8].

2.3.3.2 Ionic thermal component

Cowan model

The model for ionic thermal energy should describe low temperature properties of solids, fluid phase for temperatures above melting point and ideal gas behavior at still higher temperatures. Thus molar C_{V_i} must vary from Debye's T^3 law to $3R$ and finally to $3R/2$, where R is the gas constant. This feature is essential since shock compression of porous materials produce high temperatures. The mean field model used by Wang does not possess this crucial feature [84]. The parameters in the ionic model used by Korner *et al* has to be adjusted for every material [57]. So we use a modified Cowan's model [46], with alternate specifications of Debye temperature $\theta(V)$ and melting tempera-

ture $T_M(V)$. For $w=T/T_M < 1$ we use the well known expressions:

$$E_{ti}(V, T) = E_D = \frac{k_B T}{AM_p} \left(\frac{9}{8}u + 3D(u) \right) \quad (2.19)$$

$$P_{ti}(V, T) = P_D = \frac{\Gamma_s(V)}{V} E_{ti}(V, T), \quad u = \theta(V)/T \quad (2.20)$$

where k_B is Boltzmann's constant, A atomic number, M_p proton mass, Γ_s Gruneisen parameter in solid phase, $\theta(V)$ Debye temperature and $D(u)$ Debye function. The fluid approximation for $w \geq 1$ is given by

$$E_{ti}(V, T) = \frac{3}{2} \frac{k_B T}{AM_p} (1 + w^{1/3}), \quad P_{ti}(V, T) = \frac{1}{V} \frac{k_B T}{AM_p} (1 + \Gamma_F w^{1/3}) \quad (2.21)$$

where $\Gamma_F = 3\Gamma_s - 1$ is Gruneisen parameter for the fluid phase [46]. In lieu of the empirical formula for $\Gamma_s(V)$ in the original Cowan's model, we use a three parameter fit by Preston *etal* [7]:

$$\Gamma_s(V) = \frac{1}{2} + c_1 V^{1/3} + c_2 V^q \quad (2.22)$$

The parameters c_1 , c_2 , and q are determined using experimental data on Γ_s at $T=300$ K, at zero pressure melting point T_M and asymptotic ($V \rightarrow 0$) approximation for free electron states. Expressions for $\theta(V)$ and $T_M(V)$ follow from Debye-Gruneisen law and Lindemann's law:

$$\theta(V) = \theta_0 \left(\frac{V_0}{V} \right)^{1/2} \exp[3c_1(V_0^{1/3} - V^{1/3}) + \frac{c_2}{q}(V_0^q - V^q)] \quad (2.23)$$

$$T_M(V) = T_M(V_r) \left(\frac{V_r}{V} \right)^{1/3} \exp[6c_1(V_r^{1/3} - V^{1/3}) + \frac{2c_2}{q}(V_r^q - V^q)] \quad (2.24)$$

where θ_0 , $T_M(V_r)$ and V_r are, respectively, reference Debye temperature, melting temperature, and melting volume at $P=0$.

Johnson model

Johnson proposed a generic model for all materials to obtain thermodynamics of ionic contribution from low temperature solid region to ideal gas limit [47]. The model uses Debye model in solid region but interpolates through melting and the liquid regime to ideal gas regime, assuming that the specific heat at constant volume (C_{Vi}) drops monotonically from about $3R$ at melting point,

to $9R/4$ at five times melting temperature, and continuing to $3R/2$ at high temperatures. For $w \leq 1$, the thermal components E_{ti} and P_{ti} are described by Debye model i.e. Eq. (2.19) and (2.20). For $w \geq 1$, there are three regions, i.e. $1 \leq w \leq 5$, $5 \leq w \leq T_g$, $T_g \leq w$, depending upon the variation of C_{Vi} from melting point to ideal gas limit. Here T_g is the finite temperature at which C_{Vi} goes to $3R/2$.

For $1 \leq w \leq 5$,

$$E_{ti}(V, T) = E_D + E_1, \quad P_{ti}(V, T) = P_D + \frac{2\Gamma_F}{3} \frac{E_1}{V}, \quad E_1 = \frac{3}{32} \frac{k_B T}{AM_p} \left(2 - w - \frac{1}{w} \right) \quad (2.25)$$

For $5 \leq w \leq T_g$,

$$E_{ti}(V, T) = E_D + E_2, \quad P_{ti}(V, T) = P_D + \frac{2\Gamma_F}{3} \frac{E_2}{V} \quad (2.26)$$

$$E_2 = \frac{k_B T}{AM_p} \left(\frac{-3}{4} + b_1 \ln \left(\frac{w}{5} \right) - b_1 + \frac{5(b_1 + 9/20)}{w} \right)$$

where

$$b_1 = \frac{9}{32\{a_1 + 3/4 + (27/16)\ln 5\}} \quad \& \quad a_1 = -5.7 \quad (2.27)$$

For $T_g \leq w$,

$$E_{ti}(V, T) = E_D + E_3, \quad P_{ti}(V, T) = P_D + \frac{2\Gamma_F}{3} \frac{E_3}{V} \quad (2.28)$$

$$E_3 = \frac{k_B T}{AM_p} \left(\frac{-3}{2} + \frac{5(b_1 + 9/20)}{w} - \frac{T_g b_1}{w} \right), \quad T_g = 5e^{-3/(4b_1)}$$

2.3.3.3 Electronic thermal component

Electronic thermal component of energy and pressure is significant at temperatures reached in shock compression of porous materials. The hydrodynamic codes uses often Thomas-Fermi model to describe electronic thermal contribution [50–52]. However, the pressure and energy resulting from the approximations involved in this model need to be corrected in the low pressure-temperature range. For example, the low temperature specific heat constant predicted by the model differs significantly from experimental values. Further, employing pressure and energy values from in-line solution of the Thomas-Fermi equations is time consuming.

For low temperature limit (i.e. $T \ll T_f$ where T_f is the Fermi degeneracy temperature) the fitting formulas for P_{te} and E_{te} , obtained by Gilvarry from perturbation solution of Thomas-Fermi equation [54], are

$$E_{te}(V, T) = \frac{1}{2}\beta(V)T^2, \quad P_{te}(V, T) = \frac{\Gamma_e}{V}E_{te}(V, T) \quad (2.29)$$

where β is the coefficient of electronic specific heat, given by

$$\beta(V) = \beta_0(V/V_0)^{\Gamma_e}, \quad \beta_0 = \frac{4\pi^4}{(3\pi^2)^{2/3}} \frac{k_B^2 m_e}{h^2} N_e^{1/3} V_0^{2/3} \quad (2.30)$$

Here N_e is the number of free electrons per unit mass and h is the Planck constant. The detailed analysis carried out by Soviets [85], using perturbation solution of Gilvarry, Latter's data [55] for non-zero temperature, and experimental data, showed that $E_{te} \sim T^2$ up to the temperatures of the order of 30,000-50,000⁰ K. This consistency increases with increasing density because $T_f \sim V^{-2/3}$.

For $T \gg T_f$ a study of Latter's curves depicts that the energy due to thermal excitation of electrons becomes independent of volume and approaches an asymptotic value, approximated as

$$E_{te} = \frac{3}{2}\zeta T, \quad \zeta = \frac{0.85X^{0.59}}{1 + 0.85X^{0.59}}ZR, \quad X = \frac{T}{Z^{4/3}} \quad (2.31)$$

In the above equation ζ represents to effective gas constant for electrons and R is the gas constant (universal gas constant divided by atomic weight). The corresponding pressure is $P_{te} = \zeta T/V$.

McCloskey proposed the following fitting formulas for P_{te} and E_{te} , to provide a continuous transition from low temperature (where P_{te} and E_{te} vary as T^2) to high temperature i.e. ideal gas limit [53].

$$P_{te}(V, T) = \frac{1}{V} \frac{\zeta^2}{\Gamma_e \beta(V)} \log \cosh \left(\frac{\Gamma_e \beta T}{\zeta} \right), \quad E_{te}(V, T) = \frac{9\zeta^2}{4\beta(V)} \log \cosh \left(\frac{2\beta T}{3\zeta} \right) \quad (2.32)$$

Eq. (2.32) give accurate electronic pressure and internal energy over a wide

range of temperature and compression.

2.3.3.4 Model parameters for Cu

The parameters needed in this model are available from experimental data [7, 8, 53]. Zero temperature isotherm for Cu is parametrized using $V_0=0.112 \text{ cm}^3$, $B_0=134.8 \text{ GPa}$, $B'_0=5.193$ and $E_{coh}=3.48 \text{ eV/atom}$. Constants in Γ_s are: $c_1=1.87 \text{ (g/cm}^3)^{1/3}$, $c_2=2.31 \times 10^4 \text{ (g/cm}^3)^q$, and $q=4.7$. The reference values are $\Gamma_0=2.02$, $\theta_0=343 \text{ K}$, $T_M(V_r)=1358 \text{ K}$ and $V_r=0.119 \text{ cm}^3$. Electronic Gruneisen parameter Γ_e is in the range 0.6-0.8 and specific heat constant β_0 is about $1.1 \times 10^{-5} \text{ J/(g K}^2)$.

2.3.4 Calculation of χ_i , C_{Pi} , C_{Pe} and H_{te}

We have computed χ_i , C_{Pi} , C_{Pe} and H_{te} using the three component EOS mentioned above. Particularly, for C_{Pi} , we have considered Johnson ionic model since it incorporates more details of melting (no discontinuity at melting point as seen in Cowan model) and the temperature dependence of the C_{Vi} in the liquid regime. Omitting the electronic terms from Eqs. (2.15) and (2.16), we obtain C_{Pi} and $\chi_i=(P/C_{Pi})(\partial V/\partial T)_P$. Since C_{Pi} and χ_i vary rather slowly with P and T , we only compute them along the solid Hugoniot. In fact, C_{Pi} varies from $\sim 3Nk_B$ at low temperature, where N is the number of atoms per gram, to $(5/2)Nk_B$ at high temperature. It is also possible to calculate χ_i using experimental Hugoniot data of solid [66, 68].

With specified values of P and T , we invert Eq. (2.15) to obtain V and thereafter total enthalpy $H=E+PV$ using Eq. (2.16). Repeating the step without electronic terms gives H_c+H_{ti} and thereafter the electronic enthalpy $H_{te}=H-H_c-H_{ti}$ which is used in Eq. (2.11). We also obtain C_{Pe} in this manner with additional calculations for three temperatures in the neighborhood of T , numerical interpolation, and differentiation. We show below that H_{te} and C_{Pe} vary strongly with P and T and therefore this procedure is necessary to get good results.

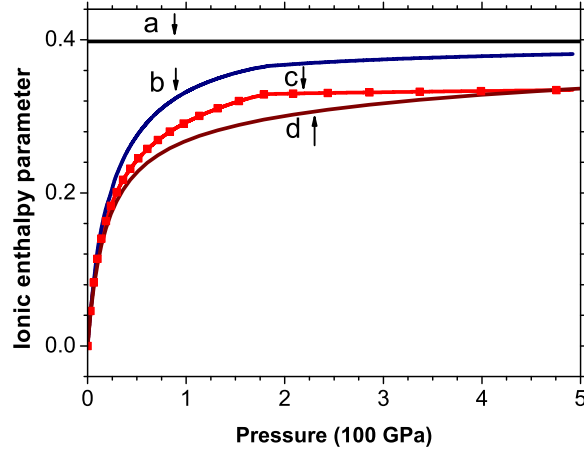


Figure 2.1: Variation of ionic enthalpy parameter with pressure for Cu. (a) $\chi_e = \Gamma_e / (\Gamma_e + 1)$ with $\Gamma_e = 0.66$. (b) Effective χ obtained using C_P weighting (see text below Eq. (2.8)). (c) χ_i obtained from 3-component EOS model. (d) $\chi_i = P\Gamma_s / K_s$ obtained using Γ_s (see Eq. (2.22)) and zero temperature isotherm for K_s .

2.4 Results

In this section we discuss the results of applications of the theory to porous Cu. Fig. 2.1 shows variation of ionic enthalpy parameter χ_i with respect to pressure along the solid Hugoniot. Variation χ_i along the zero temperature isotherm, obtained as $\chi_i = P\Gamma_s / K_s$, is also shown. Comparison of these two curves show the weak temperature dependence of χ_i because temperature on the Hugoniot varies up to $\sim 2 \times 10^4 K$. Maximum difference between these results is only about 10 percent at 180 GPa, and the curves merge at higher pressure as the zero temperature isotherm dominates there. The constant value of electronic parameter χ_e assuming $\Gamma_e = 0.66$ is also shown. We also show the effective χ parameter obtained with C_P weighting (see text below Eq. (2.8)). The ionic parameter χ_i starts off from very low values at low pressures and approaches a constant value of about 0.32 around 200 GPa and remains fairly constant thereafter. This is due to the melting transition and crossover to fluid phase at about this pressure. The effective χ parameter approaches χ_e for high pressures as C_{Pe} becomes more and more dominant in comparison to C_{Pi} (see Fig. 2.2).

Fig.2.2 shows the variation of constant pressure specific heats C_{Pi} and C_{Pe} along the Hugoniot of solid Cu. The steady increase of C_{Pe} is due to electrons

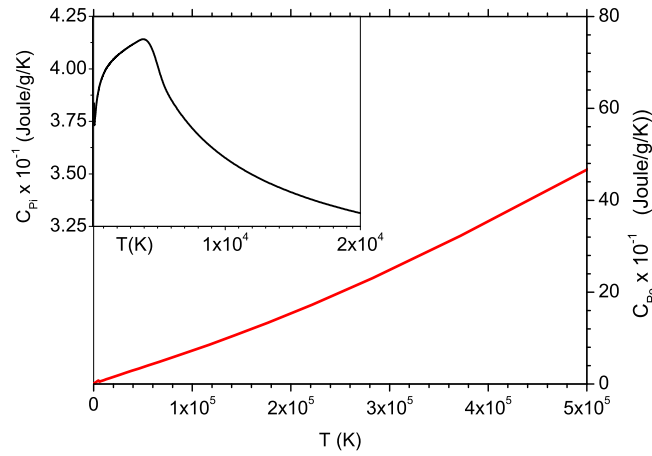


Figure 2.2: Variation of electronic specific heat C_{Pe} with temperature T along the Hugoniot for Cu, using 3-component EOS model. Insert figure shows ionic specific heat C_{Pi} obtained using 3-component EOS model.

produced via thermal ionization. The insert figure shows gradual decrease of C_{Pi} from its value in solid phase to that in fluid phase at around 5×10^3 K, and is due to the melting transition. The overall variation of C_{Pi} is much less compared to that of C_{Pe} . In fact, C_{Pi} varies only in the range 0.33-0.41 Joule/g K when temperature rises up to 2×10^4 K.

Fig. 2.3 shows the contribution of thermal electrons on the Hugoniot of porous Cu with initial porosity $\alpha_0=2$. The main figure shows P-V curve with and without thermal electron contribution. Experimental data is also shown for comparison [3]. The initial volume $V_{00} \sim 0.224 \text{ cm}^3$ is compacted to solid volume $V_0 \sim 0.112 \text{ cm}^3$ with pressure less than 3 GPa. Electronic terms begins to contribute to the Hugoniot at around 50 GPa. The experimental data compares much better when electronic effects are added. At 0.09 cm^3 there is about 25 % increase in pressure, from ~ 300 to ~ 380 GPa, due to electronic contributions. In fact this contribution would increase with pressure due to further thermal ionization, finally saturating only when Cu is fully ionized. The insert figure compares temperature on the Hugoniot with and without electronic contribution. The latter produces a dramatic reduction in temperature, for instance, by a factor of two for pressure ~ 300 GPa. This reduction is due to the generation of more free electrons via thermal ionization and consequent increase in specific heat.

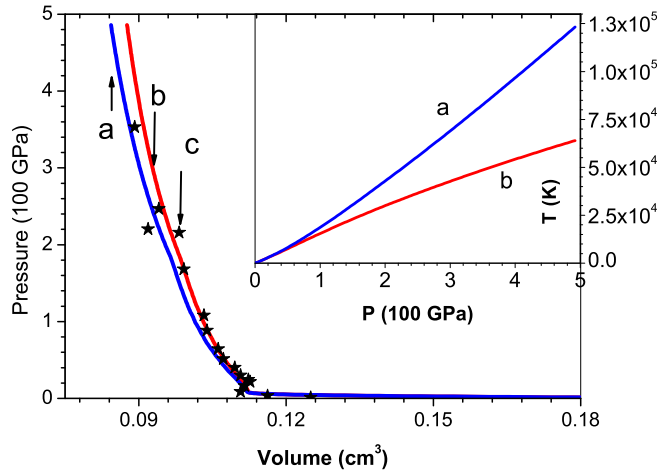


Figure 2.3: Comparison of P-V Hugoniot of porous Cu with porosity $\alpha_0=2$. (a) Without electronic contribution. (b) With electronic contribution. (c) Experimental data[3]. Insert figure shows temperature on the Hugoniot. (a) Neglecting electronic effects. (b) Including electronic effects.

Fig. 2.4 compares P-V Hugoniot curves for Cu with experimental data for a number of initial porosities. All results in this figure include electronic contribution, which has magnitudes similar to that in Fig. 2.3, though it increases at higher porosities. There is excellent agreement with data for $\alpha_0=1$ and 2. However, there are differences for $\alpha_0=3$ and $\alpha_0=4$. At still higher porosities $\alpha_0=7.2$ and $\alpha_0=10.03$ the trends at low pressures are good, but experimental data are limited. Anomalous expansion in the shocked states are evident for $\alpha_0 > 2$. We feel that better agreement with data at higher porosities would come about with improvements in modeling electronic enthalpy and specific heat. Electronic binding and thermal ionization are only described crudely in the present treatment. Furthermore, coexisting vapor-liquid phases also should be included for volume greater than V_0 .

Fig. 2.5 shows temperature vs. pressure on the Hugoniot of Cu for different initial porosities, and includes electronic contribution. Temperature rises from $\sim 1.5 \times 10^4$ K to almost 1.8×10^5 K for ~ 400 GPa pressure when porosity increases from $\alpha_0=1$ to $\alpha_0=10.03$. We have already shown (see Fig. 2.3) the need for accounting thermal electron contribution in temperature computations.

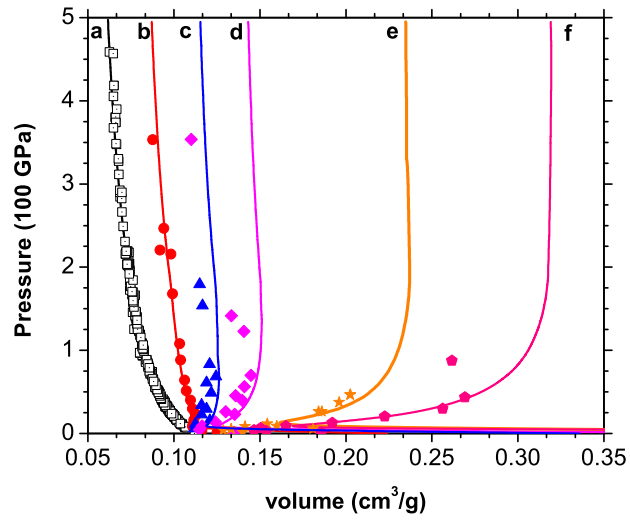


Figure 2.4: Comparison of P-V curves of porous Cu. (a) $\alpha_0=1$, (b) $\alpha_0=2$, (c) $\alpha_0=3$, (d) $\alpha_0=4$, (e) $\alpha_0=7.2$, (f) $\alpha_0=10.03$. Symbols are experimental data [3].

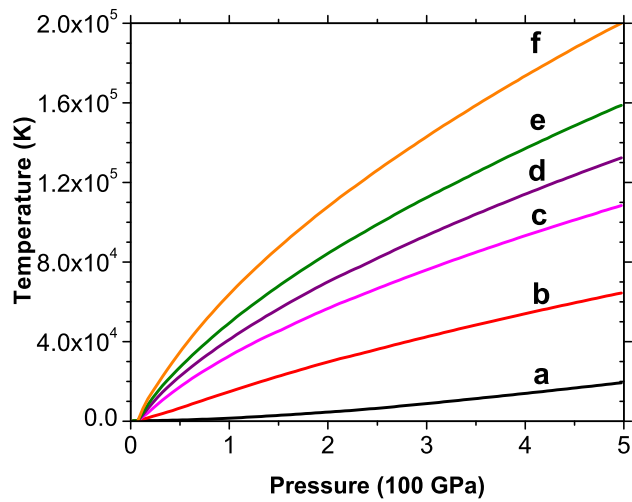


Figure 2.5: Variation of temperature with pressure on the Hugoniot of porous Cu. (a) $\alpha_0=1$, (b) $\alpha_0=2$, (c) $\alpha_0=4$, (d) $\alpha_0=5.45$, (e) $\alpha_0=7.2$, (f) $\alpha_0=10.03$.

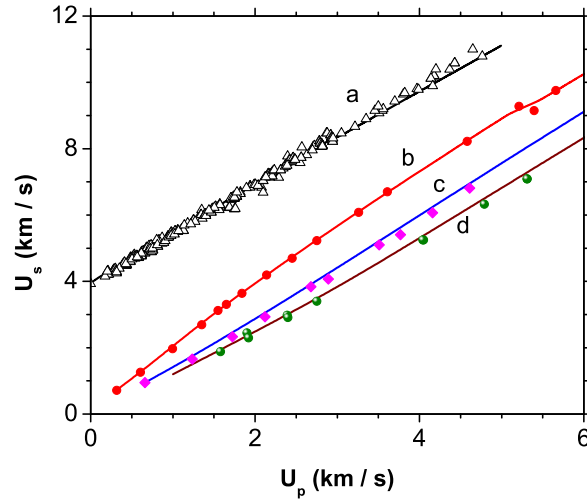


Figure 2.6: Comparison of U_s - U_p curves of porous Cu. (a) $\alpha_0=1$, (b) $\alpha_0=2$, (c) $\alpha_0=4$, (d) $\alpha_0=7.2$. Symbols are experimental data [3].

Finally, in Fig. 2.6 we compare shock speed U_s and particle speed U_p curves with experimental data for four initial porosities of Cu. While the curve for $\alpha_0=1$ is almost linear, there is significant curvature in the curves at low pressures and higher porosities. The curves approach the origin thereby showing that sound speed is nearly zero for higher porosities. This may be understood to be due to the presence of pore space which does not support wave propagation due to energy dissipation and heating.

2.5 Summary

In this chapter we have presented the correct set of equations within the generalized enthalpy-based EOS which includes thermal electronic effects explicitly. This approach needs simultaneous solution of P-V curve and temperature for computing the Hugoniot of porous materials. We have presented a simple method for practical implementation of the scheme. The method also needs constant pressure ionic and electronic specific heats and enthalpy parameters. We have outlined a three component EOS to compute these parameters. The method has been applied to porous Cu with different initial porosities and the results have been compared with experimental data. It is shown that thermal electronic contribution has a significant effect on determining the P-V curves

and temperature on the Hugoniot. The EOS model used here accounts for melting transition, however needs to be expanded further by including liquid-vapor transition. Electronic binding effects could also be improved for better predictions at higher porosities and pressures. Last, we have brought out and discussed the errors and ad hoc assumptions in two earlier papers (J. Appl. Phys., **92**, 5917, (2002), J. Appl. Phys., **92**, 5924, (2002)) using a similar approach.

Non-equilibrium theory employing enthalpy-based equation of state for binary solid and porous mixtures

3.1 Introduction

Shock wave propagation in mixtures of condensed materials is of considerable importance. Many practical applications such as shock initiation of heterogeneous explosives, attenuation of blast waves, material synthesis employing shock-induced chemical reactions, etc., have led to significant theoretical and experimental research in this area [63]. Mixtures prepared via compaction of powders are generally porous, which generate high temperatures on shock loading. Inclusion of effects of high porosity generates an additional dimension in thermodynamic modeling, even in the case of single component materials [58], [23].

The particulate nature of components in mixtures determines the time scales for equilibration of thermodynamic variables during shock propagation [86]. If particles are subjected to different pressures, equilibration would be reached at a typical time scale $\tau_1 \sim 5 \times$ (particle diameter/sound speed), which is about 1 ns for 1 μm particle, if we assume sound speed $\sim 5,000$ m/s [87]. Since this time is of the order of the shock rise time even for 100 μm size particles, it is reasonable to assume pressure equilibration during shock transit. Shock compaction experiments do not indicate the occurrence of different particle speeds in components [88]. However, differential production of microkinetic energy in the components due to interfacial friction has been invoked in mixture theories [89]. This turbulent energy would be very quickly dissipated in the particles, thereby providing an initial mechanism for non-equilibrium internal energy distribution. These arguments suggest that particle velocities

would also equilibrate within shock rise time scales. Then, due to different compressibility, it is possible to have unequal temperatures in the components immediately behind the shock front. Temperature equilibration occurs on a time scale $\tau_2 \sim (\text{diameter}^2 / \text{thermal diffusivity})$. Even for good conductors like Cu (with thermal diffusivity $\sim 110 \text{ mm}^2/\text{s}$), this time would be three orders larger than pressure equilibration time for $100 \mu\text{m}$ particle. Therefore it is necessary to assume non-equilibrium temperature after shock passage when particles sizes are $\gtrsim 50 \mu\text{m}$. Of course thermal equilibrium could be assumed for mixtures with much smaller size particles.

The earliest approaches to deal with shock compression of mixtures made use of the component Hugoniot. A simple method due to Russian researchers is to identify mixture volume, for a specified pressure, as the average of the Hugoniot volumes of components [90], [91]. This method, called an additivity rule, has been found to provide good accuracy to a large data base of mixture Hugoniot [63], [92]. McQueen et al. first obtained averaged zero temperature isotherms, deduced from the individual pressure-volume Hugoniot, and average Grüneisen parameter to derive the mixture Hugoniot [93]. Kinetic energy averaging method, which also relies on the component Hugoniot, first gets the average kinetic energy of the mixture and then deduces other parameters [94]. These methods do not address directly the issues of non-equilibrium aspects discussed earlier.

Since pressure and velocity equilibration is a valid approximation, it is natural to use pressure and temperature as independent variables in thermodynamic modeling. An approach based on the average Gibbs free energy, which provides correct mixture parameters, was developed early, although equilibrium conditions were assumed [87]. In an important work on mixture theory, Krueger and Vreeland showed that in non-thermal equilibrium conditions, the Rankine-Hugoniot conservations laws are insufficient, and an additional equation specifying partitioning of energy onto the components is needed [88]. In another pioneering work, Gavrilyuk and Saurel developed a method to incorporate microkinetic energy generation [89]. All these methods have been reviewed and discussed, together with inter-comparison of numerical results, recently [95].

Recently, Zhang and co-workers used the enthalpy-based equation of state (EOS) for Hugoniot of mixtures [76], [96]. After obtaining the average zero temperature isotherm, they simply followed the method for a single component material, and so do not consider non-equilibrium aspects at all. The enthalpy-based EOS, originally proposed by Rice and Walsh for water, employs pressure as independent variable in lieu of volume [67]. This approach is found to be well suited for single component materials with a wide range of porosity [66], [68], [6].

In this chapter we present the development of the generalized enthalpy-based EOS for binary mixtures, including non-equilibrium effects. Our method is close to that of McQueen et al. and makes use of average zero temperature isotherm as well as mixture parameters [93]. The Enthalpy-based approach is more suitable to discuss non-equilibrium effects as pressure equilibration is fast and so pressure can be treated as an independent variable. Furthermore, it is also the method of choice to treat shock Hugoniot of porous substances. A new feature of our method is that we obtain a term involving enthalpy differences in the EOS of the mixture. We propose to use single component criteria in determining energy partitioning on to the components, as also implied within the additivity rule [95]. Even though we find the magnitude of enthalpy differences to be small, our method provides a theoretical justification for the accuracy of averaging methods.

Section 3.2 describes generalized enthalpy-based EOS for binary mixtures, employing individual component EOS. In section 3.3 we derive the formulation of mixture Hugoniot and discuss the numerical method to compute equilibrium and non-equilibrium temperature on the Hugoniot of mixture. Also earlier approaches on mixture theory are mentioned. Application of our method to various binary mixtures, metallic, mixture of compounds, and porous mixtures are shown in section 3.4. We compare component temperatures with average temperature of the mixture, thereby obtaining an estimate of non-thermal equilibrium effects. Our practical implementation uses the zero temperature Birch-Murnaghan EOS model, which is known to be applicable to a variety of materials, and a simple thermal model. Finally, section 3.5 summarizes the

work.

3.2 Generalized enthalpy-based EOS for binary mixtures

The enthalpy parameter χ and constant pressure specific heat C_P are defined as $(\partial V/\partial T)_P = (\chi/P)C_P$ and $(\partial H/\partial T)_P = C_P$, respectively, where V is specific volume, T temperature, P pressure, and H specific enthalpy. The parameters χ and C_P for a mixture contain thermal ionic and electronic contributions of each component. It is possible to split the parameters into those of the components as $\chi C_P = \chi_1 w_1 C_{P1} + \chi_2 w_2 C_{P2}$ and $C_P = w_1 C_{P1} + w_2 C_{P2}$, where χ_1 and χ_2 are the enthalpy parameters of the components and w_1 and $w_2 = 1 - w_1$ are their weight fractions. Similarly, C_{P1} and C_{P2} are the constant pressure specific heats. This decomposition also shows that the effective χ of the mixture is to be obtained by weighting the enthalpy parameters with constant pressure specific heats. A similar conclusion follows for Grüneisen parameter, where averaging needs to be done with constant volume specific heats. For metallic mixtures, it is also desirable to separate the electronic components, as we shall do below.

3.2.1 Individual component EOS

We assume that properties of the shocked material like pressure, particle speed, and shock speed are uniform within the mixture. However, non-equilibrium thermal effects lead to different thermal enthalpies, which depend on component temperatures T_1 and T_2 , respectively. The components have specific volumes V_1 and V_2 . Integrating the defining relations from zero to T_k , specific volume V_k , and enthalpy H_k of the k^{th} component are expressed as

$$V_k = V_{ck}(P) + \frac{1}{P} \int_0^{T_k} (\chi_{ik} C_{Pik} + \chi_e C_{Pek}) d\tau \quad (3.1)$$

$$H_k = H_{ck}(P) + \int_0^{T_k} (C_{Pik} + C_{Pek}) d\tau. \quad (3.2)$$

Here the reference state parameters, V_{ck} and $H_{ck}=E_{ck}+P V_{ck}$, denote, respectively, the zero temperature specific volume and specific enthalpy of the component at pressure P . Note that V_{ck} is to be obtained by inverting the zero-temperature pressure equation, $P_{ck}(V_{ck})=P$. We have also introduced ionic enthalpy parameter χ_{ik} and specific heat C_{Pik} and their electronic counterparts χ_e and C_{Pe} .

Generally it is assumed that the enthalpy parameters χ_{ik} in the solid phase of the component is independent of temperature [66]. We have tested this assumption for four elements by comparing χ_{ik} on their respective Hugoniot and the zero temperature isotherms (see Fig. 3.1). Temperatures on the Hugoniot at about 220 GPa are in the range 6000 K to 7500 K for these elements while the thermal component of χ_{ik} is between 8 to 12 %. In addition, χ_{ik} occurs as the ratio $\chi_{ik}/(2-\chi_{ik})$ in the expression for P-V Hugoniot (see Eq. (3.9)), which reduces the actual effect of this difference to ~ 4 to 6 %. Therefore the assumption that temperature dependence of χ_{ik} is weak is justified, and so we use χ_{ik} computed on the zero temperature isotherm to obtain all results in this paper.

This approach is similar to using the Grüneisen's parameter along the zero temperature isotherm [23]. In fact χ_{ik} can be computed along any suitable P-V curve; it has been computed along the solid Hugoniot earlier [66], [6].

It is customary to use a constant electron Grüneisen parameter Γ_e in the range 0.6-0.8 [57]. Then the general definition yields $\chi_e=\Gamma_e/(1+\Gamma_e)$. We assume that $\chi_{ik}(\tau)$ is weakly dependent on temperature, based on the above discussion, and so replace it by $\chi_{ik}(T_k)$ within the integral in Eq. (3.1). Then, Eqs. (3.1) and (3.2) can be combined together to obtain the enthalpy-based EOS:

$$V_k = V_{ck}(P) + \frac{\chi_{ik}}{P} H_{tik}(P, T_k) + \frac{\chi_e}{P} H_{tek}(P, T_k), \quad k = 1, 2. \quad (3.3)$$

where H_{tik} and H_{tek} , respectively, denote the specific ion thermal enthalpy and electron enthalpy of k^{th} component. This equation explicitly accounts for thermal electron contributions to total volume.

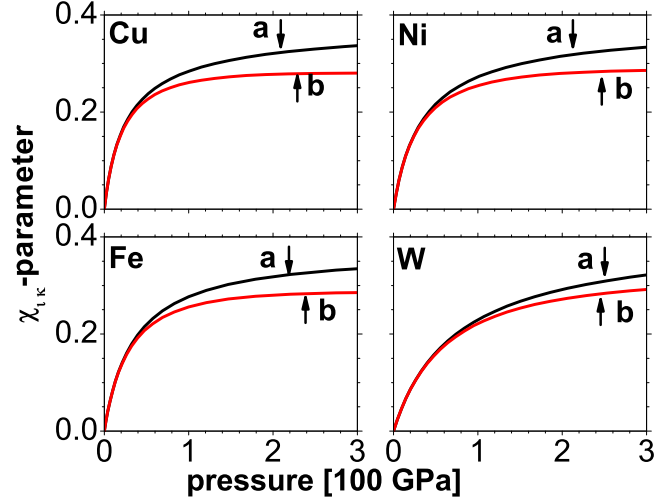


Figure 3.1: Variation of χ_{ik} with pressure for Cu, Fe, W, and Ni. χ_{ik} on the Hugoniot (curves-a). χ_{ik} obtained on the Birch-Murnagan isotherms (curves-b).

3.2.2 Binary mixture EOS

It is necessary to average the component volumes to derive an EOS for the mixture. So, multiplying Eq. (3.3) with the weight fraction w_k of the k^{th} component and summing over k we obtain the enthalpy EOS for the mixture:

$$V = V_c + \frac{\chi_{i1}}{P} w_1 H_{ti1} + \frac{\chi_{i2}}{P} w_2 H_{ti2} + \frac{\chi_e}{P} H_{te} \quad (3.4)$$

where $V_c = w_1 V_{c1} + w_2 V_{c2}$ is the average zero temperature specific volume. Similarly, $H_{te} = w_1 H_{te1} + w_2 H_{te2}$ is the average specific electron enthalpy. Expressing $w_1 H_{ti1} = H - H_c - w_2 H_{ti2} - H_{te}$, we get

$$V = V_c + \frac{\chi_{i1}}{P} (H - H_c) + \frac{1}{P} (\chi_e - \chi_{i1}) H_{te} + \frac{1}{P} (\chi_{i2} - \chi_{i1}) w_2 H_{ti2} \quad (3.5)$$

Here $H_c = w_1 H_{c1} + w_2 H_{c2}$ is the average of zero temperature specific enthalpy. The last term in this equation contains the enthalpy difference of the components. Eq. (3.5) has one defect; it is not symmetric with respect to components 1 and 2. However, a similar expression for V is obtained by substituting $w_2 H_{ti2} = H - H_c - w_1 H_{ti1} - H_{te}$ in Eq. (3.4):

$$V = V_c + \frac{\chi_{i2}}{P} (H - H_c) + \frac{1}{P} (\chi_e - \chi_{i2}) H_{te} + \frac{1}{P} (\chi_{i1} - \chi_{i2}) w_1 H_{ti1} \quad (3.6)$$

Multiplying Eq. (3.5) and Eq. (3.6) with weight factors f_1 and $f_2=1-f_1$, respectively, and adding the resulting equations yields

$$V = V_c + \frac{\bar{\chi}_i}{P}(H - H_c) + \frac{1}{P}(\chi_e - \bar{\chi}_i)H_{te} + \frac{1}{P}(\chi_{i1} - \chi_{i2})(f_2w_1H_{ti1} - f_1w_2H_{ti2}) \quad (3.7)$$

This equation is symmetric with respect to the component parameters and so is better suited for applications. Some important features of Eq. (3.7) are the following:

1. First, the average enthalpy parameter $\bar{\chi}_i=f_1\chi_{i1}+f_2\chi_{i2}$ occurs naturally in the second and third terms.
2. The last term contains differences of χ_{i1} and χ_{i2} as well as ion thermal enthalpies. Hence, it would be a small correction to the preceding three terms.
3. Without the last term, this equation exactly resembles that of a single component system [6].
4. The choice $f_1=w_1$ and $f_2=w_2$, yields a simple average enthalpy parameter $\bar{\chi}_i= w_1\chi_{i1}+w_2\chi_{i2}$, which is similar to the average Grüneisen parameter of McQueen et al. [93].
5. The choice $f_k=w_kC_{Pik}/\bar{C}_{Pi}$ ($k=1, 2$), where $\bar{C}_{Pi}= w_1C_{Pi1}+w_2C_{Pi2}$, gives C_P weighted enthalpy parameter: $\bar{\chi}_i=(w_1C_{Pi1}\chi_{i1}+w_2C_{Pi2}\chi_{i2})/\bar{C}_{Pi}$. We pointed out in the beginning that thermodynamic definitions leads to this averaging of χ_{ik} (see also Ref.[87]).
6. With both choices, the product w_1w_2 , which has a maximum value $1/4$, comes out as a common factor in the last term and decreases its magnitude.
7. In equilibrium condition, when both components are at the same temperature, the last term vanishes with the second choice of f_k , if C_{Pik} are constants. This point is important for low pressure studies of mixtures.

3.3 Binary mixture Hugoniot

The Hugoniot of the mixture is obtained by combining Eq. (3.7) with the expression for enthalpy along the Hugoniot:

$$H = E_{00} + \frac{1}{2}P_{00}(V_{00} - V) + \frac{1}{2}P(V_{00} + V) \quad (3.8)$$

where E_{00} and P_{00} are, respectively, the energy and pressure at initial volume V_{00} . The resulting P-V curve is

$$\begin{aligned} V = & 2V_c \frac{1 - \bar{\chi}_i}{2 - \bar{\chi}_i^*} + \frac{2}{P} \frac{\chi_e - \bar{\chi}_i}{2 - \bar{\chi}_i^*} H_{te} + \frac{\bar{\chi}_i}{2 - \bar{\chi}_i^*} \left(V_0(1 + P_0/P) + \frac{2}{P}(E_0 - E_c(V_c)) \right) \\ & + \frac{2}{P} \frac{\chi_{i1} - \chi_{i2}}{2 - \bar{\chi}_i^*} w_1 w_2 \frac{1}{C_P} (C_{P2} H_{ti1} - C_{P1} H_{ti2}) \end{aligned} \quad (3.9)$$

Here we have used C_P weighting introduced above, and $\bar{\chi}_i^* = \bar{\chi}_i(1 - P_{00}/P)$. Neglecting the last term containing ion thermal enthalpy difference, for reasons pointed out above, yields a P-V curve similar to that of a single material [6]. This finding provides a theoretical justification for simply using average parameters in mixture theory. However, we shall also discuss below a scheme to compute this term, though it makes only a small contribution to V . In Fig. 3.2 we show its magnitude relative to the preceding terms for three cases of W-Cu mixture. Over a pressure range of ~ 300 GPa, the maximum difference is $\lesssim 0.035\%$. Therefore, retaining the first three terms in this expression would provide accurate results for practical applications. This estimate of the enthalpy difference term provides an error estimate in the P-V curve. However, temperatures of the components are needed in other applications involving thermally induced chemical reactions, structural transitions, dissociation, etc.

Notwithstanding the above discussion, there could be situations where the enthalpy difference term is significant. Such cases would correspond to $w_1 w_2 \sim 1/4$, largely different values for χ_{ik} , specific heats C_{Pik} and temperatures T_k for the components.

Porous mixtures are characterized by porosity parameter $\alpha_0 = V_{00}/V_0$, where V_{00} is the volume including that of pores. For using Eq. (3.9), the zero temperature volumes V_{ck} ($k=1, 2$) need to be extended to the region $V_{0k} \leq V_{ck} \leq \alpha_0 V_{0k}$ where

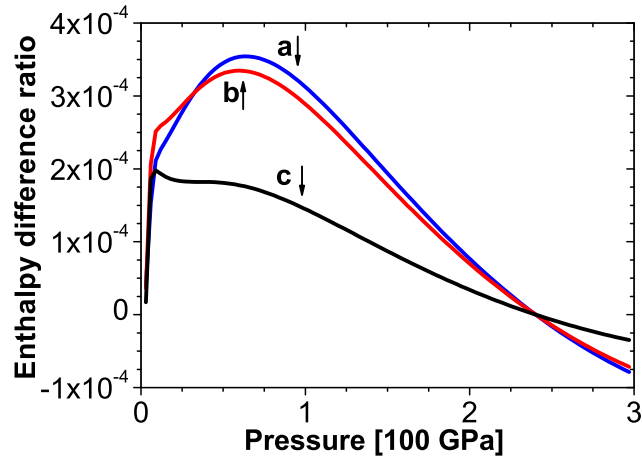


Figure 3.2: Ratio of enthalpy difference term to those preceding it in Eq. (3.9) for three W-Cu mixtures. $w_1/w_2=76/24$ (curve-a), $w_1/w_2=55/45$ (curve-b), $w_1/w_2=25/75$ (curve-c).

V_{0k} is the initial volume of the solid component. A method to effect this is to use a parametrization of $\alpha(P)$ and the P- α model [12],[58]. This approach is now well known for single component materials [6].

3.3.1 Other approaches

As there is a detailed review of the methods of mixture theory by Petel and Jette [95], together with numerical comparisons, we provide only a brief account of these approaches here. Russian researchers developed a method by associating the mixture volume, for a specified pressure, with average Hugoniot volumes of components [90], [91]. The method of McQueen et al., which is based on the Mie-Grüneisen EOS, employs weighted average (using w_1 and w_2) of the zero temperature isotherm and the Grüneisen parameter for any pressure [93]. Then pressure is calculated using the mixture volume and energy on the Hugoniot, which is analogous to Eq. (3.8). Duvall and Taylor developed a theory for mixtures in thermal equilibrium, starting with an average Gibbs free energy [87]. This approach computes equilibrium temperature and naturally leads to C_V (constant volume specific heat) weighted average Grüneisen parameter. Kinetic energy averaging scheme obtains the average kinetic energy of the mixture, using individual kinetic energies of the component Hugoniot, and then deduces other parameters via conservation equations [94]. The approach by Zhang et al. using enthalpy-based EOS, simply uses the

average zero temperature isotherm, and thereafter follows the procedure for single materials [76],[96]. All the parameters of the mixture, including $\bar{\chi}$, are based on the average zero temperature isotherm. Even though these schemes do not address non-equilibrium aspects, they do imply certain assumptions in this regard. For example, the volume or kinetic energy averaging schemes neither assume velocity nor thermal equilibration. However, the method of McQueen et al. assumes velocity equilibration as it uses energy on the mixture Hugoniot, while the methods of Duvall and Taylor and Zhang et al. assume both velocity and thermal equilibration.

Krueger and Vreeland developed a scheme using the Mie-Grüneisen EOS to investigate non-thermal equilibrium effects on mixture Hugoniots [88]. These authors showed that Rankine-Hugoniot conservation laws for the mixture, which automatically assume velocity equilibration, need to be supplemented with an additional equation specifying partitioning of energy onto the components. However, they found that the P-V Hugoniot is quite insensitive to the division of Hugoniot energy.

The averaging methods mentioned above use the *additivity rule* or *single component criteria*, which is Eq. (3.8), or its equivalent form in energy, applied to each component [90], [91], [94]. Thus Eq. (3.8) for enthalpy is replaced by the component enthalpy

$$H_k = E_{00k} + \frac{1}{2}P_{00}(V_{00k} - V_k) + \frac{1}{2}P(V_{00k} + V_k) \quad (3.10)$$

where E_{00k} ($k=1, 2$) is the energy at initial volume V_{00k} of the k^{th} component. Similarly, V_k is the volume after shocking to pressure P . Hugoniots of a large number of mixtures have been compared within this approximation [63]. A theoretical derivation of this rule has been provided recently for low shock pressures [92]. These authors also applied this approximation to twelve mixtures together with detailed comparisons with experimental data. We also point out that use of Eq. (3.10) implies neither velocity nor thermal equilibration in the mixture. The work related to generation of microkinetic energy in the components and analysis of the resulting non-equilibrium energy distribution employs an extended single component criteria [89].

The *single component criteria*, together with enthalpy-based EOS in Eq. (3.3), leads to the Hugoniot of the components:

$$V_k = 2V_{ck} \frac{1 - \chi_{ik}}{2 - \chi_{ik}^*} + \frac{2}{P} \frac{\chi_e - \chi_{ik}}{2 - \chi_{ik}^*} H_{tek} + \frac{\chi_{ik}}{2 - \chi_{ik}^*} \left(V_{00k} (1 + P_{00}/P) + \frac{2}{P} (E_{00k} - E_{ck}) \right) \quad (3.11)$$

for $k=1,2$. It is important to note that summing over k , with weight factors f_1 and f_2 , *does not* yield Eq. (3.9). Thus, the method using just averaging of the component Hugoniot is different from our approach, in spite of the numerical accuracy of the former [95]. Also, note that using Eq. (3.11), the component kinetic energies and the average mixture kinetic energy can be readily computed for use in the kinetic energy averaging method [94].

3.3.2 Determination of temperature in binary mixture

To close Eq. (3.9) for the mixture volume, non-equilibrium enthalpies $H_{tk}(P, T_k)$ are needed. These are readily determined once temperatures T_k are obtained by solving the equations:

$$\frac{d}{dP} T_k - \frac{\chi_k}{P} T_k = \frac{0.5 Z_k}{w_k C_{Pk}} \left((V_{00} - V) + (P - P_{00}) dV/dP \right) \quad (3.12)$$

for $k=1,2$, where χ_k and C_{Pk} includes ionic and electronic contributions. These equations are similar to the Walsh-Christian differential equation, although there volume is independent variable [81]. Here, Z_k is the fraction of enthalpy on the Hugoniot shared by the k^{th} component. These fractions are unknown, and thus need to be assumed a priori to close the system of equations [88]. *We therefore propose to use the single component criteria to determine these temperatures.* Then Eq. (3.12) is replaced by

$$\frac{d}{dP} T_k - \frac{\chi_k}{P} T_k = \frac{0.5}{C_{Pk}} \left((V_{00k} - V_k) + (P - P_{00}) dV_k/dP \right) \quad (3.13)$$

for $k=1, 2$. Temperatures obtained from the solution of these equations is used to evaluate the last term in Eq. (3.9). After determining the P-V curve of the mixture, we can also determine an average temperature $T=T_1=T_2$ obtained by

summing Eq. (3.12) over k :

$$\frac{d}{dP}T - \frac{\bar{\chi}}{P}T = \frac{0.5}{C_P} \left((V_{00} - V) + (P - P_{00})dV/dP \right). \quad (3.14)$$

where $\bar{\chi} = (\chi_1 w_1 C_{P1} + \chi_2 w_2 C_{P2}) / C_P$ is the average enthalpy parameter and $C_P = w_1 C_{P1} + w_2 C_{P2}$ is the specific heat of the mixture. A numerical method could be used to solve differential equations like Eqs. (3.13) or (3.14).

3.3.3 Numerical method

Using forward differencing, Eq. (3.14) can be written in discrete form as:

$$C_{P,n}(1 - \bar{\chi}_n \Delta P / P_n) T_n = C_{P,n} T_{n-1} + 0.5 \left((V_{00} - V_n) \Delta P + (P_n - P_{00})(V_n - V_{n-1}) \right) \quad (3.15)$$

Here the subscript n on different variables denotes their respective values at $P_n = P_{00} + n \Delta P$ where ΔP is an increment in pressure, and $n=1, 2, 3$ etc. Eq. (3.15) have to be evaluated at each P_n . An iteration method is needed at each P_n if electronic terms are treated explicitly because H_{te} depends on T_n [6]. An identical method can be used to solve for T_k from Eq. (3.13).

3.4 Applications

The main result of this work is Eq. (3.9) for the mixture volume. Its application needs a model for zero temperature isotherm, enthalpy parameters and constant pressure specific heats. We already discussed calculation of shock temperatures of the components once these parameters are available. Our aim here to apply the formulation and compare the results with experimental Hugoniot data on mixtures, which are generally available for pressures $\lesssim 250$ GPa [4], [5]. In this region, explicit accounting of thermal electron effects are unnecessary, and hence we do not consider the second term in Eq. (3.9), instead use effective χ_k and C_{Pk} .

3.4.1 EOS model

There are several formulations for the zero temperature isotherm. We use the finite strain Birch-Murnaghan formula for pressure, energy, and bulk modulus

[33], which are given by:

$$\begin{aligned} P_c &= 3B_0f(1+2f)^{5/2}(1+2\zeta f) \\ E_c &= -E_b + (9/2)B_0V_0f^2(1+(4/3)\zeta f) \\ B_s &= B_0(1+2f)^{5/2}(1+7f+4\zeta f+18\zeta f^2) \end{aligned} \quad (3.16)$$

Here, B_0 , B'_0 , and E_b are, respectively, the bulk modulus, its pressure derivative, and cohesive energy at V_0 and $P=0$. Furthermore, the strain parameter is defined as $f=0.5((V_0/V)^{2/3}-1)$ and $\zeta=3(B'_0-4)/4$. The index k on the constants is omitted in this section for simplicity of notation.

For a given pressure P , Eq. (3.16) is numerically inverted to obtain $V_c(P)$. This is easily effected using an iteration method (starting with $X=1$) after rewriting it as

$$X = \left(X^{5/3} + 8P/(B_0(12 + 9(B'_0 - 4)(X^{2/3} - 1))) \right)^{3/7} \quad (3.17)$$

where $X=V_0/V$. Then, the definition of the enthalpy parameter yields $\chi=PV_c/B_s(V_c)$. For the Grüneisen parameter we use the expression $\Gamma=\Gamma_0 (V/V_0)+(2/3) (1-V/V_0)^2$ where Γ_0 is its value at V_0 [97], [7].

For systems subjected to high compression and pressures, it is more appropriate to use the EOS due to Vinet et al. [36], [37] which is known to be accurate even in the TPa range [41].

For the thermal component of enthalpy, we assume that C_V is a constant, and the standard expressions $E_t=C_V(T-T_0)$ and $P_t=(\Gamma/V)E_t$ [37], [41]. Constant pressure specific heat C_P is then readily computed using the expression $C_P=C_V(1 + T\Gamma\alpha_P)$, where α_P is the volume expansion coefficient. In Fig. 3.3, we show the temperature dependence of C_P for four elements. Variation in C_P is less than 10 % over 20000 K for these elements. Therefore it is reasonable to assume a constant value of C_P , for low pressure applications, in calculating thermal contributions. This formulation is now applied to five different types of mixtures. Material parameters used in calculations are given in Table 3.1. More detailed thermal models, including melting and electronic effects, can be readily employed if necessary [6].

Table 3.1: Material Parameters for Hugoniot calculations. Units: ρ_0 in g/cm^3 , B_0 in 100 GPa and C_V in $\text{J}/\text{g K}$

Material	ρ_0	B_0	B'_0	Γ_0	C_V
Iron	7.877	1.63	4.5	1.81	0.450
Copper	8.93	1.348	5.193	2.0	0.385
Nickel	8.875	1.79	5.0	2.0	0.440
Calcite	2.665	0.365	4.72	2.3	0.82
Water	1.0	0.03	6.0	1.5	4.18
Epoxy	1.2	0.094	4.76	1.43	1.0
Paraffin	0.917	0.0893	4.88	1.87	2.13
Carbon	2.24	0.33	7.0	0.28	0.71
Enstatite	3.01	0.82	3.2	1.14	0.82
Periclase	3.584	1.5	4.48	2.49	0.93
Forsterite	3.201	1.06	3.8	1.29	0.843
Titanium	4.51	1.06	3.708	1.33	0.54
Tungsten	19.3	3.25	3.92	1.8	0.134
Aluminum	2.7	0.728	4.365	2.1	0.9
Ta-Carbide	14.21	3.25	3.5	1.6	0.19

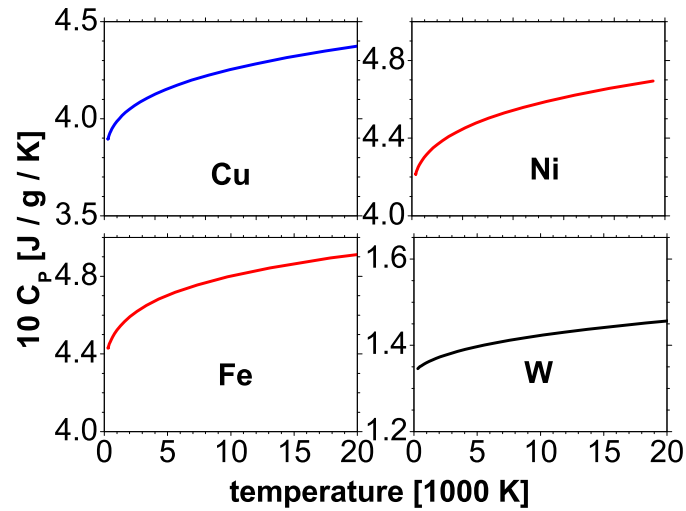


Figure 3.3: Variation of C_P with temperature along the Hugoniot of Cu, Fe, W, and Ni within the EOS model.

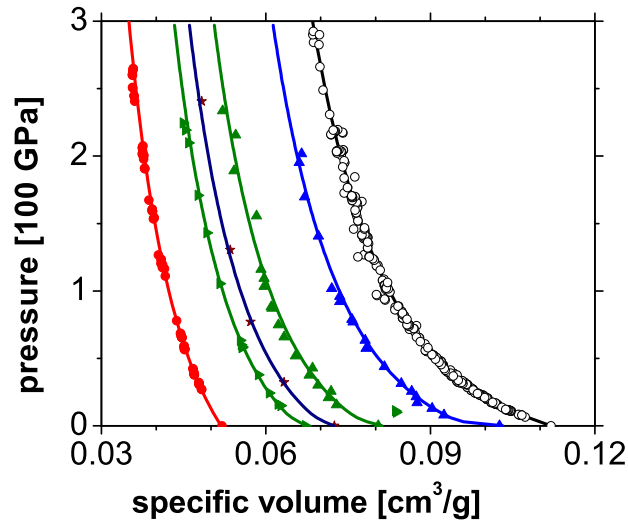


Figure 3.4: Pressure-volume Hugoniot of W-Cu mixtures. Curves from left to right are for: pure W, $w_1/w_2=76/24$, $w_1/w_2=68/32$, $w_1/w_2=55/45$, $w_1/w_2=25/75$ and pure Cu. Experimental data (symbols) are from Ref.[4].

3.4.2 Metallic mixtures

Pressure-volume Hugoniots for four compositions, $w_1/w_2=76/24$, $68/32$, $55/45$, $25/75$ of W-Cu mixture are shown in Fig. 3.4 together with experimental data [4], [5]. The Hugoniots of pure W and Cu are also shown. The gradual evolution of tungsten Hugoniot to that of copper is clearly evident. In Fig. 3.5 we show temperature vs. pressure for the four mixture compositions. Average temperature as well as component temperatures are shown for comparison. It is seen from Eqs. (3.13) or (3.14) that temperature depends mainly on the interplay between volume change, compressibility, and specific heat. The temperature of Cu component is more than that of W because of higher compressibility through W has a lower specific heat. So the average temperature reduces as the weight fraction of W increases due to decrease of compressibility. However, a reduction of specific heat seems to increase the average temperature for composition $w_1/w_2 = 25/75$ in comparison to that of Cu. Shock speed (U_s) vs. particle speed (U_p) results are compared with experimental data in Fig. 3.6. Our results follow the data quite well and also brings out the increase in shock speed with weight fraction W for the same particle speed. Slight initial curvature of the U_s - U_p curves, which is due to different compressibility of the components, is also reproduced.

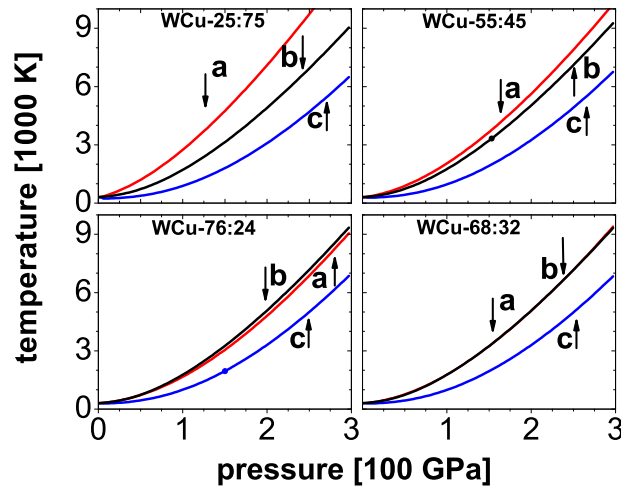


Figure 3.5: Temperature-pressure curves for W-Cu mixtures. Average temperature (curve-a), temperature of Cu (curve-b), temperature of W (curve-c). Curve-a and curve-b merged together for $w_1/w_2=68/32$.

In Fig. 3.7 we show the P-V Hugoniot of pure Ni and Fe-Ni mixture composition $w_1/w_2=74/26$. Data for Fe is not shown because it is quite close to that of the mixture. Good agreement with experimental data is noted here also. Hugoniot temperatures of Ni and three mixture Fe-Ni compositions, $w_1/w_2=74/26$, $82/18$, $90/10$, are shown in Fig. 3.8. Average temperatures are closer to those of Fe because of the composition. Comparison of shock speed vs. particle speed curves with experimental data for Ni, Fe, and the three mixture compositions, in Fig. 3.9, also shows good agreement. Linear relations for the components and slight initial curvature for mixtures are evident in these cases also.

3.4.3 Mixtures of compounds

In Fig. 3.10 we show pressure-volume Hugoniot of the mineral calcite (CaCO_3), calcite-water mixture of composition $w_1/w_2=90/10$ and pure water. Mixture results are closer to those of calcite because of the composition. Experimental data compares well with calculated results. The enthalpy-based EOS, originally developed for water, is providing good results [67]. Temperature vs. pressure curves, given in Fig. 3.11, show that temperatures of calcite and the mixture are close, as expected. Larger volume change in the Hugoniot of water

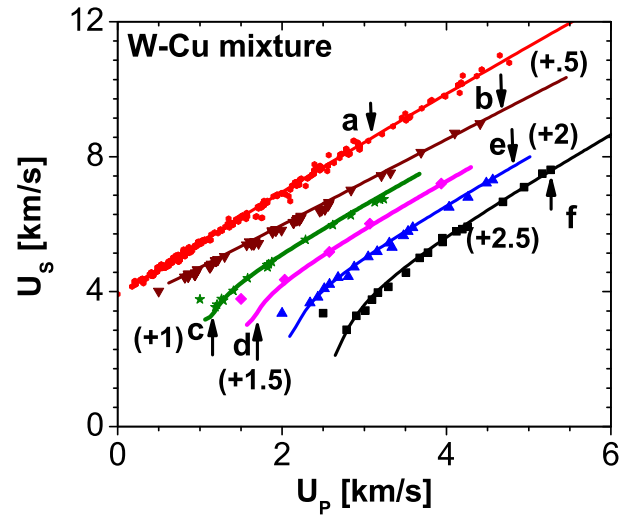


Figure 3.6: Shock speed (U_s) vs. particle speed (U_p) for pure Cu (curve-a), pure W (curve-b), $w_1/w_2=76/24$ (curve-c), $w_1/w_2=68/32$ (curve-d), $w_1/w_2=55/45$ (curve-e), $w_1/w_2=25/75$ (curve-f). Experimental data (symbols) are from Ref.[4]. Curves b to f are shifted to right by 0.5 km/s successively for clarity.

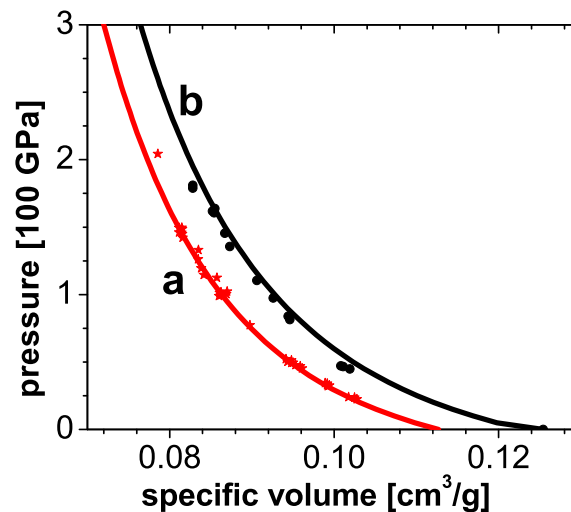


Figure 3.7: Pressure-volume Hugoniot of Ni (curve-a) and Fe-Ni mixture with $w_1/w_2=74/26$ (curve-b). Experimental data (symbols) are from Ref.[4].

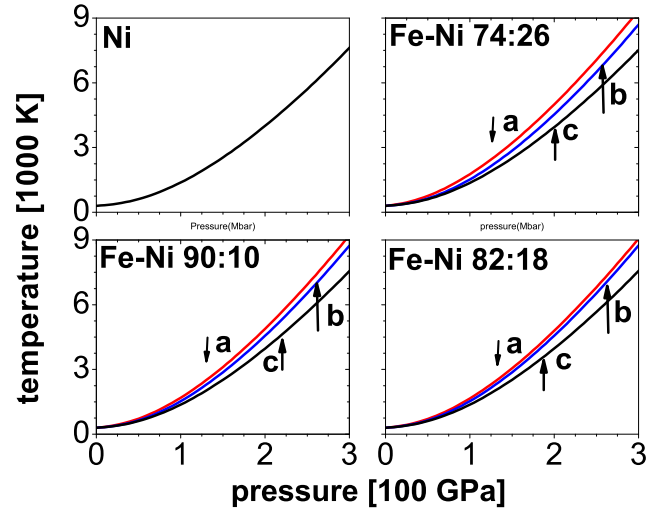


Figure 3.8: Temperature-pressure curves for Fe-Ni mixtures. Average temperature (curve-a), temperature of Fe (curve-b), temperature of Ni (curve-c).

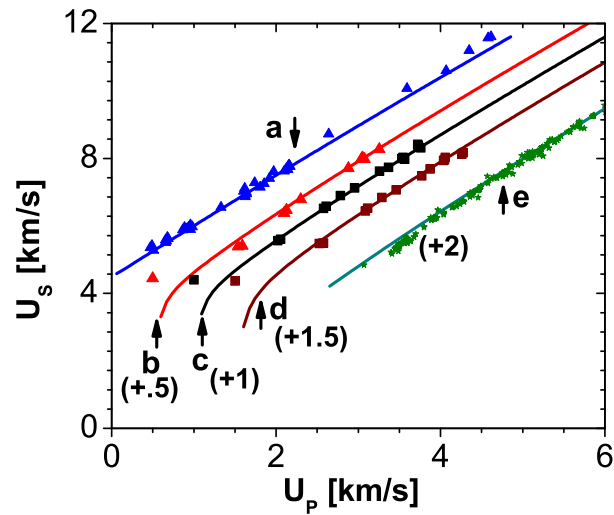


Figure 3.9: Shock speed (U_s) vs. particle speed (U_p) for pure Ni (curve-a), $w_1/w_2=90/10$ (curve-b), $w_1/w_2 = 82/18$ (curve-c), $w_1/w_2 = 74/26$ (curve-d), and pure Fe (curve-e). Experimental data (symbols) are from Ref.[4]. Curves b to e are shifted to right by 0.5 km/s successively for clarity.

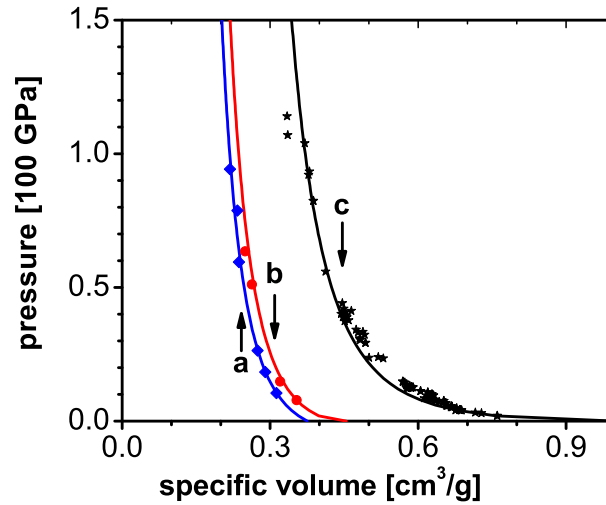


Figure 3.10: Pressure-volume Hugoniot of calcite (curve-a), calcite-water mixture with $w_1/w_2=90/10$ (curve-b), and water (curve-c). Experimental data (symbols) are from Ref.[4].

is compensated with its comparatively larger specific heat (4.18 to be compared with 0.8 J/g/K for calcite). Finally, shock speed vs. particle speed curves, shown in Fig. 3.12, also show good agreement with experimental data. The initial curvature in the mixture data is properly brought out in calculated results.

Next we consider a mixture where the components have quite different densities - paraffin and tungsten. The pressure volume Hugoniots for two compositions of paraffin (density ~ 0.92 g/cm³) with W (density ~ 19.3 g/cm³) are shown in Fig. 3.13. Agreement with experimental data is quite good for pure materials and two compositions $w_1/w_2=16/84$ and $w_1/w_2=34/66$. Data for mixtures stay closer to those of tungsten due to the large density difference. Tungsten is almost incompressible in the pressure range shown. Temperatures on the Hugoniot are given in Fig. 3.14. Average mixture temperature is closer to that of paraffin and tungsten temperature is much lower due to smaller volume change. Results of shock speed vs. particle speed for paraffin, W and two mixtures, shown in Fig. 3.15, also follow the experimental results closely. Note that doubling the fraction of paraffin has only a negligible effect on shock speeds.

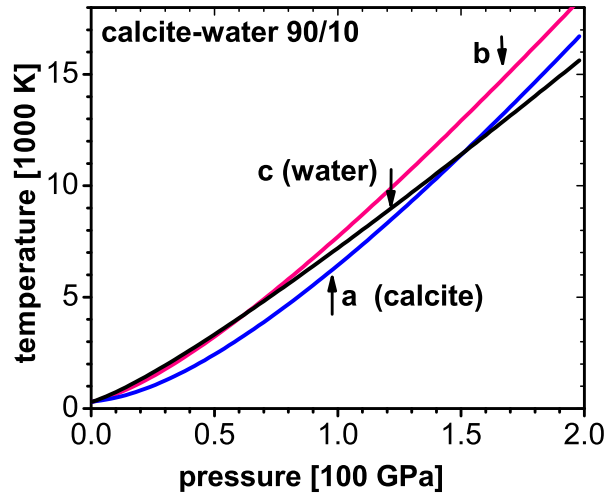


Figure 3.11: Temperature-pressure curves for calcite-water mixture with $w_1/w_2=90/10$. Temperature of calcite (curve-a), average temperature (curve-b), temperature of water (curve-c).

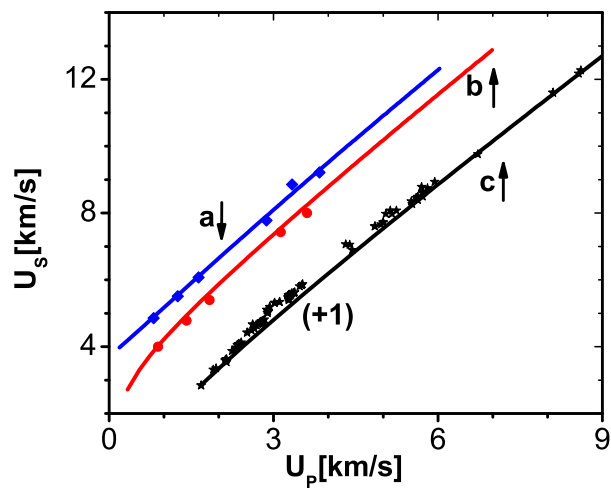


Figure 3.12: Shock speed (U_s) vs. particle speed (U_p) for calcite (curve-a) calcite-water mixture with $w_1/w_2=90/10$ (curve-b) and water (curve-c). Experimental data (symbols) are from Ref.[4]. Data for water (curve-c) are shifted to right by 1 km/s for clarity.

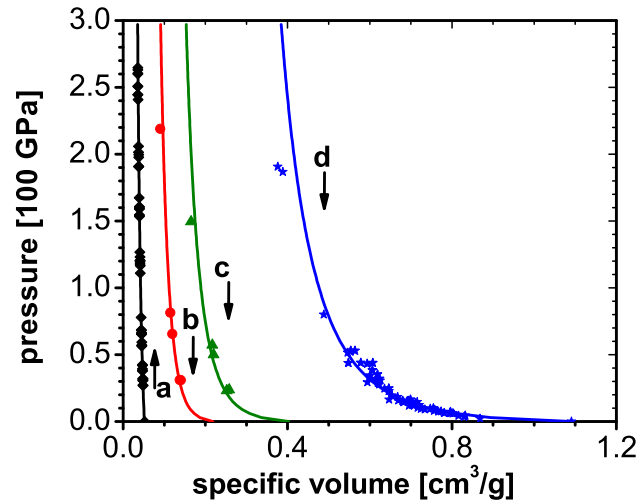


Figure 3.13: Pressure-volume Hugoniot of W (curve-a), paraffin-W mixture with $w_1/w_2=16/84$ (curve-b), $w_1/w_2=34/66$ (curve-c) and Paraffin (curve-d). Experimental data (symbols) are from Ref.[4].

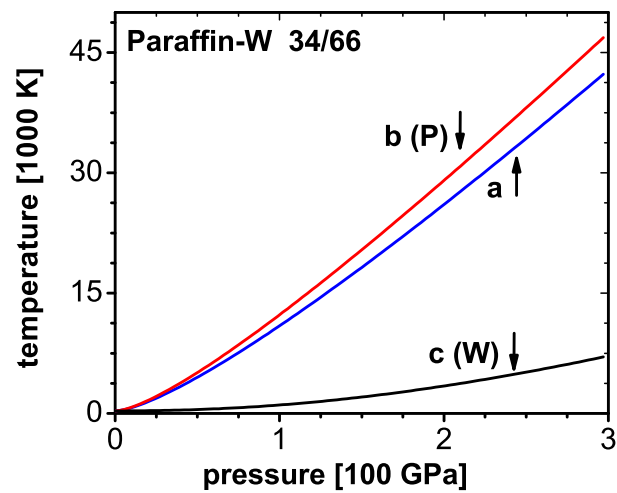


Figure 3.14: Temperature-pressure curves for paraffin-W mixture with $w_1/w_2=34/66$. Average temperature (curve-a), temperature of paraffin (curve-b), temperature of W (curve-c).

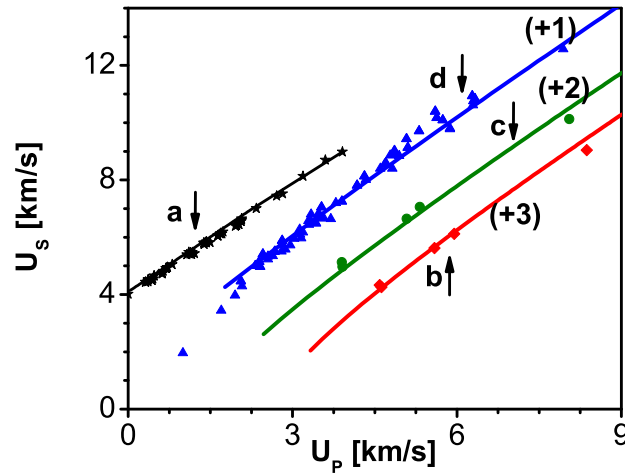


Figure 3.15: Shock speed (U_s) vs. particle speed (U_p) for W (curve-a), paraffin-W mixture with $w_1/w_2=16/84$ (curve-b), $w_1/w_2=34/66$ (curve-c) and paraffin (curve-d). Experimental data (symbols) are from Ref.[4]. Data for paraffin (curve-d), mixture (curve-c) and mixture (curve-b) are shifted to right by 1, 2, and 3 km/s for clarity.

3.4.4 Porous mixture

Our last example is of a porous mixture of dense tantalum carbide ($\rho_0 \approx 14.2 \text{ g/cm}^3$) and graphite ($\rho_0 \approx 2.24 \text{ g/cm}^3$) with porosity $\alpha_0 = 1.44$. Excellent agreement is found in Fig. 3.16 for both of the components, while some differences are noted for the mixture. Nevertheless, the effect of porosity is properly accounted within our method. Temperatures are shown in Fig. 3.17. These curves are similar to that in the first layer for W-Cu ($w_1/w_2 = 25/75$) in Fig. 3.5. TaC has a temperature lower than that of C because of its lower compressibility, in spite of it having lower specific heat. However, the average mixture temperature is high due to porosity effects and consequent large volume change. Results for shock speed vs. particle speed, shown in Fig. 3.18, follow experimental data quite well except for TaC in the low speed range, which is due to a phase change. This can be remedied by employing different sets of parameters in the two phases.

The present approach does not include any effect of air or other gases which might be present in the pores because their weight fractions are completely negligible.

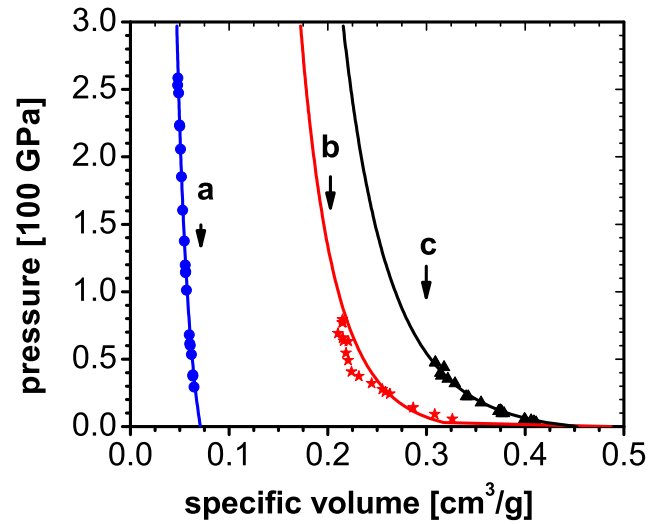


Figure 3.16: Pressure-volume Hugoniot of TaC (curve-a), TaC-C mixture with $w_1/w_2=30/70$ and porosity 1.44 (curve-b), and carbon (curve-c). Experimental data (symbols) are from Ref.[5].

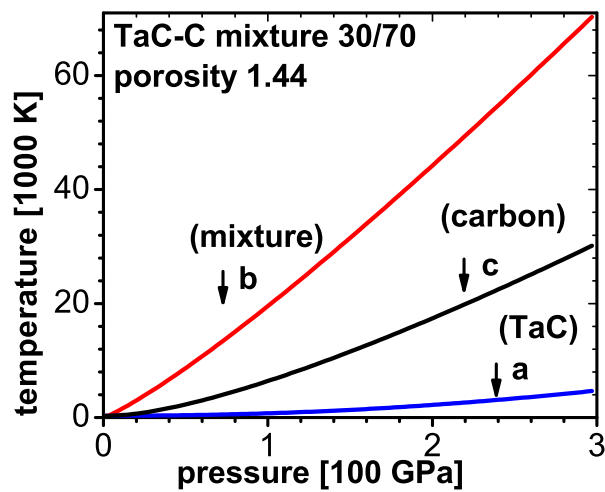


Figure 3.17: Temperature-pressure curves for TaC-C mixture with $w_1/w_2=30/70$ and porosity 1.44. Temperature of TaC (curve-a), average temperature (curve-b), and temperature of carbon (curve-c).

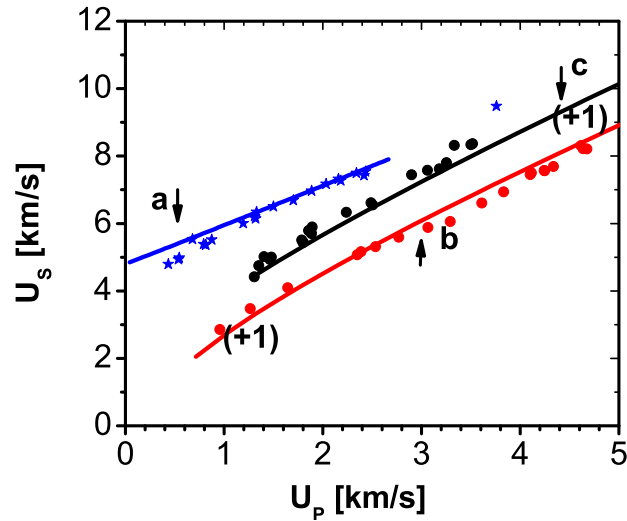


Figure 3.18: Shock speed (U_s) vs. particle speed (U_p) for TaC (curve-a), TaC-C mixture with $w_1/w_2=30/70$ and porosity 1.44 (curve-b), and carbon (curve-c). Experimental data (symbols) are from Ref.[5]. Data for mixture (curve-b) and carbon (curves-c) are shifted to right by 1 km/s, respectively, for clarity.

3.5 Summary

In this chapter we outlined a method to compute the Hugoniot of binary mixtures, including non-equilibrium thermal effects. This development employs the enthalpy-based EOS, which is well suited to the mixture problem because pressure equilibration is fast, and hence pressure and temperature are appropriate independent variables. The main assumption involved in our approach is the weak temperature dependence of the enthalpy parameters, which we have shown to have sufficient validity even in the high pressure range. The EOS of the mixture is found to have a distinct contribution from enthalpy differences of the components, after introducing proper averaging of the zero temperature isotherm and enthalpy parameters. We have noted, theoretically as well as numerically, that this extra term makes only a small contribution to the P-V Hugoniot of the mixture. We have proposed the use of a single component criteria for determining non-equilibrium component temperatures, and estimating the contribution of the enthalpy difference term in P-V Hugoniot. The component temperatures are compared with the average mixture temperature, thereby providing an estimate of non-thermal equilibrium conditions. The method is applied to five cases, including a porous mixture. A simple zero

temperature isotherm and a linear thermal energy model are shown to provide accurate results in the pressure range up to ~ 300 GPa. Overall agreement of our approach with experimental data is quite good. Furthermore, we have unified all the mixture theories within our approach and brought out the different assumptions on equilibrium conditions. The method can be generalized to multi-component mixtures. Effects of shock-induced chemical reactions or detonation can also be included as component temperatures and mixture temperatures are known explicitly.

Generalized enthalpy-based equation of state for multi-component mixtures

4.1 Introduction

Shock wave propagation in composites made of a low density binder and materials of high strengths and stiffness is a topic of current interest due to several applications [98]. Epoxy based composites having varying amounts of polycrystalline alumina (Al_2O_3) have been investigated recently [99–101]. Measurements of Hugoniot of three component composites consisting of aluminum, iron oxide (Fe_2O_3) and epoxy and aluminum, pyrolusite (MnO_2) and epoxy have also been reported [98, 102, 103]. Multicomponent mixture models are also needed in modeling equation of state (EOS) of graded density impactors [104]. Material synthesis employing shock induced reactions, initiation of heterogeneous energetic materials, applications involving attenuation of blast waves, etc., have led to important research in shock wave propagation in multicomponent mixtures [63]. Treatment of porosity effects in mixtures introduces additional problems in thermodynamic modeling, as in the case of single component materials [23, 58].

Time scales for equilibration of thermodynamic variables during shock transit is determined by the particulate nature of components [86]. Pressure differences smooth out in typical time $\tau_1 \sim 5d/C_s$, where d is some average particle diameter and C_s sound speed. If $C_s \sim 5000$ m/s, then τ_1 is about 1 ns for 1 μm particle [87]. So pressure equilibration occurs during shock transit as τ_1 is about shock rise time even for 100 μm size particles. Shock compaction experiments do not show different particle speeds in components [88]. However, there is differential micro kinetic energy production in components due to inter-facial friction [89]. Further, unequal thermal energies occur in compo-

nents immediately behind the shock due to different compressibility. Thermal energy or temperature smoothing occurs on time $\tau_2 \sim d^2/D$, where D is thermal diffusivity. Even for good conductors ($D \sim 100 \text{ mm}^2/\text{s}$ for Al), τ_2 is three orders larger than τ_1 for $100 \text{ }\mu\text{m}$ particle. So non-equilibrium temperatures could arise after shock passage when particles sizes are $\gtrsim 50 \text{ }\mu\text{m}$. In mixtures with much smaller size particles, thermal equilibrium could be assumed.

As mentioned in chapter 3 the earliest approaches to deal with shock compression of mixtures made use of the Hugoniot of components. Hugoniot volumes of components are determined for a given pressure, and then mixture volume is obtained by averaging with component weight fractions [90, 91]. This approach is termed as *additivity rule* or *additivity principle* [63, 92]. In the scheme called kinetic energy averaging, first the kinetic energy of the mixture is obtained by averaging component kinetic energies deduced from the component Hugoniot for a specified pressure, and then all other parameters are computed via conservation equations [94]. Both these schemes do not assume equilibration of either material velocity or thermal energy in the mixture on shock traversal. McQueen *et al*, employ weighted average of zero temperature isotherms and Gruneisen parameters for a given pressure, and then uses the Mie-Gruneisen EOS to obtain mixture Hugoniot [93]. Zhang *et al* simply uses the average zero temperature isotherm and thereafter follows the procedure for single materials employing enthalpy-based EOS [76, 96]. Originally proposed by Rice and Walsh [67], enthalpy-based EOS is well suited for also treating porosity effects in single component materials [6, 66, 68]. In these two schemes, velocity equilibration is implied as they use Hugoniot equation involving mixture volume, however, they do not address thermal equilibration effects. There are also schemes, which assume pressure and velocity equilibration, to obtain the parameters of the (assumed) linear shock speed vs. particle speed relation [98, 104]. Starting with an average Gibbs's free energy, Duvall and Taylor developed an equilibrium mixture theory, and so obtained only equilibrium temperature [87]. This scheme naturally leads to C_V (constant volume specific heat) weighted Gruneisen parameter for the mixture. A scheme employing the Mie-Gruneisen EOS is developed by Krueger and Vreeland to investigate non-thermal equilibrium effects in mixtures [88]. They showed that Rankine-Hugoniot conservations laws, which automatically assume velocity

equilibration, have to be supplemented with an additional equation specifying partitioning of energy between the components, though the P-V Hugoniot is quite insensitive to this partitioning.

The methods summarized above have been reviewed and discussed recently together with comparison of numerical results [95, 104]. The additivity rule is known to provide reasonable accuracy when applied to a large database of mixture data [63, 92]. The scheme based on kinetic energy averaging is found to be accurate, however, simpler compared to that involving average Mie-Gruneisen parameter [95]. Averaging the parameters in the (assumed) linear shock speed vs. particle speed relation also provides a simple scheme if the components obey linear relations [98, 104]. Notwithstanding these developments, it is desirable to have a general approach which can also provide information on non-equilibrium thermal energy distribution in the components.

This chapter describes the development of the enthalpy-based EOS for multi-component mixtures, which includes non-equilibrium effects. Just like McQueen *et al*, we make use of average zero temperature isotherm and mixture parameters [93]. However, enthalpy-based approach is better suited for mixtures as pressure equilibration is fast and so pressure could be treated as independent variable. Shock Hugoniot of porous substances are also obtained appropriately within this scheme. An added feature of this method is occurrence of a term involving enthalpy differences in mixture EOS, equivalent of which is not obtained by McQueen *et al*. We propose to use additivity principle for determining energy partitioning on to the components. Though the magnitude of enthalpy differences is found to be small, our method provides a way to estimate non-equilibrium effects by comparing component temperatures with average temperature. We apply the scheme to epoxy based two as well as three component mixtures, and show excellent agreement with experimental data. Numerical results are obtained using a linear thermal model and zero temperature isotherm of Vinet *et al* [36, 37], which is known to provide good accuracy [41].

The chapter is organized as follows. Generalized enthalpy-based EOS for multi-component mixtures is discussed in section 4.2. Section 4.3 describes multi-

component mixture Hugoniot employing single component criteria. In section 4.4 EOS models used in computation are given. Results are shown in section 4.5. Section 4.6 summarizes the present work.

4.2 Generalized enthalpy-based equation of state for multi-component mixtures

The enthalpy-based EOS is analogous to the Mie-Gruneisen EOS, however, the dependent variable volume is expressed in terms of enthalpy which depends on pressure and temperature. The parameters that enter into this approach are the enthalpy parameter χ and constant pressure specific heat C_P . This formalism has been successfully employed for describing the EOS of water [67], Hugoniot of porous materials [66, 68], also including explicit treatment of electronic effects [6]. The EOS parameters, χ and C_P , can be split into those of the components, and also of unbound electrons for developing a generalized approach.

As discussed earlier, pressure, particle speed and shock speed are quite uniform within the mixture. But, non-equilibrium thermal energies lead to different temperatures in the components. Then, integrating the defining relations, viz., $(\partial V/\partial T)_P = (\chi/P)C_P$ and $(\partial H/\partial T)_P = C_P$, the specific volume V_k and enthalpy H_k of component k can be expressed as [6]

$$V_k = V_{ck}(P) + \frac{1}{P} \int_0^{T_k} (\chi_{ik} C_{Pik} + \chi_e C_{Pe_k}) d\tau \quad (4.1)$$

$$H_k = H_{ck}(P) + \int_0^{T_k} (C_{Pik} + C_{Pe_k}) d\tau. \quad (4.2)$$

The reference state quantities, V_{ck} and $H_{ck} = E_{ck} + PV_{ck}$, denote, respectively, the zero temperature specific volume and specific enthalpy of component k at pressure P . The equation, $P_{ck}(V_{ck}) = P$, where $P_{ck}(V)$ is zero temperature isotherm, is to be solved to obtain V_{ck} . Ionic enthalpy parameter χ_{ik} and specific heat C_{Pik} and their electronic counterparts χ_e and C_{Pe_k} are additional parameters in above equations.

The electron Gruneisen parameter Γ_e is in the range 0.6 – 0.8 [57], and so $\chi_e = \Gamma_e / (1 + \Gamma_e)$ is a constant. It is generally assumed that χ_{ik} in the solid phase is nearly independent of temperature. This assumption can be tested by comparing χ_{ik} on the solid Hugoniot and the zero temperature isotherm [75]. Such a comparison for aluminum is shown in Fig. 4.1A. The results given here were obtained using well known formulations for zero temperature isotherm and electronic thermal energy [6]. However, we have employed a more accurate ionic thermal model [47] in comparison to Cowan's model used earlier [6]. Maximum difference of about 11 % occurs near 150 GPa where temperature on the Hugoniot is nearly 5200 K. Further, as χ_{ik} occurs as the ratio $\chi_{ik} / (2 - \chi_{ik})$ in the P-V Hugoniot (see Eq. (4.9) below), maximum effect of this difference is only about 6 %. Therefore we replace χ_{ik} with their respective values at T_k within the integral in Eq. (4.1). Then, the generalized enthalpy-based EOS follows by combining Eqs. (4.1) and (4.2):

$$V_k = V_{ck}(P) + \frac{\chi_{ik}}{P} H_{tik}(P, T_k) + \frac{\chi_e}{P} H_{tek}(P, T_k), \quad 1 \leq k \leq N. \quad (4.3)$$

where H_{tik} and H_{tek} , respectively, denote the specific ion thermal enthalpy and electron enthalpy of component k . Thermal electron contribution to total volume is accounted explicitly here.

An EOS of the mixture is readily obtained by multiplying Eq. (4.3) with the weight fraction w_k of the component k , and summing over all k :

$$V = \bar{V}_c + \frac{1}{P} \sum_{k=1}^N \chi_{ik} w_k H_{tik} + \frac{\chi_e}{P} \bar{H}_{te} \quad (4.4)$$

Here, $\bar{V}_c = \sum_1^N w_k V_{ck}$ and $\bar{H}_{te} = \sum_1^N w_k H_{tek}$, respectively, denote zero temperature specific volume and specific electron enthalpy of the mixture. The thermal enthalpy of component m is expressed as

$$w_m H_{tim} = H - \bar{H}_c - \bar{H}_{te} - \sum_{k \neq m}^N w_k H_{tik}, \quad 1 \leq m \leq N \quad (4.5)$$

where H is the total specific enthalpy and $\bar{H}_c = \sum_1^N w_k H_{ck}$ is the zero tempera-

ture specific enthalpy of the mixture. The result of combining Eqs. (4.4) and (4.5) is:

$$V = \bar{V}_c + \frac{\chi_{im}}{P}(H - \bar{H}_c) + \frac{1}{P}(\chi_e - \chi_{im})\bar{H}_{te} + \frac{1}{P} \sum_{k \neq m}^N (\chi_{ik} - \chi_{im})w_k H_{tik}, \quad 1 \leq m \leq N \quad (4.6)$$

To remove the explicit dependence of Eq. (4.6) on component m , we multiply it with normalized weight factors $f_m = w_m C_{Pim} / \bar{C}_P$, where $\bar{C}_P = \sum_{k=1}^N w_k C_{Pik}$ is the ionic specific heat of the mixture, and sum over all m to obtain:

$$V = \bar{V}_c + \frac{\bar{\chi}_i}{P}(H - \bar{H}_c) + \frac{1}{P}(\chi_e - \bar{\chi}_i)\bar{H}_{te} + \frac{1}{P} \sum_{k,m,k < m}^N (\chi_{ik} - \chi_{im})(f_m w_k H_{tik} - f_k w_m H_{tim}) \quad (4.7)$$

Here we have defined the average ionic enthalpy parameter $\bar{\chi}_i = \sum_{k=1}^N f_k \chi_{ik}$. It follows from definition that this is the correct weighting of enthalpy parameter. Without the last term, Eq.(4.7) exactly resembles that of a single material [6]. This term, which involves differences of enthalpy parameters as well as ion thermal enthalpies, is expected to be a small correction to the preceding three terms because, in addition, the product $w_m w_k$, has maximum value 1/4. Finally, we note that this term vanishes identically if all components are at same temperature and C_{Pik} are constants.

4.3 Multi-component mixture Hugoniot

Total enthalpy along the Hugoniot of the material is given by:

$$H = E_{00} + \frac{1}{2}P_{00}(V_{00} - V) + \frac{1}{2}P(V_{00} + V) \quad (4.8)$$

where E_{00} and P_{00} are, respectively, the energy and pressure at initial volume V_{00} . The P-V Hugoniot is then obtained by substituting Eq. (4.8) in (4.7):

$$\begin{aligned} V = & 2\bar{V}_c \frac{1 - \bar{\chi}_i}{2 - \bar{\chi}_i^*} + \frac{2}{P} \frac{\chi_e - \bar{\chi}_i}{2 - \bar{\chi}_i^*} \bar{H}_{te} + \frac{\bar{\chi}_i}{2 - \bar{\chi}_i^*} \left(V_{00}(1 + P_{00}/P) + \frac{2}{P}(E_{00} - \bar{E}_c) \right) \\ & + \frac{1}{P} \sum_{k,m,k < m}^N \frac{\chi_{ik} - \chi_{im}}{2 - \bar{\chi}_i^*} \frac{w_k w_m}{\bar{C}_P} (C_{Pim} H_{tik} - C_{Pik} H_{tim}) \end{aligned} \quad (4.9)$$

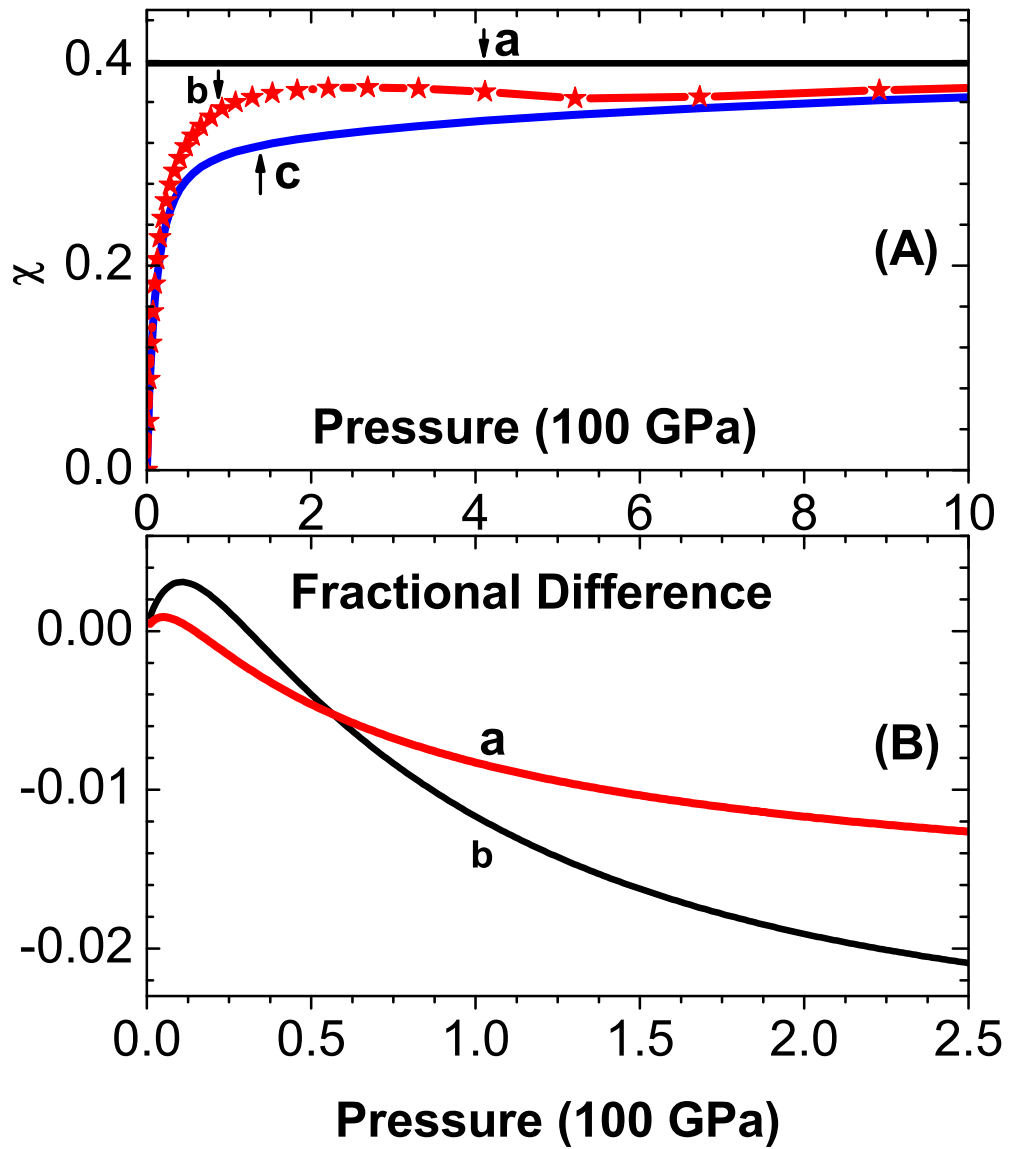


Figure 4.1: (A). Variation of χ with P for Al. (a) $\chi_e = \Gamma_e / (\Gamma_e + 1)$ with $\Gamma_e = 0.66$. (b) χ_i obtained from 3-component model [6]. (c) $\chi_i = P \Gamma_s / B_s$, where Γ_s is Gruneisen parameter of solid [7] and B_s bulk modulus, along zero temperature isotherm [6]. (B). Ratio of enthalpy difference term to those preceding it in Eq. (4.9) for two mixtures. (a.) Al-MnO₂-Epoxy, (b.) Al-Fe₂O₃-Epoxy.

where $\bar{\chi}_i^* = \bar{\chi}_i(1 - P_{00}/P)$, and $\bar{E}_c = \bar{H}_c - P\bar{V}_c$. On neglecting last term, for reasons pointed above, we get a P-V Hugoniot exactly similar to that of a single material [6]. This fact provides a theoretical justification for use of just the average parameters in mixture theory. We show its magnitude relative to the preceding terms in Fig. 4.1B for Al-Fe₂O₃-Epoxy and Al-MnO₂-Epoxy mixtures. Over a pressure range of ~ 200 GPa, the maximum contribution of this term $\lesssim 2\%$ of the preceding terms. More results for these mixtures and details of numerical calculations are discussed below. Thus, quite accurate results are obtained with the first three terms in Eq. (4.9). However, we shall discuss a scheme to compute temperatures in different components as well as equilibrium temperature in the mixture.

The parameter defined as $\alpha_0 = V_{00}/V_0$, where V_{00} is the volume including that of pores, is used to characterize porous mixtures. For application to these materials, the zero temperature volumes V_{ck} ($1 \leq k \leq N$) of all components are extended to the region $V_{0k} \leq V_{ck} \leq \alpha_0 V_{0k}$ using the P- α model, where V_{0k} is the initial volume of solid component k [6, 12].

4.3.1 Single component criteria

In case one is intending to use the averaging methods discussed in the introduction, it is necessary to invoke what is called the *additivity rule* or *single component criteria*. This is simply Eq. (4.8), or its equivalent form in energy, applied to each component [90, 91, 94]:

$$H_k = E_{00k} + \frac{1}{2}P_{00}(V_{00k} - V_k) + \frac{1}{2}P(V_{00k} + V_k), \quad 1 \leq k \leq N \quad (4.10)$$

Here E_{00k} ($1 \leq k \leq N$) is the energy of component k at its initial volume V_{00k} and V_k is the volume after shocking to pressure P . Trunin and co-workers have compared the Hugoniot of a large number of mixtures within the *additivity rule* [63]. Saurel *et al* developed a theoretical justification of this rule for low shock pressures and applied it to twelve mixtures [92]. We note that the use of Eq.(4.10) and the *additivity rule* imply neither velocity nor thermal equilibration in the mixture. However, a concept invoking generation of micro kinetic energy in the components leading to non-equilibrium energy distribution has

been developed using an *extended single component criteria* [89].

The *single component criteria*, together with enthalpy-based EOS in Eq. (4.3), leads to Hugoniot of components:

$$V_k = 2V_{ck} \frac{1 - \chi_{ik}}{2 - \chi_{ik}^*} + \frac{2}{P} \frac{\chi_e - \chi_{ik}}{2 - \chi_{ik}^*} H_{tek} + \frac{\chi_{ik}}{2 - \chi_{ik}^*} \left(V_{00k} (1 + P_{00}/P) + \frac{2}{P} (E_{00k} - E_{ck}) \right) \quad (4.11)$$

where $1 \leq k \leq N$. Note that Eq. (4.10) implies (4.8), though the converse is not necessarily true. However, summing Eq. (4.11) over k , with weight factors f_k , does not yield Eq. (4.9). Thus, our approach is basically different from that involving simply averaging the component Hugoniot, though the latter may provide adequate accuracy for some applications [95]. Using Eq. (4.11), kinetic energies of the components and the mixture can be readily computed for use in kinetic energy averaging method [94].

4.3.2 Determination of temperature in mixture

If all components in the mixture are in thermal equilibrium, then the equilibrium temperature $T = T_k$, $1 \leq k \leq N$, is determined from the equation:

$$\frac{d}{dP} T - \frac{\bar{\chi}}{P} T = \frac{0.5}{\bar{C}_P} \left((V_{00} - V) + (P - P_{00}) dV/dP \right) \quad (4.12)$$

which is similar to the Walsh-Christian differential equation, though there volume is independent variable [81]. Here, $\bar{\chi} = \sum_{k=1}^N w_k C_{Pk} \chi_k / \bar{C}_P$ is the average enthalpy parameter of the mixture and $\bar{C}_P = \sum_{k=1}^N w_k C_{Pk}$ is its specific heat. Here, χ_k and C_{Pk} contain electronic contributions also [6]. However, in the non-equilibrium case, which is prevalent in most situations, the component temperatures, T_k , $1 \leq k \leq N$, need to be obtained separately. The total compressive enthalpy (in the bracketed terms in Eq. (4.12)) is shared by the components. The fractional sharing is unknown, and so need to be specified a priori in some arbitrary manner [88]. But it is clear from earlier discussion that non-equilibrium temperatures arise because the components get compressed almost independently and time available for heat diffusion is insufficient before shock traversal. So, *we propose to use the single component criteria to determine*

these temperatures. Then Eq. (4.12) is replaced by the set of equations:

$$\frac{d}{dP}T_k - \frac{\chi_k}{P}T_k = \frac{0.5}{C_{P_k}} \left((V_{00k} - V_k) + (P - P_{00})dV_k/dP \right), \quad 1 \leq k \leq N \quad (4.13)$$

These temperatures are then used to evaluate the last term in Eq.(4.9) in the non-equilibrium case.

4.3.3 Numerical technique

A numerical method for solving differential equations in Eqs. (4.13), using forward differencing, is obtained as:

$$\begin{aligned} C_{P_{k,n}}(1 - \chi_{k,n}\Delta P/P_n) T_{k,n} &= C_{P_{k,n}}T_{k,n-1} + 0.5 \left((V_{00k} - V_{k,n})\Delta P \right. \\ &\quad \left. + (P_n - P_{00})(V_{k,n} - V_{k,n-1}) \right) \end{aligned} \quad (4.14)$$

Here the subscript n on different variables denotes their respective values at $P_n = P_{00} + n\Delta P$ where ΔP is an increment in pressure, and $n=1, 2, 3$ etc. Eq. (4.14) have to be evaluated at each P_n . An iteration method is needed at each P_n if electronic terms are treated explicitly because H_{te} depends on $T_{k,n}$ [6]. An identical method can be used to solve for T from Eq. (4.12) to obtain equilibrium temperature.

4.4 EOS models

Mixture volume for multi-component systems, given in Eq. (4.9), accounting non-equilibrium temperatures, is the main result of this work. Models for zero temperature isotherm, enthalpy parameters and constant pressure specific heats for each component are needed for its application. We shall apply the present formulation to compute the Hugoniot of epoxy based two and three component mixtures. Experimental data on these systems are generally available for low pressure regimes $\lesssim 30$ GPa [4, 5]. Therefore we only use effective χ_k and C_{P_k} since explicit accounting of thermal electron effects is unnecessary in this region. So we do not include the second term in Eq. (4.9).

For the zero temperature isotherm of each component, we use the formulation

due to Vinet *et al* [36, 37]:

$$\begin{aligned}
 P_c &= 3B_0X^{-2}(1-X)\exp(\eta(1-X)) \\
 E_c &= -E_b + (9/\eta^2)B_0V_0(1-Z\exp(\eta(1-X))) \\
 B_s &= B_0X^{-2}(1+(\eta X+1)(1-X))\exp(\eta(1-X))
 \end{aligned}
 \tag{4.15}$$

where $X=(V/V_0)^{1/3}$, $Z=1-\eta(1-X)$ and $\eta=(3/2)(B'_0-1)$. Further, B_0 , B'_0 and E_b are, respectively, the bulk modulus, its pressure derivative and cohesive energy at V_0 and $P=0$. Detailed analysis of this EOS shows that it is quite accurate up to ~ 1 TPa [41].

Eq. (4.15) is numerically inverted to get $V_c(P)$ for a given pressure P . This is easily effected using an iteration method (starting with $Y=1$) after rewriting it as

$$Y = \left(Y^{1/3} + \frac{P}{3B_0} \exp[-\eta(1-Y^{-1/3})] \right)^{3/2}
 \tag{4.16}$$

where $Y=V_0/V$. Then, the definition of enthalpy parameter yields $\chi=P\Gamma(V_c)/B_s(V_c)$. For Gruneisen parameter of each component we use the expression $\Gamma=\Gamma_0(V/V_0) + (2/3)(1-V/V_0)^2$ where Γ_0 is its value at V_0 [7, 97]. Component index k is omitted from these equations for simplicity of notation.

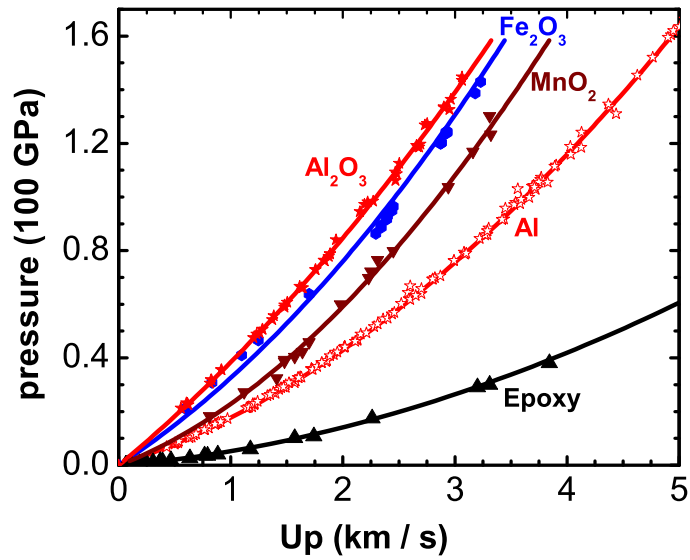
For thermal component of enthalpy, we assume that C_V is a constant, and the standard expressions $E_t=C_V(T-T_0)$ and $P_t=(\Gamma/V)E_t$ [37, 41]. Constant pressure specific heat C_P is then readily computed using the expression $C_P=C_V(1+T\Gamma\alpha_P)$, where α_P is volume expansion coefficient. This formulation is now applied to five components, and five mixture compositions. The Al-Fe₂O₃-epoxy mixture has slightly porosity, i.e. ~ 15 %. Material parameters for the components used in calculations are given in Table 4.1. More detailed thermal models, including melting and electronic effects, can be readily employed if necessary [6].

4.5 Results

First of all we apply the models outlined above, together with the data given in Table 4.1, to five materials which form the components of two and three com-

Table 4.1: EOS parameters of components. ρ_0 [g/cm³], B_0 [100 GPa] and C_V [J/g K]

Material	ρ_0	B_0	B'_0	Γ_0	C_V
Al	2.71	0.728	4.36	2.1	0.901
Al ₂ O ₃	3.97	2.63	3.90	1.37	0.875
Fe ₂ O ₃	5.01	1.40	3.10	1.99	0.653
MnO ₂	4.42	0.76	4.50	1.2	0.623
Epoxy	1.20	0.094	4.76	1.43	1.01

**Figure 4.2:** Comparison of $P-U_p$ Hugoniot of single component materials, Epoxy, Al, MnO₂, Fe₂O₃, and Al₂O₃. Experimental data are from references [4, 5].

ponent epoxy based mixtures. Pressure on the Hugoniot vs. particle speed for Al, Al_2O_3 , Fe_2O_3 , MnO_2 and epoxy are shown in Fig. 4.2. This comparison with experimental data [4, 5] shows the adequacy of the models even up to pressures ~ 160 GPa. There is slight disagreement with data for Fe_2O_3 in the pressure range below ~ 60 GPa, which is due to the structural phase change. Different model parameters need to be used in the two phases for improving comparison with data. However, this mismatch is unimportant for the case of mixtures, and so is not considered any further.

We compare pressure vs. particle speed for two component mixtures consisting of Al_2O_3 and epoxy in Fig. 4.3A. Results for three compositions, where Al_2O_3 weight fractions are $w_1=0.454$, 0.626 and 0.708, are shown. The gradual increase of pressure, for the same particle speed, as Al_2O_3 weight fraction increases is predicted quite accurately by the mixture model. Fig. 4.3B shows non-equilibrium temperatures vs. pressure in Al_2O_3 and epoxy for the composition $w_1/w_2 = 0.454/0.546$. While temperature of epoxy steadily increases with pressure, Al_2O_3 temperature remains almost constant. This is due to the larger compressibility of epoxy in comparison to that of Al_2O_3 . Equilibrium temperatures of the mixture, though lie in between the limits, is quite different from those of the components.

We now consider a three component mixture of Al- MnO_2 -epoxy with weight fractions $w_1/w_2/w_3=0.251/0.537/0.212$. Comparison of pressure vs. particle speed results with experimental data shown in Fig. 4.4A shows good agreement. However, there is slight mismatch at intermediate pressures around 15 GPa. This is reflected in the comparison of particle speed vs. shock speed results in Fig. 4.5A. Temperature vs. pressure for the components and mixture in equilibrium are given in Fig. 4.6A. Al and MnO_2 have almost same temperatures as their properties also are similar. Just the opposite is the case for epoxy, its lower bulk modulus overrides the larger specific heat to develop much higher temperatures. Average mixture temperature is well below that of epoxy.

Our final case is a three component mixture of Al- Fe_2O_3 -epoxy with weight fractions $w_1/w_2/w_3=0.126/0.374/0.5$. Pressure vs. particle speed results shown

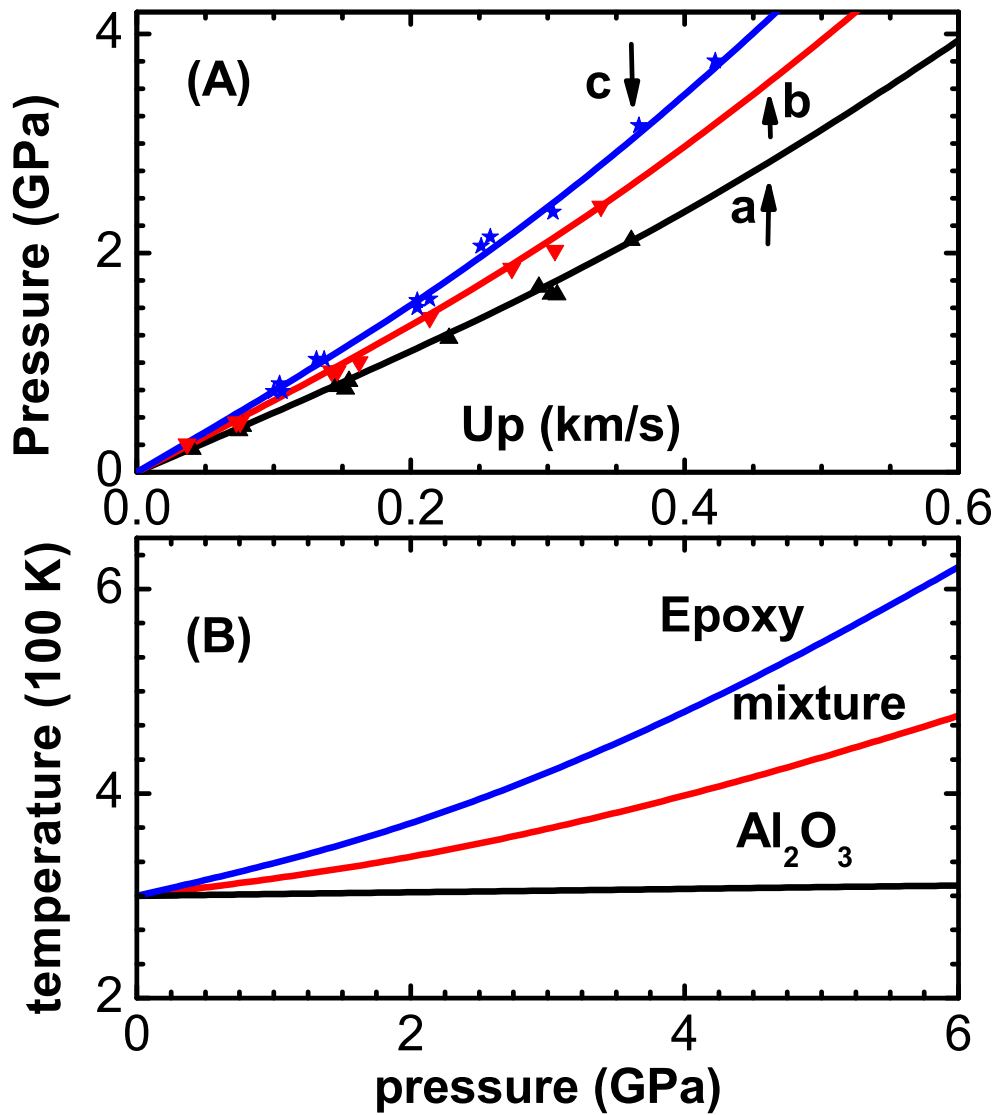


Figure 4.3: (A). Comparison of $P-U_p$ Hugoniot of two component mixtures of Alumina and Epoxy. (a) Al_2O_3 (0.454)-Epoxy, (b) Al_2O_3 (0.626)-Epoxy, (c) Al_2O_3 (0.708)-Epoxy. Experimental data are from references [4, 5]. (B). Temperature vs. pressure on the Hugoniot of two component mixture of Al_2O_3 and Epoxy with $w_1/w_2=0.454/0.546$. Graphs show component temperatures and average mixture temperature

in Fig. 4.4B show good agreement with experimental data. Similar agreement is also evident in the shock speed vs. particle speed comparison shown in Fig. 4.5B. Our approach provides much better agreement in comparison to that given by Zhang *et al* [76], which simply uses average zero-temperature isotherm and thereafter follows the single component theory. Temperature vs. pressure in different components and equilibrium mixture are shown in Fig. 4.6B. Slightly larger temperatures in Fe_2O_3 , in comparison to that in Al, is due to its lower specific heat, though it has a larger bulk modulus (see Table 4.1). As in the case of Al- MnO_2 -epoxy system, due to its lower bulk modulus, epoxy overrides its larger specific heat to develop much higher temperatures. Average mixture temperatures lie in between those of the components.

4.6 Summary

In this chapter we have developed a method to compute the Hugoniot of multi-component mixtures using enthalpy-based EOS. The possibility of incorporating non-equilibrium thermal effects is included in this model. Thermal electron effects are also accounted explicitly in the method. Choice of pressure and temperature as independent variables, leading to enthalpy-based EOS, is better suited for mixtures since equilibration of pressure is much faster compared to thermal energy. We pointed out in the introduction the problems encountered in mixture theories using total volume as independent variable.

For the systems we have analyzed, the assumption of weak temperature dependence of the enthalpy parameters is very well justified in the pressure range of available experimental data. For higher range of pressures, these component parameters are easily computed on suitable P-V curves like the solid Hugoniot. Our formulation shows that there is a specific contribution to the EOS due to enthalpy differences of the components. However, it is shown that this contribution is somewhat small to the P-V Hugoniot of the mixtures analyzed. Even so, it is necessary to have a complete theory, as attempted in this paper, which can be used to evaluate the contributions of all effects separately.

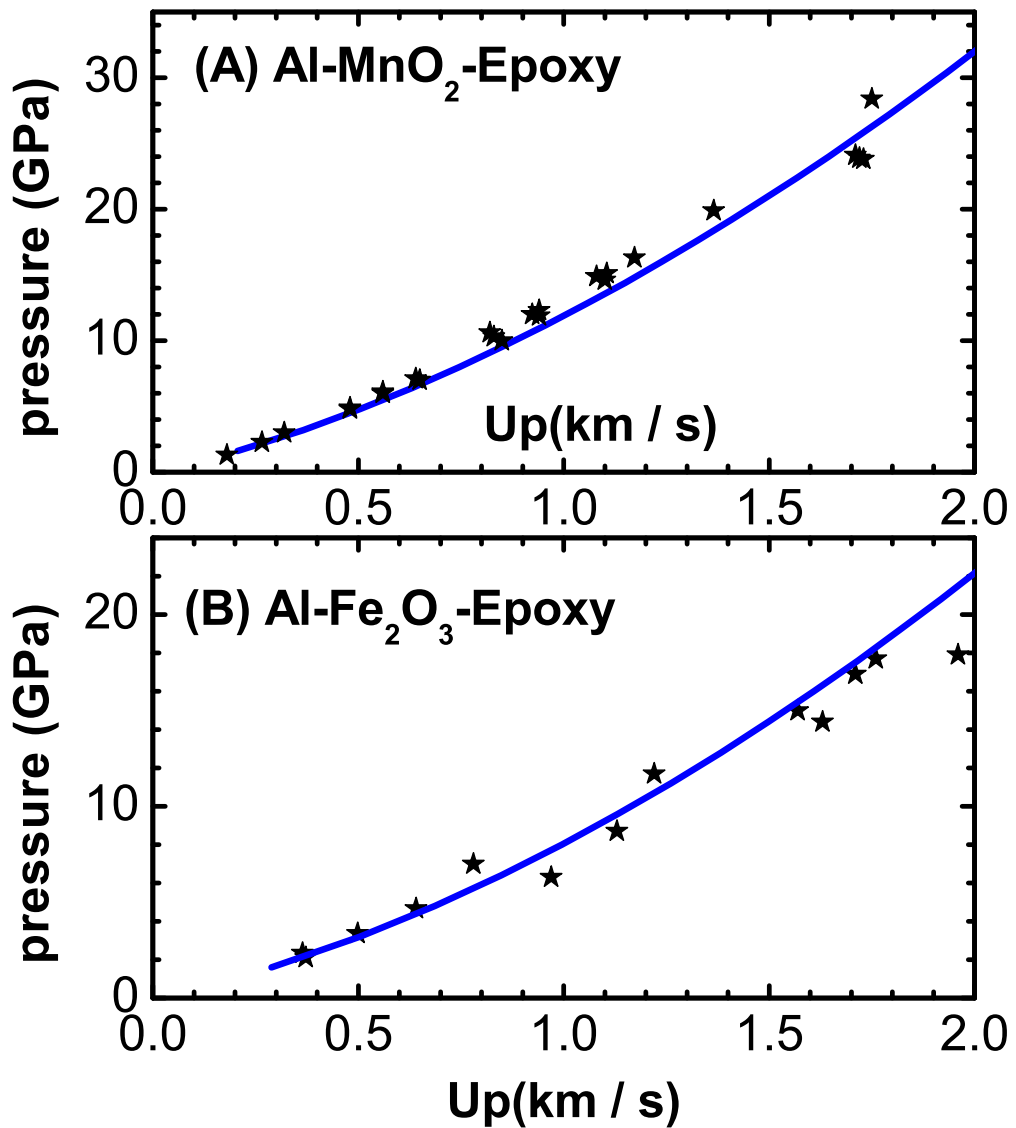


Figure 4.4: (A). Comparison of $P-U_p$ Hugoniot of three component mixture of Al, MnO₂ and Epoxy with $w_1/w_2/w_3=0.251/0.537/0.212$. Experimental data are from references [4, 5] (B). Comparison of $P-U_p$ Hugoniot of three component mixture of Al, Fe₂O₃ and Epoxy with $w_1/w_2/w_3=0.126/0.374/0.5$. Experimental data are from references [4, 5].

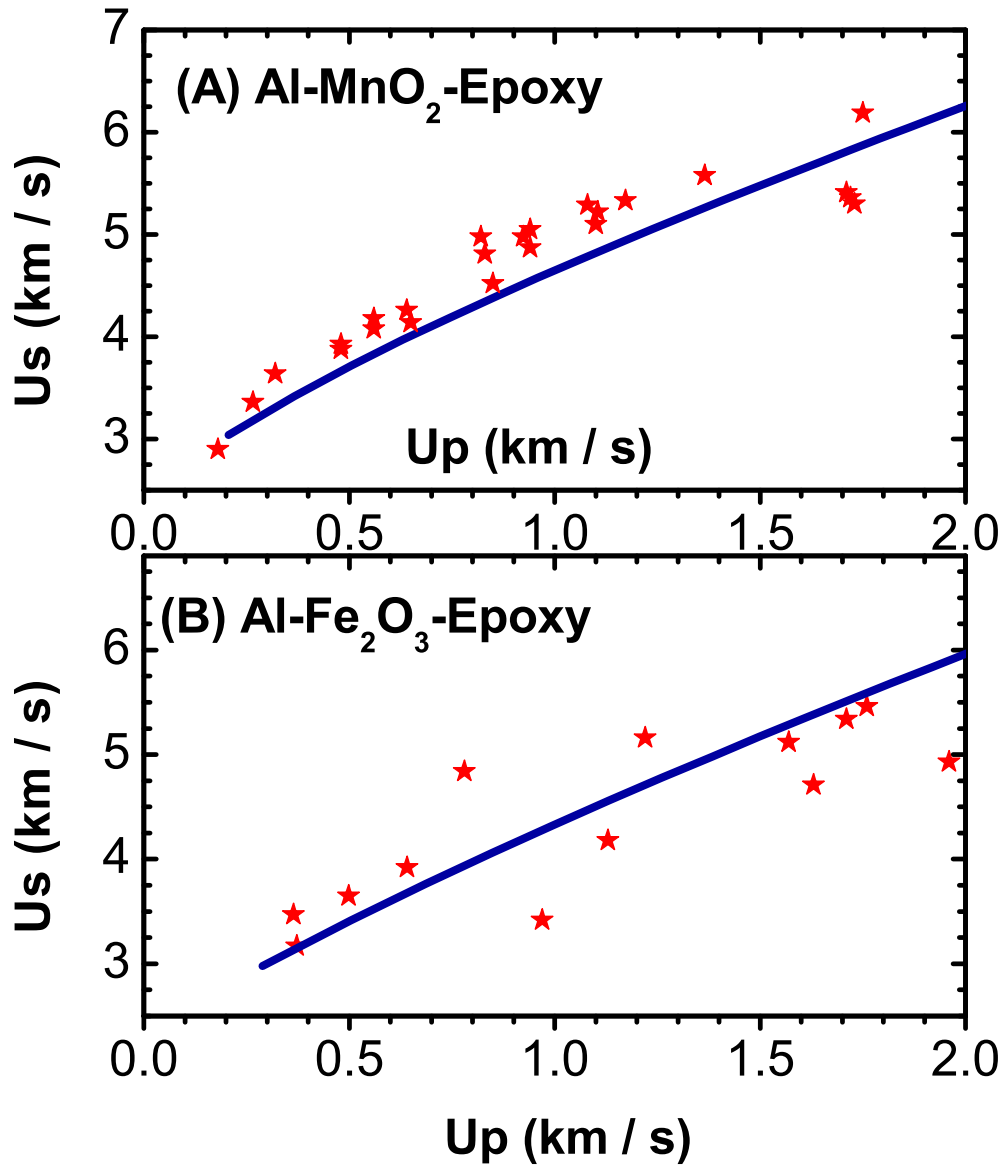


Figure 4.5: (A). Comparison of U_p - U_s curve of three component mixture of Al, MnO₂ and Epoxy with $w_1/w_2/w_3=0.251/0.537/0.212$. Experimental data are from references [4, 5] (B). Comparison of U_p - U_s curve of three component mixture of Al, Fe₂O₃ and Epoxy with $w_1/w_2/w_3=0.126/0.374/0.5$. Experimental data are from references [4, 5].

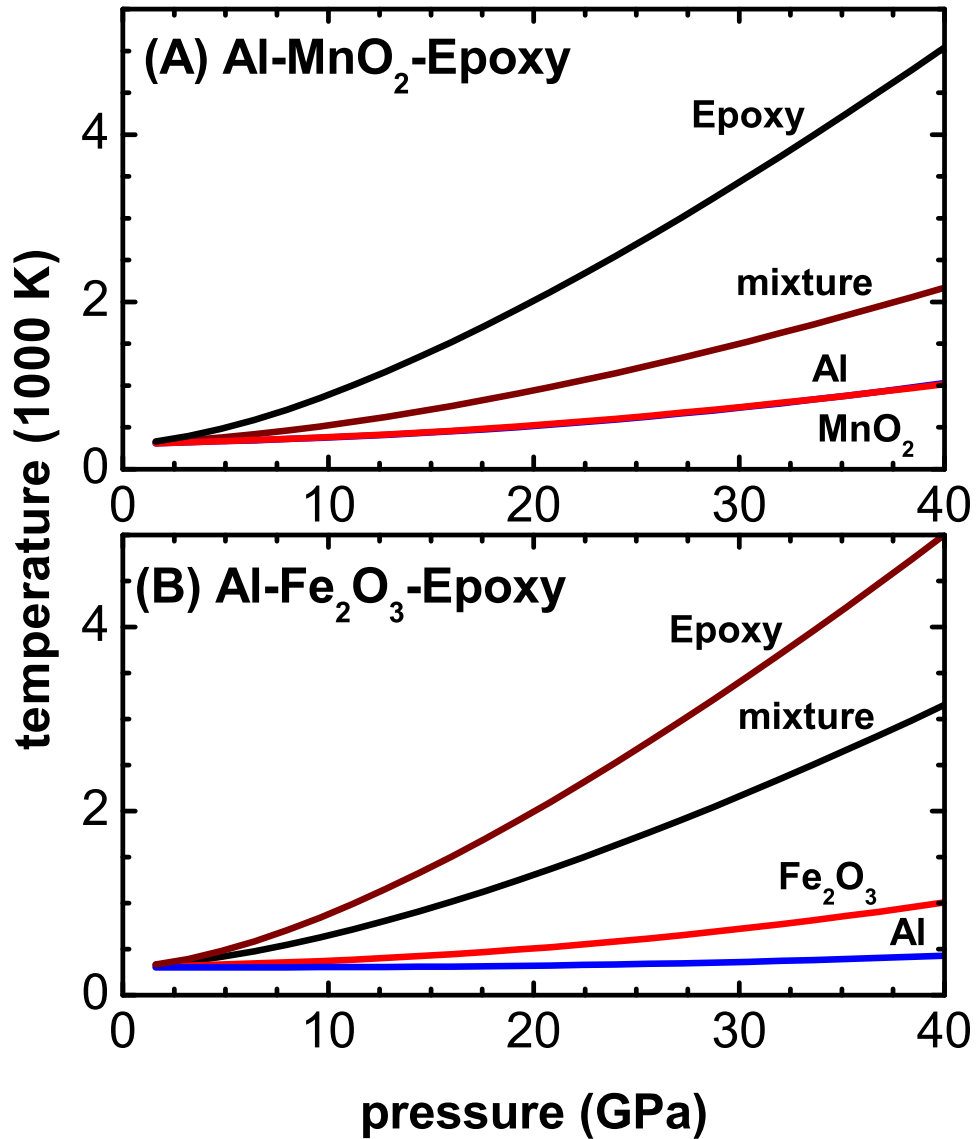


Figure 4.6: (A). Temperature vs. pressure on the Hugoniot of three component mixture of Al, MnO₂ and Epoxy with $w_1/w_2/w_3=0.251/0.537/0.212$. Graphs show component temperatures and average mixture temperature. Temperatures for Al and MnO₂ are almost the same. (B). Temperature vs. pressure on the Hugoniot of three component mixture of Al, Fe₂O₃ and Epoxy with $w_1/w_2/w_3=0.126/0.374/0.5$. Graphs show component temperatures and average mixture temperature.

For computing non-equilibrium temperatures in the components, we have proposed the use of single component criteria. This scheme allows us to compare component temperatures and equilibrium mixture temperature for estimating non-equilibrium effects. The method is applied to two and three component mixtures, and shows good agreement with experimental data. An important aspect of our method is that it predicts the mixture Hugoniot accurately, without any tuning, once the component data are available. The method is readily applicable to porous mixtures, as it is now well known that enthalpy-based approach is better suited to treat porosity effects.

Enthalpy-based equation of state for highly porous materials employing modified soft sphere fluid model

5.1 Introduction

Enthalpy-based equation of state, originally proposed by Rice and Walsh [67] to model the Hugoniot of water, relates specific volume and specific enthalpy via enthalpy parameter and treats pressure and temperature as independent thermodynamic variables. This approach is quite analogous to the Mie-Grüneisen equation of state which treats volume and temperature as independent variables. A key assumption used in applications of enthalpy-based approach, which provides good accuracy, is that the enthalpy parameter depends only on pressure. This leads to the result that constant pressure specific heat is either a constant or a function of entropy [75]. However, a weak dependence of the enthalpy parameter on temperature is accommodated in the formalism discussed below. Shock wave propagation in porous materials, binary mixtures and multi-component systems are areas where enthalpy-based approach is better suited in comparison to Mie-Grüneisen equation of state.

Modeling shock compression of porous materials has remained a topic of considerable interest over several decades [23, 105]. Closure of pores and compression of the material matrix occur first during shock transit [58]. Molecular dynamics simulations of model systems [72, 73] show that the sequence of processes involved are the initial shocking of the solid matrix, shock break out at the pore interfaces and collisional energy dissipation of the ejecta. These processes give rise to formation of hot spots and local heating [74]. High temperatures generated on shock loading of porous materials is due to the collisional energy dissipation, which also gives rise to anomalous expansion in the shocked state for higher initial porosity [71]. The shocked volume of Cu

increases, instead of decreasing, with increasing pressure when initial porosity is more than two. This effect shows up as double valued pressure on the pressure-volume Hugoniot.

A way to simplify thermodynamic modeling of porous materials is to employ the enthalpy-based equation of state. This was realized early by Trunin and co-workers [63] in their method for extrapolating solid Hugoniot to porous states. A parameter relating specific internal energy and specific volume was introduced by them, and also in later studies [64, 65]. But, Wu and Jing developed the ideas in greater detail and applied the enthalpy-based scheme, including modeling of initial compaction, to several materials [66]. The enthalpy parameter is taken as a function of pressure and is computed along the solid Hugoniot in these applications. The method is also applied to mixtures [76, 79], compounds [78] and preheated materials [77]. Viljoen *et al* reviewed several approaches used for modeling porous Hugoniot, and also provided an alternate method to compute the enthalpy parameter [68]. Explicit treatment of electronic effects on the Hugoniot is yet another improvement within this scheme [6].

Particulate nature of components in heterogeneous mixtures determines the time scales for equilibration of thermodynamic variables during shock propagation [86]. While pressure and particles speeds equilibrate fast, non-equilibrium thermal conditions prevail during shock traversal [87, 89]. The Rankine-Hugoniot conservation laws are insufficient, and an additional equation specifying partitioning of energy onto the components of the mixture is needed in these conditions [88]. As pressure equilibrates fast, it is natural to use enthalpy-based approach for thermodynamic modeling of binary solid and porous mixtures [106], as well as multi-component systems [107].

In all the applications discussed above, the enthalpy parameter is computed either along the solid Hugoniot or on the zero temperature isotherm, and has been found adequate enough for lower porosities. However, for higher porosities, the shocked states lie in the expanded volume region corresponding to the fluid phase of the material. This is the case of Cu when porosity is more than two. Then, an appropriate fluid model is needed for applying enthalpy-based

approach to high porosity cases. With this aim in view, we develop a modified soft sphere model [48, 49] to compute the enthalpy parameter and constant pressure specific heat along suitable pressure-volume curves in the fluid region. The essential modification of the soft sphere model is in the determination of all its parameters in terms of bulk modulus, cohesive energy and density of the solid at normal conditions. Hugoniot of Cu with high porosity are then computed using the results of the modified soft sphere model, and compared with experimental data. As observed earlier for polystyrene [71], we also incorporate the effect of energy loss from the shock due to expansion of the shocked material for calculating porous Hugoniot. We, thus, also show that expansion of the vapor in the final phase is an essential feature of shock compression of materials with higher porosity.

The chapter is organized as follows. In section 5.2 we briefly discuss the enthalpy-based equation of state, and derived the formulations for volume and temperature on Hugoniot using the same EOS. The modified soft sphere model for ionic contribution is developed in section 5.3. Results are given in section 5.4. Finally, section 5.5 summaries the work.

5.2 Enthalpy-based equation of state

The enthalpy parameter χ and constant pressure specific heat C_P are defined as $(\partial V/\partial T)_P=(\chi/P)C_P$ and $(\partial H/\partial T)_P=C_P$, respectively. The symbols H , V , P and T denote specific enthalpy, specific volume, pressure and temperature. Both χ and C_P contain thermal ionic and electronic effects, and so may be split into ionic and electronic components as $\chi C_P=\chi_i C_{Pi} + \chi_e C_{Pe}$. Here C_{Pi} and C_{Pe} are, respectively, the constant pressure ionic and electronic specific heats, and $C_P=C_{Pi}+C_{Pe}$. Now, integrating the defining relations from zero temperature, V and H are expressed as

$$V = V_c(P) + \int_0^T \frac{1}{P} \chi_i(P, \tau) C_{Pi}(P, \tau) d\tau + \int_0^T \frac{1}{P} \chi_e(P, \tau) C_{Pe}(P, \tau) d\tau \quad (5.1)$$

$$H = H_c + H_{ti} + H_{te} \equiv H_c(V) + \int_0^T C_{Pi}(P, \tau) d\tau + \int_0^T C_{Pe}(P, \tau) d\tau \quad (5.2)$$

where H_{ti} and H_{te} are, respectively, thermal ionic and thermal electronic specific enthalpy. The reference state parameters V_c and H_c denote, respectively, the zero temperature specific volume and specific enthalpy at pressure P . Specific volume V_c is to be obtained by inverting the zero temperature isotherm of the solid, and is defined by the equation $P_c(V_c) = P$ for the given P . Corresponding specific enthalpy is then obtained as $H_c = E_c(V_c) + P V_c$. For both solid and fluid regions, $P_c(V)$ is quite accurately represented by a formulation [8] due to Li *et al*, which is discussed below.

The Gruneisen parameter for thermal electrons Γ_e is adequately represented by a constant value in the range 0.6 - 0.9 [57]. The lower limit corresponds to Fermi gas model while the upper bound accounts also for pressure ionization. Then, the definition yields the result $\chi_e = \Gamma_e / (\Gamma_e + 1)$ (which is independent of temperature) if electrons are considered independently. For the ion-electron mixture in materials, χ_e should be determined together with χ_i in a consistent manner. In any case, the dependence of enthalpy parameters on temperature is quite weak. This is demonstrated by comparing the variation of χ_i with pressure on the solid Hugoniot and zero temperature isotherm for Al [75, 107] and Cu [6]. This assumption is discussed further below (using Fig. 5.1-A) in section 5.4, where variation of (effective) χ is shown on four pressure-volume curves with varying temperature profiles. So we approximate $\chi_i(P, \tau)$ and $\chi_e(P, \tau)$ in Eq. (5.1) by their values at the upper limits of the integrals. With this approximation, Eqs. (5.1) and (5.2) can be combined together to obtain the generalized enthalpy-based EOS:

$$V = V_c + \frac{1}{P} \chi_i(P) H_{ti}(P, T) + \frac{\chi_e}{P} H_{te}(P, T). \quad (5.3)$$

The weak temperature dependence of $\chi_i(P, T)$ and $\chi_e(P, T)$ will be dropped hereafter. Substituting $H_{ti} = H - H_c - H_{te}$, Eq. (5.3) can be rewritten as

$$V = V_c + \frac{1}{P} \chi_i(P) (H - H_c) + \frac{1}{P} (\chi_e - \chi_i) H_{te}(P, T) \quad (5.4)$$

This expression for $V(P, T)$ defines the enthalpy-based EOS with explicit representation of electronic effects, although it favors ions over electrons. However, we can also eliminate H_{te} from Eq. (5.3) and obtain

$$V = V_c + \frac{1}{P}\chi_e(H - H_c) + \frac{1}{P}(\chi_i - \chi_e)H_{ti}(P, T) \quad (5.5)$$

The last two equations may now be averaged with weight factors $w_i = C_{Pi}/C_P$ and $w_e = C_{Pe}/C_P$, respectively, to arrive at the final expression

$$V = V_c + \frac{1}{P}\chi(P)(H - H_c) + \frac{1}{P}(\chi_e - \chi_i)\left(w_i H_{te}(P, T) - w_e H_{ti}(P, T)\right) \quad (5.6)$$

This expression is symmetric with respect to ions and electrons, and χ is the effective enthalpy parameter defined as $\chi = w_i \chi_i + w_e \chi_e$. The last term, which involves differences of enthalpy parameters and specific enthalpies, is not obtained in earlier treatments [66, 68]. We discuss it further below, however expect it to be only a small correction because of the weight factors employed.

Initial porosity is defined as $\alpha_0 = V_{00}/V_0$, where V_{00} and V_0 are, respectively, initial specific volumes of the porous material and normal solid. For applying Eq. (5.6) to porous materials, the zero temperature volumes V_c is extended to the region $V_0 \leq V_c \leq V_{00}$ using the P- α model [6, 12]. In this approach, the zero temperature energy in the extended region is the same as $E_c(V_0)$, however, pressure increases due to compaction.

5.2.1 Specific volume and temperature on Hugoniot

The Hugoniot equation relating energy E , pressure P and volume V of the shocked material is given by:

$$E - E_{00} + P\Delta V_m = \frac{1}{2}(P + P_{00})(V_{00} - V) \quad (5.7)$$

where E_{00} and P_{00} are, respectively, the specific energy and pressure at initial volume V_{00} . We already mentioned that the variables for the shocked state occur in the fluid region for higher porosities. We introduced a new term $P\Delta V_m$ in Eq. (5.7) to account for the energy spend by the shock to expand the material to final volume V . Need to consider such endothermic processes after the sharp rise of shock-pressure was first motivated from experiments on highly porous polystyrene [71]. For modeling the Hugoniot, these authors used a real gas EOS and a constant energy term in place of $P\Delta V_m$, which is simply the

work done by the shock to expand the vaporized material by ΔV_m . We expect ΔV_m to depend on initial porosity and micro-structural details of the material, and to be small (with respect to V_0) for lower porosities. Thereafter it would increase and finally saturate at high porosities. For applications we shall represent it as $\Delta V_m = \Delta V_{max} (\alpha_0 - a)/(\alpha_0 + b)$ for $\alpha_0 \geq a$, where ΔV_{max} is the limiting volume change due to expansion and a and b are two material constants. For Cu we find that $\Delta V_{max}=0.156 \text{ cm}^3/\text{g}$, $a=1.703$ and $b = 3.045$ (see Fig. 5.4-A).

Elimination of $H=E+PV$ between Eqs. (5.7) and (5.6) yields the volume-pressure curve:

$$V = 2V_c \frac{1 - \chi}{2 - \chi^*} + \frac{\chi}{2 - \chi^*} \left(V_{00}(1 + P_{00}/P) + \frac{2}{P}(E_{00} - E_c(V_c) - P\Delta V_m) \right) + \frac{2}{P} \frac{\chi_e - \chi_i}{2 - \chi^*} \left(w_i H_{te}(P, T) - w_e H_{ti}(P, T) \right) \quad (5.8)$$

where $\chi^* = \chi(1 - P_{00}/P)$. This expression reduces to those given by Wu and Jing [66] and Viljoen [68] when either $\chi_e = \chi_i$ or the enthalpy difference $w_i H_{te} - w_e H_{ti} = 0$. The second case arises if the constant pressure ion and electron specific heats are proportional to the same function of temperature. This is a consequence of the choice of weight factors w_i and w_e . Explicit terms accounting for electronic effects, thus, vanish identically in these situations. All the details of the derivation, for correctly incorporating electronic effects, have already been discussed in detail [6]. Volume in Eq. (5.8) is determined together with the solution of the differential equation for temperature along the Hugoniot, viz.,

$$\frac{d}{dP} T - \frac{\chi}{P} T(P) = \frac{1}{2C_P} \left((V_{00} - V) + (P - P_{00})dV/dP \right) \quad (5.9)$$

Here χ is the effective parameter and C_P is total specific heat. This equation, which is similar to Walsh-Christian differential equation [81], is easily discretized using a forward finite difference scheme:

$$(1 - \Delta P \chi_n/P_n)T_n = T_{n-1} + 0.5 \left((V_{00} - V_n)\Delta P + (P_n - P_{00})(V_n - V_{n-1}) \right) / C_{P,n} \quad (5.10)$$

Here the subscript n on different variables denotes their respective values at $P_n = P_{00} + n \Delta P$ where ΔP is an increment in pressure, and $n=1, 2, 3$ etc. Numerical values of V_n corresponding to P_n are given by Eqs. (5.8). The fluid

model, which is outlined below, is used to obtain ion and electron enthalpies and specific heats. Thus, Eqs. (5.8) and (5.10) are evaluated iteratively at each P_n . Starting with a guess value of T_n , say T_{n-1} , first V_n is computed using Eq. (5.8). Then Eq. (5.10) is used to get an improved value of T_n . These steps are, then, repeated until values of T_n between successive iterates are within a prescribed error. The iterations converge in few steps. Finally, the whole process is repeated for $n=1, 2, 3$ etc., thereby obtaining volume and temperature along the Hugoniot in a consistent manner.

5.3 Modified soft sphere model

A modification of the well known soft sphere model [48, 49] for liquid metals in the fluid region ($V \geq V_0$) is discussed below. This model is characterized in terms of an inter-particle repulsive potential $\phi(r) = \epsilon(\sigma/r)^n$ where ϵ and σ are, respectively, the energy and length scale parameters and the power law exponent n is in the range $1 \leq n \leq 12$. The lower limit corresponds to Coulomb potential. The specific free energy of the model is expressed as [108, 109]

$$F(V, T) = -Nk_B T \ln\left(\frac{Ve}{N\lambda^3}\right) + Nk_B T \frac{Q}{2}(n+4)\left(\frac{V_0}{V}\right)^{n/9} \left(\frac{\epsilon}{k_B T}\right)^{1/3} + E_{c\ soft}(V), \quad (5.11)$$

where N is number of atoms per gram and k_B is Boltzmann constant. The thermal deBroglie wavelength is $\lambda = h / \sqrt{2\pi m k_B T}$ and Q is a parameter introduced to account for thermal electron effects. Normal volume V_0 is related to σ as $V_0 = N \sigma^3 / \sqrt{2}$. The first term in Eq. (5.11) is the ideal gas free energy. The second term is obtained by fitting Monte Carlo simulation data of internal energy minus a zero temperature contribution. The subtracted contribution is $(N \epsilon / 2) C_n (V_0/V)^{n/3}$ where C_n is the lattice sum for the potential for FCC lattice [48]. Finally, the last term $E_{c\ soft}$ represents the total zero temperature specific energy, which is expressed as

$$E_{c\ soft} = N\epsilon C_n \left(\frac{V_0}{V}\right)^{n/3} - N\epsilon \left(\frac{V_0}{V}\right)^{m^*} + E_c, \quad (5.12)$$

where E_c is related to the cohesive energy of the solid in normal conditions. Note that the first term is of the soft sphere model. Further, $N \epsilon (V_0/V)^{m^*}$ is a van der Waals term with exponent m^* which is added empirically so that

the last two terms account for the attractive component of zero temperature specific energy. All the earlier applications of soft sphere model involved fitting five parameters ϵ , σ , n , m^* and Q to fluid data like vapor pressure vs. temperature, isobaric expansion data, etc. [49, 108–110]. This model provides an analytical expression for Gruneisen parameter in the fluid phase [111], it is also in use for fitting quantum molecular dynamics data on liquid metals [112]. Our modification is in determining the parameters of the model from properties of the solid.

5.3.1 Generalized Lennard Jones model

In the modified soft sphere model, we propose to use Eq. (5.11), however, with $E_{c\ soft}$ replaced by a generalized Lennard-Jones formula for zero temperature energy (and pressure):

$$E_{LJ}(V) = \frac{E_{coh}}{n-m} \left[m \left(\frac{V_{c0}}{V} \right)^{n/3} - n \left(\frac{V_{c0}}{V} \right)^{m/3} \right], \quad (5.13)$$

$$P_{LJ}(V) = \frac{E_{coh}}{n-m} \frac{n}{3} \frac{m}{V_{c0}} \left[\left(\frac{V_{c0}}{V} \right)^{1+n/3} - \left(\frac{V_{c0}}{V} \right)^{1+m/3} \right], \quad (5.14)$$

where V_{c0} is the reference volume at zero temperature and the exponents n and m are to be determined in terms of cohesive energy E_{coh} per gram, bulk modulus B_0 and its pressure derivative B'_0 at conditions $T=0$ and $P=0$.

Several authors have introduced the generalized Lennard-Jones model for $V > V_{c0}$. Together with experimental values of E_{coh} and V_{c0} , Young and Corey used an expression as in Eq. (5.13) and fitted the exponents n and m to obtain liquid-vapor critical point data for many materials [97]. An alternate approach is to start with a pair potential

$$U(r) = \frac{\epsilon}{n-m} \left[m \left(\frac{r_e}{r} \right)^n - n \left(\frac{r_e}{r} \right)^m \right], \quad (5.15)$$

where ϵ and r_e are, respectively, the equilibrium bond energy and nearest neighbor distance. Then the cohesive energy of different lattices (like FCC) can be computed in terms of lattice sums C_n and C_m for arbitrary n and m . Further determined the parameters (ϵ , n and m) using experimental data of E_{coh} and B_0 , but accounted only for nearest neighbor atoms [113]. Zhen and Davies

revised this approach by considering up to 14 neighbors and corrections for the remaining sites [114]. However, these authors used an assumption $n \approx 2m$ for determining the best values of three parameters (ϵ , n and m) in terms of E_{coh} and B_0 . Again, restricting to nearest neighbors, Jiuxun invoked two requirements [115], viz., (i) $V(P)$ is analytic function of P and (ii) the bulk modulus $B(P)$ scales as $B(P) \sim (P - P_{sp})^{1/2}$, where P_{sp} is the spinodal pressure defined as $B(P_{sp})=0$. These requirements provide a condition $1+n/3=2(1+m/3)$ (i.e., $m=(n-3)/2$) relating the exponents [115], thereby removing the ad-hoc assumption $n \approx 2m$. Further, Jiuxun used experimental values of B_0 and B'_0 to get the remaining two parameters. Thus cohesive energy E_{coh} is not used in Jiuxun's approach.

As discussed below, we find it is easier to start with Eq. (5.13), in lieu of Eq. (5.15), to determine the parameters n and m and then deduce the pair potential. This scheme is better as it avoids repeated computations of C_n and C_m in the fitting processes. We shall employ the analyticity conditions of Jiuxun to relate the exponents, however, we shall use values of E_{coh} and B_0 and predict B'_0 and critical point data for comparison.

5.3.2 Energy parameters and exponents

We now introduce a generalized Lennard-Jones pair potential as

$$U_{LJ}(R) = \epsilon_{rep} \left(\frac{\sigma}{R} \right)^n - \epsilon_{att} \left(\frac{\sigma}{R} \right)^m, \quad (5.16)$$

where ϵ_{rep} and ϵ_{att} , respectively, denote repulsive and attractive energy scales. Then, E_{LJ} is readily computed via lattice sum as:

$$E_{LJ}(V) = \frac{\epsilon_{rep}}{2} \sum_k N_k \left(\frac{\sigma}{R_k} \right)^n - \frac{\epsilon_{att}}{2} \sum_k N_k \left(\frac{\sigma}{R_k} \right)^m, \quad (5.17)$$

where R_k and N_k are, respectively, the radius and number of atoms in the k^{th} shell around a test atom. For an FCC lattice, this expression reduces to

$$E_{LJ}(V) = \frac{\epsilon_{rep}}{2} C_n \left(\frac{V_{c0}}{V} \right)^{n/3} - \frac{\epsilon_{att}}{2} C_m \left(\frac{V_{c0}}{V} \right)^{m/3}, \quad (5.18)$$

where $V_{c0} = N \sigma^3 / \sqrt{2}$, and the lattice sum C_n (and similarly C_m) is defined as $C_n = \sum_k N_k (1/\sqrt{k})^n$. Further, comparing Eqs. (5.13) and (5.18), we readily find that

$$\epsilon_{rep} = E_{coh} \frac{2}{C_n} \frac{m}{n-m}, \quad \epsilon_{att} = E_{coh} \frac{2}{C_m} \frac{n}{n-m}, \quad (5.19)$$

as $(V_{c0}/V)^{n/3}$ and $(V_{c0}/V)^{m/3}$ are linearly independent functions. Bulk modulus B_0 and its pressure derivative B'_0 computed from Eq. (5.14) are given by

$$B_0 = E_{coh} \frac{n m}{9 V_{c0}}, \quad B'_0 = 2 + \frac{n}{3} + \frac{m}{3}. \quad (5.20)$$

These relations imply that n and m are obtained as roots of the quadratic equation $x^2 - 3(B'_0 - 2)x + 9B_0 V_{c0}/E_{coh} = 0$. However, in general, experimental data on V_{c0} , E_{coh} , B_0 and B'_0 lead to complex values of exponents [116], as is the case for Cu ($V_{c0} = 0.1119 \text{ cm}^3/\text{g}$, $B_0 = 134.8 \text{ GPa}$, $B'_0 = 5.193$, $E_{coh} = 5.302 \text{ kJ/g}$). Therefore we find it better to use three parameters, out of V_{c0} , E_{coh} , B_0 and B'_0 , in such situations. We propose to use of the relation $m = (n-3)/2$ which arise out of analyticity considerations [115]. Then, the first relation in Eq. (5.20) shows that n is determined from the quadratic equation $n^2 - 3n - 18B_0 V_{c0}/E_{coh} = 0$. Taking the positive root, this equation gives $n = 8.803$ and $m = 2.901$ for Cu. Then, B'_0 is obtained as 5.902 which may be compared with experimental value 5.193. Zhen and Davies [114] give the exponents $n = 8$ and $m = 5$, and hence $B'_0 = 6.333$. On the other hand, following Jiuxun [115], use of B'_0 in lieu of E_{coh} gives $n = 2B'_0 - 3$ which yields $n = 7.386$ and $m = 2.193$. Then E_{coh} is found to be 8.381 kJ/g while its experimental value is 5.302 kJ/g. We, therefore, find it more appropriate to use V_{c0} , B_0 and E_{coh} in determining the exponents since it is important to retain the correct cohesive energy. In case Eq. (5.20) provides real roots, n and m are readily determined in terms of all the four parameters.

The accuracy of the generalized Lennard-Jones model outlined above can be assessed by comparing it with a formulation developed by Li *et al* [8] which employ all the four parameters, V_{c0} , B_0 , B'_0 and E_{coh} . This formulation provides very accurate values of the zero temperature energy and pressure for a variety of materials [8] in the compression ($V \leq V_{c0}$) as well as expanded ($V > V_{c0}$) region. Comparison of this formulation for Cu with Eqs. (5.13) and (5.14) (see Fig. 5.1-B) shows that the generalized Lennard-Jones model provides adequate

accuracy.

5.3.3 Total energy and pressure

As all the parameters of generalized Lennard-Jones model are related to material constants, $E_{c\ soft}$ in Eq. (5.11) can now be replaced with E_{LJ} given in Eq. (5.13). Then, ionic energy and pressure within the modified soft sphere model are given by

$$E_{soft}(V, T) = Nk_B T \left[\frac{3}{2} + \frac{1}{6}(n+4) \left(\frac{V_0}{V} \right)^{n/9} \left(\frac{\epsilon_{rep}}{k_B T} \right)^{1/3} \right] + E_{LJ}(V), \quad (5.21)$$

$$P_{soft}(V, T) = \frac{Nk_B T}{V} \left[1 + \frac{1}{18}n(n+4) \left(\frac{V_0}{V} \right)^{n/9} \left(\frac{\epsilon_{rep}}{k_B T} \right)^{1/3} \right] + P_{LJ}(V) \quad (5.22)$$

As mentioned earlier, the correction to ideal gas thermal energy (second term in brackets) is determined from Monte Carlo simulations [48] for $4 \leq n \leq 12$. A few differences in the modified soft sphere model, in comparison to its earlier implementations [49, 108, 110], are the following:

- In lieu of fitting, three material constants V_{c0} , B_0 and E_{coh} are employed to determine all the parameters.
- The repulsive energy parameter ϵ_{rep} and exponent n so obtained are directly employed in the soft sphere free energy.
- No multiplicative constant Q is adjusted to account for electronic contribution [49], which we consider separately next.

The states reached at the final shocked condition for porosities in the range 2-10 for Cu are in the dense liquid metal region with densities more than 3.7 g/cm^3 . Significant number of free electrons would be present at these densities as in the solid state. So we propose to use electronic contributions to the EOS based on Thomas-Fermi models [55] appropriately corrected to account for low temperature specific heat. Thermal electron energy and pressure, which incorporates this correction, and also approach the classical values at high tempera-

tures, are accurately expressed as: [53, 57]

$$E_{te}(V, T) = \frac{9\zeta^2}{4\beta(V)} \log \cosh \left(\frac{2\beta T}{3\zeta} \right), \quad \zeta = \frac{0.85X^{0.59}}{1 + 0.85X^{0.59}} ZR, \quad X = \frac{T}{Z^{4/3}} \quad (5.23)$$

$$P_{te}(V, T) = \frac{1}{V} \frac{1}{\Gamma_e} \frac{\zeta^2}{\beta(V)} \log \cosh \left(\frac{\Gamma_e \beta T}{\zeta} \right), \quad \beta(V) = \beta_0 (V/V_0)^{\Gamma_e} \quad (5.24)$$

where Z and R are, respectively, atomic number and gas constant. For low temperatures, *i.e.* $T \lesssim T_F$ the Fermi temperature, Eq. (5.23) reduces to $0.5 \beta T^2$ while in the higher temperature limit, *i.e.* $T \gtrsim T_F$, it goes over to ideal gas limit, $(3/2) N_g k_B T$, where N_g is the number of electrons per gram. These terms are added to Eqs. (5.21) and (5.22) to get total energy and pressure.

5.4 Results and discussion

5.4.1 Ionic enthalpy parameter

Using the defining equation, the ionic parameter χ_i is also expressed as $\chi_i = P \Gamma_i / K_{Si}$, where K_{Si} is iso-entropic bulk modulus and Γ_i is ionic Gruneisen parameter. It is common practice to compute χ_i in the solid phase either on the experimental pressure-volume Hugoniot curve [66, 68] or the zero temperature isotherm [75, 79, 106]. We have outlined an alternate method [6] for its computation along any arbitrary pressure-volume curve using a three component EOS. This approach uses zero temperature isotherm developed by Li *et al* [8], Thomas-Fermi model [53, 55] for electrons and an accurate ionic model due to Johnson [47], which also includes melting effects. However, the ionic model is suitable only for the part of P-T-V region corresponding $V \leq V_0$. We already pointed out that for higher initial porosities (*e.g.*, $\alpha_0 > 2$ for Cu) the final Hugoniot states are in the liquid-vapor region where $V > V_0$.

For the region $V > V_0$, we propose to use the modified soft sphere model discussed above. All response functions like Γ_i , isothermal bulk modulus K_{Ti} and constant volume specific heat C_{Vi} are easily obtained in terms of V and T using Eqs. (5.21) and (5.22). Then the thermodynamic relation $K_{Si}/K_{Ti} = C_{Pi}/C_{Vi} = 1 + (T/V) \Gamma_i^2 C_{Vi}/K_{Ti}$ provides K_{Si} and C_{Pi} . All these functions can also be determined for ion-electron system using expressions for total pressure and energy.

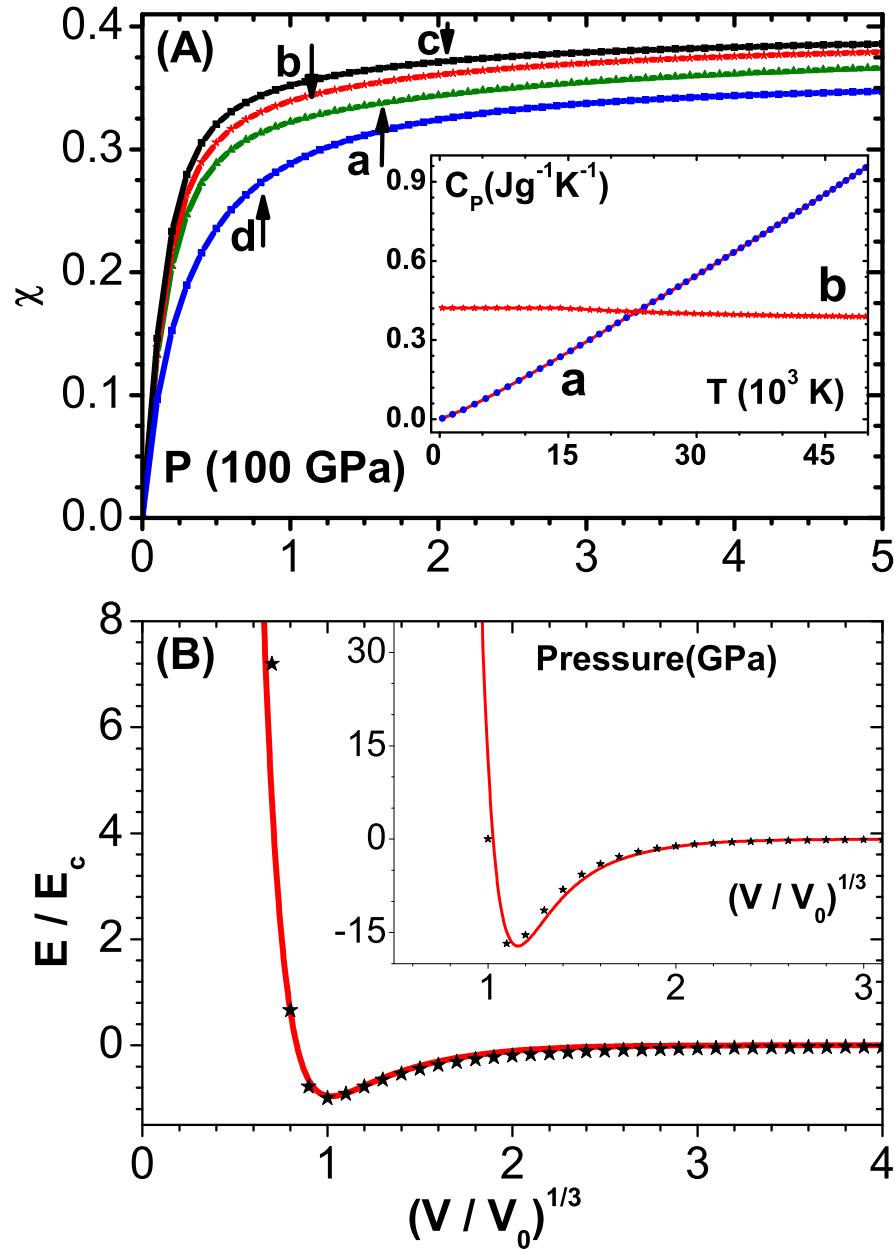


Figure 5.1: (A) Variation of χ vs. P for Cu. Curves a, b and c show χ using soft sphere model along the curves $V_1(P)$, $V_2(P)$ and $V_3(P)$ defined in the text. Curve-d shows χ along the solid Hugoniot obtained using U_s - U_p data. Inset figure shows variation of constant pressure specific heats C_{P_i} and C_{P_e} vs. temperature along $V_2(P)$. (B) Comparison of scaled cohesive energy vs. scaled inter particle distance $(V/V_0)^{1/3}$. Solid line: 4-parameter model [8], Symbols: generalized Lennard-Jones model Eq. (5.13)

Then, electronic parameters χ_e and C_{Pe} are determined from defining relations. Finally, χ , χ_i and χ_e are computed on any specified pressure-volume curve after obtaining temperature from $P(V, T)$ relations. We consider pressure-volume curves defined by the relation: $V_\lambda(P) = V_0 + \lambda (V_0 - V_H(P))$, where $V_H(P)$ is the specific volume on the solid Hugoniot, and λ is a real parameter. For example, $\lambda=0$ provides the pressure-axis at V_0 . Similarly, while $\lambda=-1$ gives the solid Hugoniot itself, $\lambda=1$ yields its mirror image about the pressure-axis at V_0 . The curves corresponding to $\lambda=-1, 1, 2$ and 3 are shown in Fig. 5.3-A.

Variation of (effective) χ with pressure along these curves is shown in Fig.5.1-A. More explicitly, curves marked a, b and c in this figure, correspond to, $V_1(P)$, $V_2(P)$ and $V_3(P)$, respectively. Temperature on these curves at 200 GPa are about 53900 K, 63800 K and 70600 K, while the corresponding χ values are 0.344, 0.361 and 0.371. Value of χ on the solid Hugoniot (shown in curve-d) is about 0.324 and corresponds to 6100 K. These results show the weak dependence of χ on temperature, which is mainly because higher pressures result from thermal contributions in the liquid-vapor region, and the EOS approaches ideal gas behavior. The insert curve in this figure shows C_{Pi} vs. temperature. The soft sphere contribution to C_{Pi} is found to drop off within about 2000 K.

5.4.2 Vapor-liquid phase diagram

A set of four isotherms shown in Fig. 5.2-A for Cu display the familiar van der Waals loops. The vapor-liquid phase diagram we have obtained is also shown in Fig. 5.2-B. The critical point parameters are $\rho_c = 2.246 \text{ g/cm}^3$, $T_c = 8345 \text{ K}$ and $P_c = 8.935 \text{ GPa}$. All these parameters lie within the range quoted in literature [108]. Our calculations do not include electronic terms as the aim is to compare the phase diagram with a recent molecular dynamic simulation using an effective inter-atomic potential [9], which is also shown in the figure. The latter work is based on obtaining zero temperature isotherm from DFT calculations, then fitting an effective pair potential, and finally employing molecular dynamic simulations for the fluid phase. The comparison is good except in the dense liquid portion.

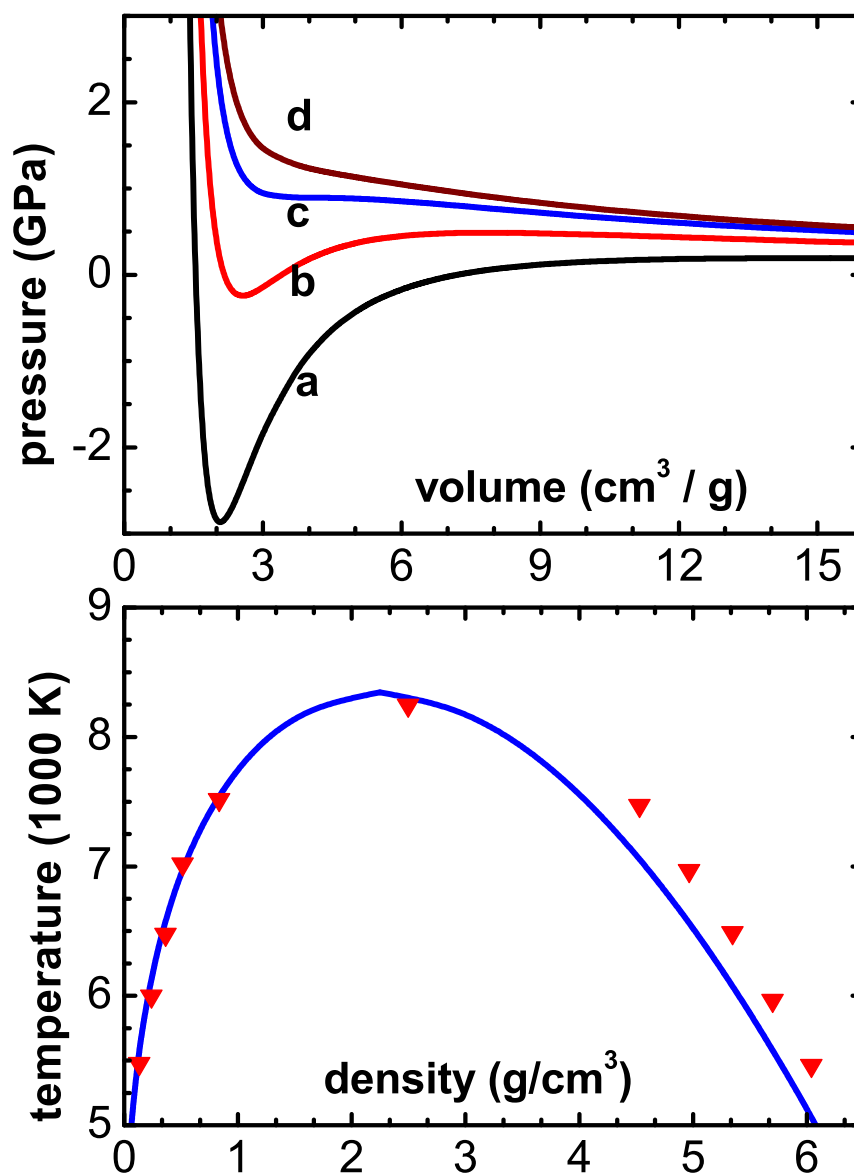


Figure 5.2: (A) Isotherms of Cu using the modified soft sphere model: (a) $T=5000$ K, (b) $T=7000$ K, (c) $T=8236$ K and (d) $T=9000$ K. (B) Liquid-Vapor phase diagram of Cu within the modified soft sphere model. Symbols are simulation data [9]

5.4.3 Porous Hugoniot

We applied the method developed above for Cu with porosities in the range from 2 to 10. We have used enthalpy parameters determined along the pressure-volume curve $V_2(P)$ ($\lambda=2$) for all the results given below. However, the specific heats are computed as functions of P and T using the EOS model. The contributions of the enthalpy difference term in Eq. (5.8) are shown in Fig. 5.3-B for the cases $\alpha_0 = 3, 5$ and 7 . As expected its maximum contribution is only about 7 %. It is the specific choice of weight factors $w_i = C_{Pi}/C_P$ and $w_e = C_{Pe}/C_P$, which makes the enthalpy difference term small. Pressure-volume Hugoniot curves shown in Fig. 5.4-B show good agreement with experimental data available in literature [3]. This comparison is much better than that obtained earlier [6] using models corresponding to compressed solid. Values of ΔV_m , which represents the volume change due to vapor expansion are shown in Fig. 5.4-A. For porosity $\alpha_0 = 2$, $\Delta V_m \sim 0$ as most of the shocked states are close to V_0 . Thereafter it increases linearly with porosity, indicating more expansion, but shows a saturating trend for higher α_0 . We expect this variation to be typical for other materials. These values of ΔV_m have been used to get the results of pressure-volume curves.

Comparisons of data of shock speed vs. particle speed are shown in Fig. 5.5-A. The results of the present model compare very well with experimental results. The intercept of all curves on the shock speed axis is negligible, thereby showing small sound speeds at these porosities. Here also, the comparison is much better than what was obtained earlier [6]. Temperature vs. pressure curves along the Hugoniot for different porosities are shown in Fig. 5.5-B. These temperatures are lower than those obtained earlier [6] because volumes on the pressure-volume curves are lower than earlier results.

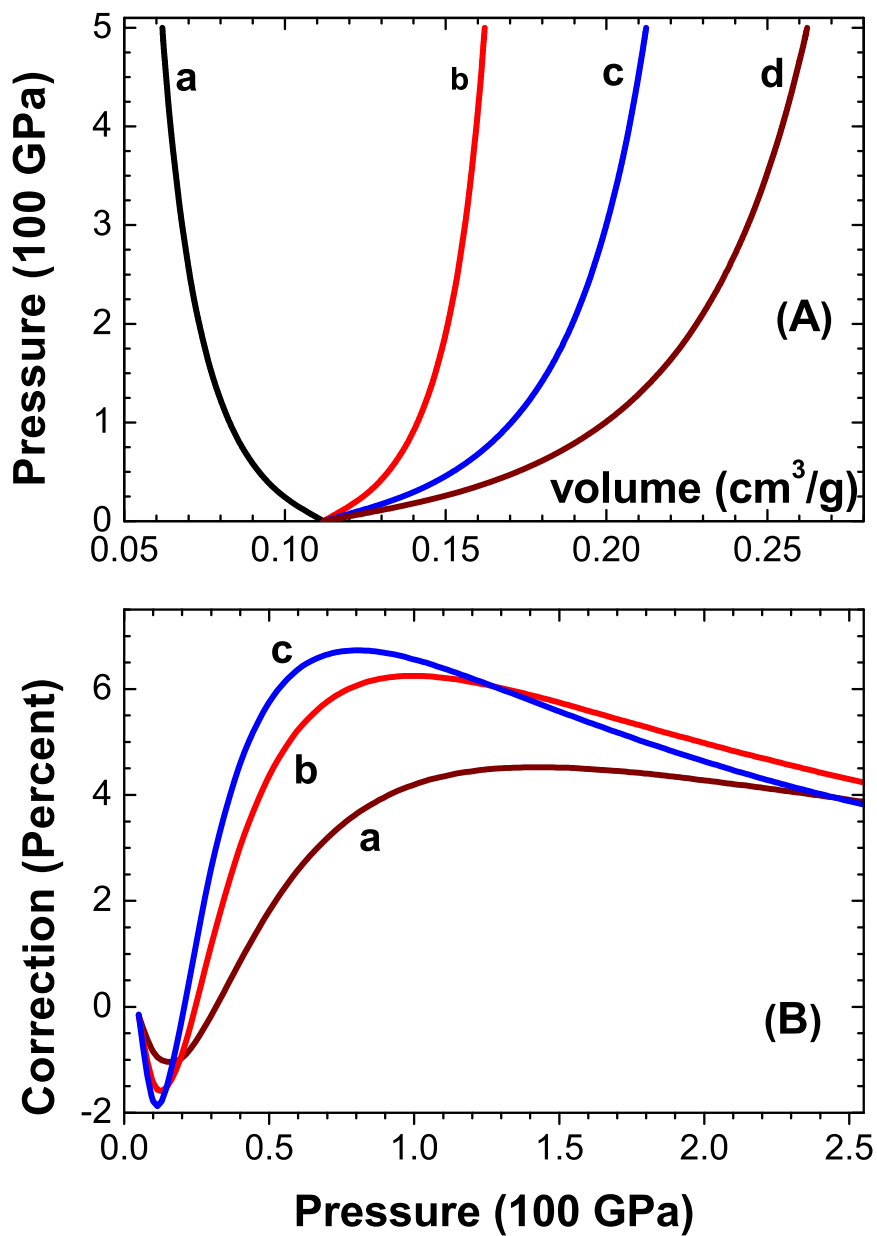


Figure 5.3: (A) Pressure-volume curves $V_\lambda(P)$ defined in the text: Curves a, b, c and d depict V_{-1} , V_1 , V_2 and V_3 , respectively. (B) Percentage contribution of the enthalpy difference term in Eq. (5.8): Curves a, b and c are for $\alpha_0=3$, 5 and 7, respectively.

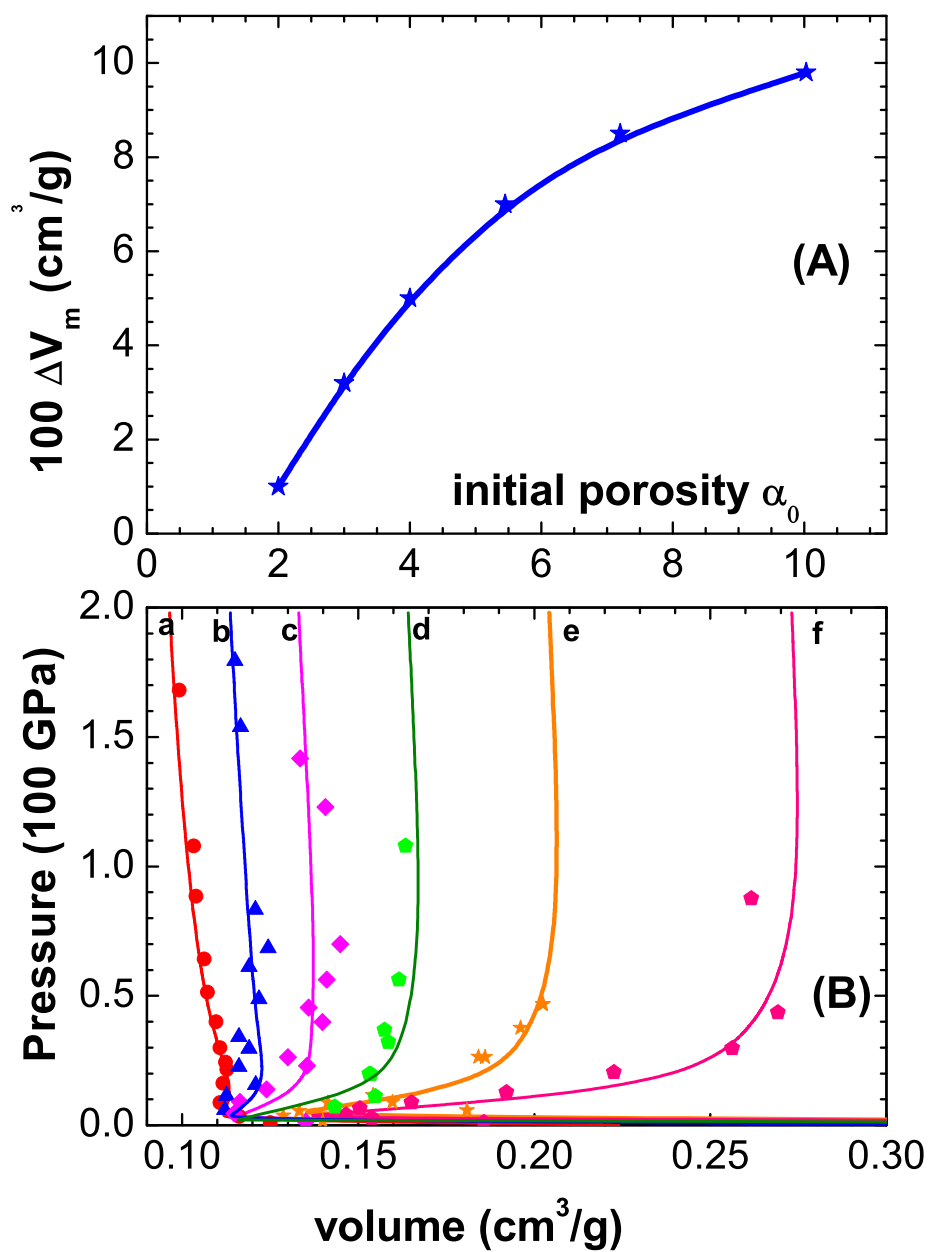


Figure 5.4: (A) Variation of ΔV_m vs. initial porosity for Cu. (B) Comparison of pressure-volume curves of Cu for different initial porosities. (a) $\alpha_0=2$, (b) $\alpha_0=3$, (c) $\alpha_0=4$, (d) $\alpha_0=5.45$, (e) $\alpha_0=7.2$, (f) $\alpha_0=10.03$. Symbols are experimental data [3].

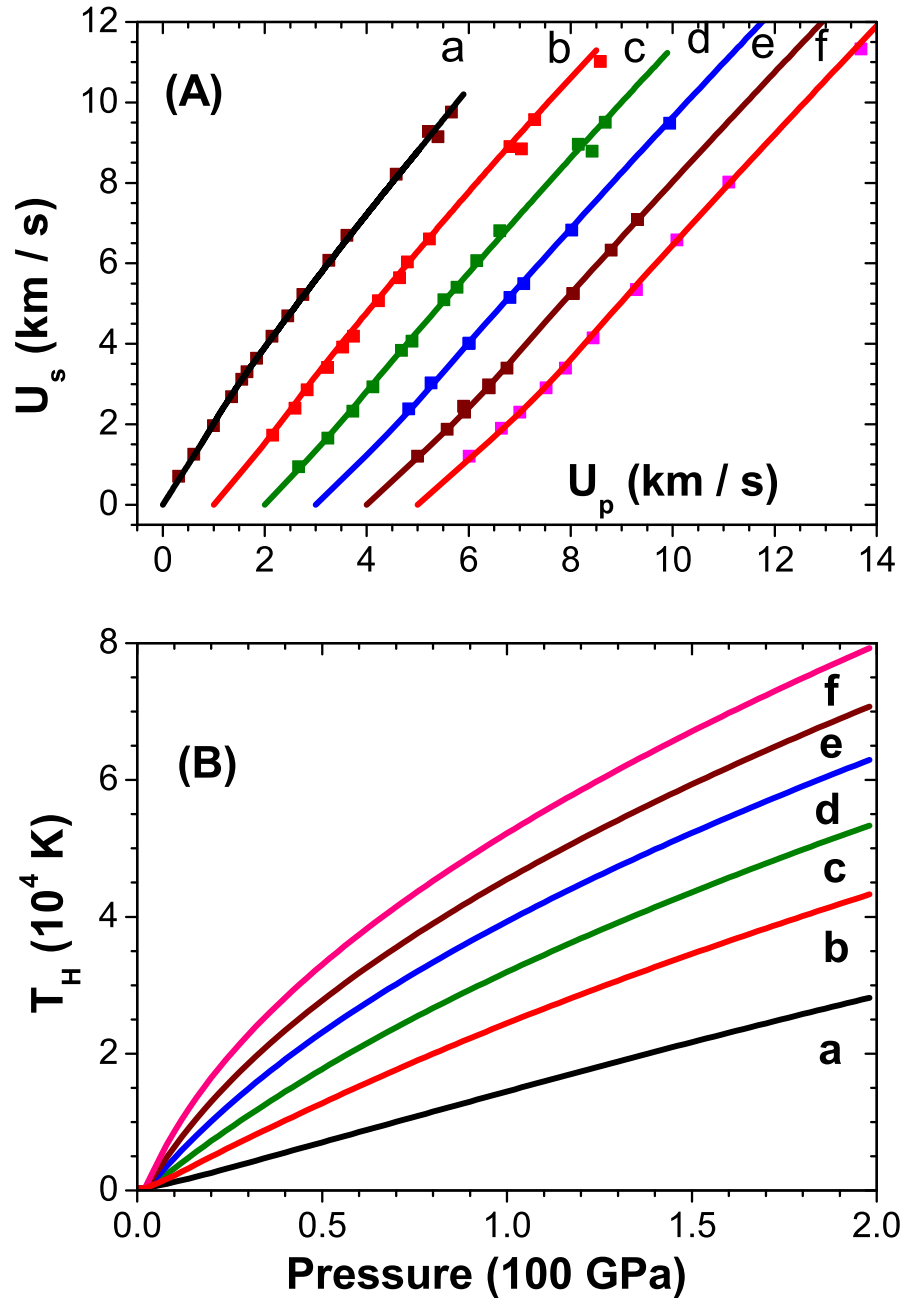


Figure 5.5: (A) Comparison of U_s - U_p curves of porous Cu. (a) $\alpha_0=2$, (b) $\alpha_0=3$, (c) $\alpha_0=4$, (d) $\alpha_0=5.45$, (e) $\alpha_0=7.2$, (f) $\alpha_0=10.03$. Curves b - f are shifted successively to right by 1 unit. Symbols are experimental data [3]. (B) Temperature vs. pressure on the Hugoniot of Cu. (a) $\alpha_0=2$, (b) $\alpha_0=3$, (c) $\alpha_0=4$, (d) $\alpha_0=5.45$, (e) $\alpha_0=7.2$, (f) $\alpha_0=10.03$.

5.5 Summary

An approach based on enthalpy-based EOS is developed in this paper to model the Hugoniot states of highly porous materials. This development is motivated from the observation that the shocked states of these materials are in the expanded fluid region, and so the EOS also should be based on models appropriate for this region. In fact, all the earlier applications of enthalpy-based approach used EOS models applicable for compressed solids and hence low porosities. With the aim just mentioned, a modified soft sphere model for the fluid region is evolved first. The main modification lies in determining all the parameters of the soft sphere model in terms of three experimental data, viz., density, cohesive energy and bulk modulus of the solid at normal conditions. It is then applied to obtain the liquid-vapor co-existence curve of Cu and the results are in good agreement with those from detailed molecular dynamics simulations.

With an appropriate model for the fluid region at hand, it is then used to compute the enthalpy parameters and constant pressure specific heats. These are determined on a pressure-volume curve in the liquid-vapor region. We have also incorporated the energy loss from the shock due to expansion of the shocked vapor to the final volume. Experimental data on Cu with initial porosities in the range 2-10 is then compared with results of the model. Pressure-volume curves and shock speeds vs. particle speeds show good comparison.

Numerical simulation of shock propagation in porous materials using enthalpy-based equation of state

6.1 Introduction

Propagation of shock waves in condensed matter is a topic of great importance in high energy density systems, like stellar structures, inertial confinement fusion, nuclear weapons, etc. The propagation of shock generates hydrodynamic motions in the materials. As a consequence, the state variables such as density, pressure, internal energy, particle velocity etc., of the material change in space and time.

Many experimental techniques are employed in shock propagation studies [117]: (i) the free-surface capacitor [118], (ii) the quartz gage [119, 120], (iii) the Manganin gage [121], and (iv) the axially symmetric magnetic (ASM) probe [122]. The free-surface capacitor measures directly the free-surface velocity of the target upon shock unloading. This technique can also resolve the elastic-plastic behavior of materials which occur at moderate pressures. The quartz gage measures the pressure at the interface of the sample and gage by employing the piezoelectric response of crystalline quartz. The shock wave transmitted from the sample to quartz generates a current due to dielectric polarization which is proportional to the instantaneous difference in stress at the gage interface. The Manganin gage which has a relatively large positive piezo-resistive coefficient is used to record pressure profiles inside the sample. The ASM probe is useful in studying insulators [123], detonating explosives [124, 125], high explosive driven metal plates, and the quasi-elastic structures in metals.

In this chapter we study shock wave propagation via numerical simulations of the Euler equations describing conservation laws of mass, momentum and

energy. Mainly there are two approaches in use for numerical solution of hydrodynamic equations, viz., Eulerian and Lagrangian schemes [126]. Motion of the material is observed from a fixed reference frame with time in Eulerian scheme. However, in Lagrangian approach the material motion is observed in a reference frame moving with the local velocity in the fluid. Equation of state (EOS) of the material is an important ingredient in numerical simulations.

We have simulated plate impact experiments in this study. Generally the Mie-Grüneisen EOS is employed in numerical simulations because it gives pressure as a function of density and internal energy. These variables are updated in a time step in all meshes and the EOS readily provides the new pressure profiles. Detailed EOS tables, which give values of pressure and energy at different density and temperature are also used in numerical simulations. One of the aims of our study is to describe the use of generalized enthalpy-based EOS, which provides a better description for porous materials. Here volume is expressed in terms of pressure and enthalpy, and so pressure has to be obtained via a root finding method.

We use a one dimensional Flux-Corrected Transport algorithm for solving the conservation equations of inviscid fluid flow. It has second order accuracy with reference to time step and has minimum residual diffusion. Positivity and monotonic features of the fluid variables are preserved within this method. It has been shown to be very useful to resolves steep gradients in fluid flow problems [127].

The chapter is organized as follows. Section 6.2 describes the conservation laws in Eulerian and Lagrangian schemes. The details of numerical algorithm for flux corrected transport (FCT), and various boundary conditions used in simulations are given in section 6.3. The EOS formulations mentioned above are discussed in section 6.4. In section 6.5 we discuss the numerical simulation results of few plate impact experiments. Finally, section 6.6 summarizes the present work.

6.2 Euler's conservation equations

6.2.1 Eulerian scheme

As pointed earlier, in Eulerian scheme we observe the motion of the fluid from a fixed reference frame with respect to time [126, 128, 129]. Thus the time rate of change of any state variable is simply the partial derivative with respect to time. The conservation equations in Eulerian scheme are given by :

$$\frac{\partial \rho}{\partial t} + \vec{\nabla} \cdot (\rho \vec{u}) = 0 \quad (6.1)$$

$$\frac{\partial(\rho \vec{u})}{\partial t} + \vec{\nabla} \cdot (\vec{u} \rho \vec{u}) = -\vec{\nabla} P + \rho \vec{g} \quad (6.2)$$

$$\frac{\partial(\rho E_t)}{\partial t} + \vec{\nabla} \cdot (E_t \rho \vec{u}) = -\vec{\nabla} \cdot (P \vec{u}) + \rho \vec{g} \cdot \vec{u} \quad (6.3)$$

where Eqs. (6.1), (6.2) and (6.3) are mass, momentum and energy conservation equations, respectively. Here, \vec{u} , ρ , P and E_t are, respectively, velocity, density, pressure and total energy per unit mass of the substance. Terms involving divergences account for net flow of the fluid variable (like mass, momentum or energy) out of a volume element. The terms on the right hand side are the driving sources. Total energy per unit mass is sum of the specific internal energy (E) and specific kinetic energy, and is given by

$$E_t = E + \frac{1}{2} \vec{u} \cdot \vec{u} \quad (6.4)$$

The terms $\rho \vec{g}$ and $\rho(\vec{g} \cdot \vec{u})$ in Eq. (6.2) and Eq. (6.3) refer to gravitational force per unit volume and rate of change of energy per unit volume when the material is also subjected to gravitational field.

6.2.2 Lagrangian scheme

In Lagrangian scheme, we observe material motion from a reference frame moving with the local velocity of the fluid with time [126, 128, 129]. There is no net flow in to a volume element as the frame is also moving and so the mass of the element remains constant. So the time rate of change of any state

variable is the total derivative. The Lagrangian conservation equations are:

$$\frac{d\rho}{dt} = -\rho(\vec{\nabla} \cdot \vec{u}) \quad (6.5)$$

$$\rho \frac{d\vec{u}}{dt} = -\vec{\nabla} P + \rho \vec{g} \quad (6.6)$$

$$\rho \frac{dE}{dt} = -P(\vec{\nabla} \cdot \vec{u}) + \rho \vec{g} \cdot \vec{u} \quad (6.7)$$

The total or material derivative of any variable $\phi(\vec{r}, t)$ is given by

$$\frac{d\phi}{dt} = \left(\frac{\partial \phi}{\partial t} \right) + \vec{u} \cdot \vec{\nabla} \phi \quad (6.8)$$

It is easy to transform the conservation equations from one scheme to the other using Eq. (6.8). The conservation equations are coupled non-linear partial differential equations and hence can not be solved analytically. Therefore, numerical techniques are commonly used for obtaining the space time profiles of fluid variables.

6.3 FCT Numerical Algorithm

In the present study we have employed the one dimensional Flux-Corrected Transport (FCT) algorithm to solve the system of coupled conservation equations rather than the conventional finite difference approximation [130]. The FCT algorithm, developed by Boris and Book [131–133] and Book *et al* [134], is a second order with respect to time step. Also, it is monotone, conservative and positivity preserving algorithm. Therefore it resolves steep gradients accurately in simulation of shocks. The positivity property is one of the important characteristics in fluid flow simulations. The monotonic feature avoids the generation of maximum or minimum in the spatial profiles due to numerical approximation of convection terms.

The FCT algorithm solves a generalized one-dimensional continuity equation, which is expressed as:

$$\frac{\partial G}{\partial t} + \frac{1}{r^{a-1}} \frac{\partial}{\partial r} (r^{a-1} G u) + \frac{1}{r^{a-1}} \frac{\partial}{\partial r} (r^{a-1} B) - C \frac{\partial D}{\partial r} - f = 0 \quad (6.9)$$

Table 6.1: Source terms in generalized continuity equation

<i>Equation</i>	G	B	C	D	f
Mass density	ρ	0	0	0	0
Momentum density	ρu	0	-1	P	0
Energy density	ρE_t	Pu	0	0	source power

Here, G is the generalized density such as mass density, momentum density or energy density. The spatial coordinate in one dimension is r and u represents the velocity along the coordinate. The Euler equations (Eqs. (6.1), (6.2), and (6.3)) specialized to the three geometries (planar, cylindrical and spherical) in one dimension can be expressed as the general continuity equation given above. The parameter a specifies the different geometries; i.e., $a = 1$ for Cartesian or planar geometry, $a = 2$ for cylindrical geometry, and $a = 3$ for spherical geometry. The source terms B, C, D and f , which are functions of r and t , take the values given in Table 6.1 for the three equations. Thus solving the coupled conservation equations amounts to solving Eq. (6.9) with specified values of the source terms.

Any numerical approximation should preserve positivity property of the fluid density. For example, if density is positive everywhere, and there are no sources or sinks, then it is a mathematical property of the conservation equation that density remains positive everywhere for all times. If this property is to be incorporated in difference schemes, then numerical approximations to convection process through the meshes generate certain amount of (numerical) material diffusion. This arises from the requirement of stability of the numerical schemes (like Courant's condition) and the positivity condition. Numerical diffusion leads to smearing of the density variable in a whole mesh, while the fluid could have just entered the mesh from its boundary. However, remedying numerical diffusion totally leads to occurrence of unphysical overshoots in the fluid properties thereby destroying monotonic behavior. This necessitates addition some diffusion so that monotonicity is not violated. The FCT algorithm accommodates minimum numerical diffusion so as to preserve monotone, conservative and positivity properties [131–133].

6.3.1 Flux correction scheme

The FCT algorithm mainly consists of two stages: a convective stage followed by an anti-diffusive stage. The convective stage involves updating the density profiles using a general three point spatial difference scheme. Net fluid flow into the mesh and some amount of diffusive transport are present in this stage so that numerical stability and positivity are preserved. But the addition of diffusion terms produces unphysical overshoots. This is, then, minimized by varying the diffusion coefficient over the meshes in such a way to suppress overshoots. However, the penalty of this process is the generation of strong numerical diffusion. To reduce the latter effect, the FCT algorithm introduces a correction to the density profile by adding anti-diffusion terms. The fluxes in the anti-diffusive stage are limited, or restricted, in such a way that no new overshoots are produced. This method of correcting the density profile obtained in the first convective stage is the basic idea of flux correction scheme. Concise discussion of these ideas are provided by Boris *et al* [127]

6.3.2 Two stage time integration

Accuracy of the time integration is improved in the FCT algorithm by using a two-step scheme. New fluid variables, such as $\rho^{n+1/2}$, are computed at half time step (indicated as superscript $n + 1/2$) to get first order accurate quantities. Then the source terms $S^{n+1/2}$ in the continuity equation e.g., $P(\rho, T)$, are obtained using time centered values of variables (like $\rho^{n+1/2}$, temperature $T^{n+1/2}$, etc.). In the second step, the continuity equation is integrated, using time-centered source terms, to obtain the fluid variables at the end of the full time step. These steps are summarized as follows:

1. Compute u^n and P^n using density ρ^n , momentum density $(\rho u)^n$ and energy density $(\rho E_t)^n$ at time t_n .
2. Compute density $\rho^{n+1/2}$ for half time step using convective transport algorithm given below.
3. Evaluate source term $P^{n+1/2}$ for the momentum conservation equation.
4. Convective transport of momentum density $(\rho u)^{n+1/2}$ for half time step using source term $P^{n+1/2}$.

5. Evaluate source term $(Pu)^{n+1/2}$ for the energy conservation equation.
6. Convective transport of energy density $(\rho E_t)^{n+1/2}$ for half time step using source term $(Pu)^{n+1/2}$.

The second stage involves repeating all the six steps, mentioned above, for full time step. This method provides second order accuracy in time integration.

6.3.3 Difference equations

6.3.3.1 Mesh generation

The spatial coordinate in the problem domain is divided into N number of cells or grids. The center of i^{th} cell is denoted as r_i^q and the interfaces are located at

$$r_{i+1/2}^q = \frac{1}{2}(r_i^q + r_{i+1}^q) \quad i = 0, \dots, N \quad (6.10)$$

The superscript q denotes o or n for old and new grids at the beginning and the end of the n^{th} time step. The coordinate $r_{1/2}^q$ and $r_{N+1/2}^q$ are the first and last interfaces of the computational domain. The cells, indexed 0 and $N + 1$, are assumed to exist outside the actual problem domain. These are known as fictitious guard cells or ghost cells. The cell interface areas, which are time and space centered in Cartesian, cylindrical, and spherical geometries are

$$A_{i+1/2} = \begin{cases} 1 & \text{Cartesian} \\ \pi(r_{i+1/2}^0 + r_{i+1/2}^n) & \text{cylindrical} \\ \frac{4}{3}\pi[(r_{i+1/2}^0)^2 + r_{i+1/2}^0 r_{i+1/2}^n + (r_{i+1/2}^n)^2] & \text{spherical} \end{cases} \quad (6.11)$$

This particular averaging ensures that a constant density profile remains unaltered in a static fluid while the time variable moves the fluid into or out of the system. The corresponding volume elements are

$$\Lambda_i^\alpha = \begin{cases} (r_{i+1/2}^q - r_{i-1/2}^q) & \text{Cartesian} \\ \pi[(r_{i+1/2}^q)^2 - (r_{i-1/2}^q)^2] & \text{cylindrical} \\ \frac{4}{3}\pi[(r_{i+1/2}^q)^3 - (r_{i-1/2}^q)^3] & \text{spherical} \end{cases} \quad (6.12)$$

At initial time, the densities G_i^0 and fluid velocities u_i^0 are known at cell centers. These variables at the cell interfaces, which are needed to determine the

interface fluxes, are given by

$$G_{i+1/2}^0 = \frac{\rho_i^0 G_{i+1}^0 + \rho_{i+1}^0 G_i^0}{\rho_i^0 + \rho_{i+1}^0} \quad (6.13)$$

$$u_{i+1/2}^0 = \frac{\rho_i^0 u_{i+1}^0 + \rho_{i+1}^0 u_i^0}{\rho_i^0 + \rho_{i+1}^0} \quad i = 1, \dots, N-1 \quad (6.14)$$

The quantities are averaged using density weighting factor. Although there are other choices to compute interface averages, we have considered Eq. (6.13) and Eq. (6.14) in our calculations.

6.3.3.2 Discrete approximations to continuity equation

The generalized density G_i^n is computed from the following difference equations

$$\Lambda_i^n G_i^n = A_i^T + A_i^S + A_i^D + A_i^C \quad (6.15)$$

where A_i^T , A_i^S and A_i^D denote the convective transport term, source term, numerical diffusion term. These cover the first stage mentioned above. A_i^C is the anti-diffusive flux correction term of second stage. These are expressed in terms of the fluid variables as follows:

$$A_i^T = \Lambda_i^0 G_i^0 + \Delta t (A_{i-1/2} G_{i-1/2}^0 u_{i-1/2}^{n+1/2} - A_{i+1/2} G_{i+1/2}^0 u_{i+1/2}^{n+1/2}) \quad (6.16)$$

$$A_i^S = \Delta t (A_{i+1/2} B_{i+1/2} - A_{i-1/2} B_{i-1/2}) + \frac{\Delta t}{2} C_i (A_{i+1/2} + A_{i-1/2}) (D_{i+1/2} - D_{i-1/2}) + \Delta t \Lambda_i^0 f_i \quad (6.17)$$

$$A_i^D = \nu_{i+1/2} \Lambda_{i+1/2}^n (G_{i+1}^0 - G_i^0) - \nu_{i-1/2} \Lambda_{i-1/2}^n (G_i^0 - G_{i-1}^0) \quad (6.18)$$

$$A_i^C = -(F_{i+1/2}^C - F_{i-1/2}^C) \quad i = 1, \dots, N \quad (6.19)$$

Here, the fluid velocity $u_{i+1/2}^{n+1/2}$ appearing in A_i^T is computed for half time step. The source terms C_i are computed in the cell centers, whereas, other source terms $B_{i+1/2}$, $B_{i-1/2}$, $D_{i+1/2}$, $D_{i-1/2}$ are computed at the interfaces. The input power term f_i are also defined at cell centers. All these variables correspond to half time step. The interface volumes, including those of boundaries, are

defined as

$$\Lambda_{i+1/2}^n = \frac{1}{2}(\Lambda_{i+1}^n + \Lambda_i^n) \quad i = 1, \dots, N-1 \quad (6.20)$$

$$\Lambda_{1/2}^n = \Lambda_1^n, \quad \Lambda_{N+1/2}^n = \Lambda_N^n \quad (6.21)$$

The FCT algorithm incorporates change in cell volume because of moving grids as in Lagrangian method. This is accounted in the diffusion stage given in Eqs. (6.18) and (6.22). The diffusion coefficient and corrected anti-diffusive fluxes are given by

$$\nu_{i+1/2} = \frac{1}{3} \left(\frac{1}{2} + \left[A_{i+1/2} u_{i+1/2}^{n+1/2} \frac{\Delta t}{2} \left(\frac{1}{\Lambda_{i+1}^n} + \frac{1}{\Lambda_i^n} \right) \right]^2 \right) \quad i = 0, \dots, N \quad (6.22)$$

$$F_{i+1/2}^C = \text{Sg Max}\{0, \text{Min}[|F_{i+1/2}|, \text{Sg } \Lambda_{i+1}^n (G_{i+2}^D - G_{i+1}^D) \text{Sg } \Lambda_i^n (G_i^D - G_{i-1}^D)]\} \\ \text{for } i = 1, \dots, N-1 \quad (6.23)$$

where $\text{Sg} = \text{sign}\{G_{i+1}^D - G_i^D\}$. The uncorrected anti-diffusive flux $F_{i+1/2}$, appearing in Eq. (6.23), is given by

$$F_{i+1/2} = \mu_{i+1/2} \Lambda_{i+1/2}^n (G_{i+1}^T - G_i^T) \quad i = 0, \dots, N \quad (6.24)$$

where $\mu_{i+1/2}$ is the anti-diffusion coefficient expressed as:

$$\mu_{i+1/2} = \frac{1}{3} \left(\frac{1}{2} - \left[A_{i+1/2} u_{i+1/2}^{n+1/2} \frac{\Delta t}{2} \left(\frac{1}{\Lambda_{i+1}^n} + \frac{1}{\Lambda_i^n} \right) \right]^2 \right) \quad i = 0, \dots, N \quad (6.25)$$

Finally, terms like G_i^D and G_i^T occurring in Eqs. (6.23) and (6.24) are given by

$$\Lambda_i^0 G_i^T = A_i^T + A_i^S; \quad \Lambda_i^n G_i^D = \Lambda_i^0 G_i^T + A_i^D \quad (6.26)$$

The numerical scheme outlined above, i.e. in Eq. (6.15) to Eq. (6.25), provides generalized density G_i^n uniquely, provided EOS of a material in the form $P(\rho, E)$ is known.

6.3.4 Boundary conditions

Different types of boundary conditions are needed to specify the behavior of fluid variables at boundaries depending on the physics of the problem. Oran and Boris [135] have described three methods to implement boundary conditions in computational scheme. These are

- If the fluid variables can be expressed as a linear superposition of expansion functions with boundary conditions built into each of them, such combinations automatically satisfy boundary conditions.
- One can derive finite difference formulas for guard cell variables from analytic formulas used in the interior for state variables, in addition with other auxiliary relations. For many practical problems analytical formulation is not possible.
- The boundary cell values can be obtained by extrapolating the value of fluid variables from interior mesh.

The third method, defining guard cell values from extrapolation, is easy and is therefore adopted in FCT algorithm. This approach updates the guard cell values with time step, depending upon the fluid variables in the interior mesh. The following boundary conditions are employed in the FCT algorithm:

$$G_0^n = S_{bc1}G_1^n + V_{bc1} \quad (6.27)$$

$$G_{N+1}^n = S_{bcN}G_N^n + V_{bcN} \quad (6.28)$$

where G_0^n and G_{N+1}^n are the generalized density in guard cells at time step n , while G_1^n and G_N^n are the same in the first cell and the last cell, respectively. The parameters S_{bc1} and S_{bcN} are slope multiplicative factors, while V_{bc1} and V_{bcN} are added constants specified by user. For modeling plate impact experiments, we have used free and rigid types of conditions at the boundary:

6.3.4.1 Free boundary

$$\text{Left: } u_{1/2}^n = u_1^n; \quad P_{1/2}^n = 1 \text{ bar}; \quad V_{bc1} = 0; \quad S_{bc1} = 0 \quad (\text{for } \rho, \rho u \text{ and } \rho E_t)$$

$$\text{Right: } u_{N+1/2}^n = u_N^n; \quad P_{N+1/2}^n = 1 \text{ bar}; \quad V_{bcN} = 0; \quad S_{bcN} = 0 \quad (\text{for } \rho, \rho u \text{ and } \rho E_t)$$

6.3.4.2 Rigid boundary

Left: $u_{1/2}^n = 0$; $P_{1/2}^n = -P_1^n$; $V_{bc1} = 0$; $S_{bc1} = 1$; (for $\rho, \rho E_t$) and
 $S_{bc1} = -1$ (for ρu)

Right: $u_{N+1/2}^n = 0$; $P_{N+1/2}^n = -P_N^n$; $V_{bcN} = 0$; $S_{bcN} = 1$; (for $\rho, \rho E_t$) and
 $S_{bcN} = -1$ (for ρu)

The FCT algorithm described are coded as FORTRAN subroutines [127] and are distributed freely by its authors. Users have to code only a driver program and provide EOS packages to use these subroutines. Accurate one and two dimensional simulations have already been reported using the FCT package [136–138].

6.4 Equation of state

A hydrodynamic sweep using the FCT algorithm needs pressure profiles (P), which is to be obtained from the current profiles of density (ρ) and specific internal energy (E). We have used the Mie-Grüneisen EOS and Enthalpy-based EOS, which are briefly discussed below.

6.4.1 Mie-Grüneisen EOS

Once ρ and E are available in a particular mesh and time, then pressure (P) is given by:

$$P = P_h(\rho) + \Gamma(\rho)\rho(E - E_h) \quad (6.29)$$

Here, $P_h(\rho)$ and $E_h(\rho)$ are, respectively, pressure and specific internal energy along the Hugoniot of solid. $\Gamma(\rho)$ is the Grüneisen-parameter which is specified a priori for the material. One of the common forms in use is $\Gamma(\rho) = \Gamma_0 (\rho_0/\rho)$ where the subscript 0 refers to parameter values at normal conditions, however, there are also more accurate formulations [7] discussed earlier in chapter 2. The second term in Eq. (6.29) accounts for thermal contribution to pressure over and above that corresponding to the solid Hugoniot. Shock wave experiments measure the parameters C and S in the shock speed (U_s)

vs. particle speed (U_p) linear relation, viz. $U_s = C + S U_p$. Combining it with the Rankine-Hugoniot relations, $P = \rho_0 U_s U_p$ and $\rho_0 U_s = \rho(U_s - U_p)$ yields the expressions:

$$P_h = C^2 \frac{\rho_0 \rho (\rho - \rho_0)}{[\rho - S(\rho - \rho_0)]^2} \quad (6.30)$$

$$E_h = \frac{1}{2} (P_h + P_0) (1/\rho_0 - 1/\rho) \quad (6.31)$$

The parameter C is same as adiabatic sound speed - $\rho_0 C^2$ is bulk modulus B_0 - while S is related to pressure derivative of bulk modulus as $B'_0 = 4S - 1$. It is easy to generate pressure profiles at the end of a time step as ρ and E get updated during the hydrodynamic cycle. For $\rho < \rho_0$, pressure is given by

$$P = C^2 (\rho - \rho_0) + \Gamma_0 \rho_0 E \quad (6.32)$$

which follows by expanding $P(\rho, E)$ to lowest order around ρ_0 and $E = 0$. It is also of the Mie-Grüneisen form if we take the first term as approximating zero temperature pressure P_c and $E_c = 0$.

6.4.2 Enthalpy-based EOS

We have already pointed out in previous chapters that porous materials differ from normal solids due to their low initial density ρ_{00} . It is more appropriate to describe these materials by keeping pressure (P) and temperature (T) as independent variables. This allows to incorporate the compaction phase (i.e., $\rho_{00} \leq \rho \leq \rho_0$) of the porous material properly. Similarly, faster equilibration of pressure in mixtures, as discussed in earlier chapters, makes it necessary to consider pressure as independent variable. The enthalpy-based EOS described in second chapter is expressed as

$$V = V'_c + \frac{\chi}{P} (H - H'_c) \quad (6.33)$$

where H is the total specific enthalpy, H'_c is the specific enthalpy on zero-temperature isotherm, V'_c is the volume on zero temperature isotherm and χ is the effective enthalpy parameter, which includes electronic effects. We have already explained the use of (Carroll and Holt) P - α model for obtaining V'_c from

the volume V_c on the zero temperature isotherm. An adequate expression for zero temperature isotherm is [139]

$$P_c = \frac{B_0}{B'_0 + 1} \left(\exp[(1 - V/V_0)(B'_0 + 1)] - 1 \right) \quad (6.34)$$

which is readily inverted for a specified pressure to obtain V_c i.e.

$$V_c = V_0 \left(1 - \frac{1}{B'_0 + 1} \log[1 + (B'_0 + 1)P/B_0] \right) \quad (6.35)$$

Note that B_0 and B'_0 are, respectively, the bulk modulus and its pressure derivative at volume V_0 . The Carroll-Holt factor $\alpha(P)$, then, gives $V'_c = \alpha(P)V_c$.

We can apply Eq. (6.33) to express volume along the solid Hugoniot as well:

$$V_h = V_c + \frac{\chi}{P}(H_h - H_c) \quad (6.36)$$

Note that V_c and H_c are used in lieu of V'_c and H'_c in this expression. Subtracting Eq. (6.36) from Eq. (6.33) and expressing enthalpies as $H=E+PV$, we obtain

$$V = V_h + (V'_c - V_c) + \frac{\chi}{1 - \chi} \frac{1}{P}(E - E_h) \quad (6.37)$$

For a specified value of P , Eq. (6.30) is inverted to obtain V_h as

$$V_h = V_0 - V_0 \frac{\beta(P)}{S} [1 - \sqrt{1 - \beta^{(-2)}}]; \quad \beta(P) = 1 + \frac{C^2}{2SV_0P} \quad (6.38)$$

Then Eq. (6.31) readily gives E_h . Thus, Eq. (6.37) can be used to obtain the volume if the enthalpy parameter χ is known. For numerical studies done in this paper, we determine it along the solid Hugoniot [66, 68]. The definition, $\chi/P = (\partial V / \partial H)_T$, yields the expression

$$\chi(P) = \Gamma \frac{P}{K_s} \quad (6.39)$$

where K_s is the bulk modulus along an isentrope passing through the point (P, V) . Since V_h is known, $\Gamma(V_h)$ is also known along the Hugoniot. We use the

thermodynamic relation

$$K_s(P) = \frac{\Gamma P}{2} - \frac{dP_h}{dV} \left(V - \frac{\Gamma}{2}(V_0 - V) \right) \quad (6.40)$$

to obtain K_s along the Hugoniot. Note that (dP_h/dV) here is the local slope along the Hugoniot, and Eq. (6.30) yields the expression

$$\frac{dP_h}{dV} = -C^2 \frac{[V_0(1+S) - SV]}{[V_0(1-S) + SV]^3} \quad (6.41)$$

The EOS formulation outlined above provides V for a specified value of pressure P and internal energy E . Pressure P in the current time step is then obtained by inverting Eq. (6.37) using the root finding method. Compaction and compression of materials with high degree of porosity can be simulated using the enthalpy-based EOS. When material expands and $\rho < \rho_0$, *after attaining normal density ρ_0 via compaction*, we use $P=C^2(\rho-\rho_0) + \Gamma_0\rho_0E$ as discussed earlier.

6.4.3 Explicit accounting of electronic effects

We have used effective enthalpy parameter in Eq. (6.33), which contains electronic effects also. However, as shown in earlier chapters, electronic effects could be incorporated explicitly. For that purpose, Eq. (6.33) is generalized as

$$V = V'_c + \frac{\chi}{P}(H - H'_c) + (\chi_e - \chi_i) \frac{1}{P} \left(w_i H_{te}(P, T) - w_e H_{ti}(P, T) \right) \quad (6.42)$$

where χ is the effective enthalpy parameter defined as $\chi = w_i \chi_i + w_e \chi_e$, while χ_i and χ_e denote ionic and electronic enthalpy parameters, respectively. The weigh factors are $w_i=C_{P_i}/C_P$ and $w_e=C_{P_e}/C_P$ where C_{P_i} and C_{P_e} are ionic and electronic specific heats, and $C_P=C_{P_i}+C_{P_e}$. Now, in lieu of Eq. (6.37), we have the generalized expression:

$$V = V'_c + \frac{\chi}{1-\chi} \frac{1}{P}(E - E_c) + \frac{\chi_e - \chi_i}{1-\chi} \frac{1}{P} \left(w_i H_{te}(P, T) - w_e H_{ti}(P, T) \right) \quad (6.43)$$

Methods for computing the specific heats, enthalpy parameters and thermal enthalpies (H_{ti} and H_{te}) are already discussed in second and fifth chapters. However, it is necessary to know temperature T to use of Eq. (6.43). At the end of a hydrodynamic step, $\Delta Q=\Delta E+P\Delta V$, where Δ denotes the incremental

Table 6.2: Impact experiments on solid Cu

Experiment	Cu-target thickness (mm)	Cu-impactor thickness (mm)	Impactor velocity (km/s)
1	18.24	2.946	0.285
2	18.23	2.865	0.468
3	18.38	2.934	0.645

Table 6.3: Material Parameters for Cu.

Material	ρ_0 g/cm ³	B_0 GPa	B'_0	Γ_0	C_V J/g K	C km/s	S
Copper	8.93	1.348	5.193	2.0	0.385	4.14	1.408

change during the time step, is known. The corresponding updated temperature T is then obtained as

$$\bar{C}_V(T - T_p) + \frac{\bar{\Gamma}}{\bar{V}}(T + T_p)\frac{\Delta V}{2} = \Delta Q \quad (6.44)$$

where T_p is the temperature in the previous time step. Other quantities \bar{C}_V , $\bar{\Gamma}$ and \bar{V} denote averages of initial and final variable values. So Eq. (6.44) may have to be iterated one or two times.

6.5 Simulation of impact experiments

In impact experiments a projectile (impactor) impacts a target (plate) and launches a shock wave. In fact two waves are formed at the interface of plate and impactor, one moves to the target and the other travels back to the projectile [140]. As a result, fluid particles in the target get accelerated and finally attain a constant velocity, known as particle velocity U_p . The shock wave moves in the target with its own speed called shock velocity U_s . Shock wave experiments usually measure U_p and U_s , and obtains the entire Hugoniot data from a series of impact experiments. Other experiments measure pressure-time profile

inside some point in the target. Yet others measure the release velocity-time profile when shock breaks out at the rear surface of the target.

6.5.1 Soild Cu experiment

First of all we consider three impact experiments on solid Cu using Cu impactors where the pressure-time profiles are measured at the center of the target. Experimental data used in the simulations are given in Table 6.2. Material constants for Cu used in the EOS model are summarized in Table 6.3. The simulation consisted of putting the target plate adjacent to the impactor, and specifying the impact velocity in all the mesh-interfaces within the impactor. This is shown schematically in Fig. 6.1. The Mie-Grüneisen EOS is used for this simulation. The resulting hydrodynamic motion is followed and the pressure-time profiles is obtained at the center of the target. The results for three impact velocities, compared with experimental data [10] in Fig. 6.2, show good agreement. Experimental pressure profiles were obtained using impedance matching technique [141]. Initial pressure rise, peak pressure and shock duration are accurately modeled in the simulation, although slight differences are noted between the profiles towards the end. This discrepancy could be due to the omission of strength effects in the EOS models.

We repeated these calculations using the enthalpy-based EOS and the root finding method. The results are practically indistinguishable from those obtained with Mie-Grüneisen EOS.

6.5.2 Shock propagation in Soild Cu

Next we investigate shock wave attenuation in a set of *simulations using the enthalpy-based EOS*. This is motivated by the routine use of porous materials for protection from shocks. First simulation consisted of using 20 mm thick solid Cu target, impacted with 3 mm thick Cu impactor with a velocity of 2 km/s. This leads to a fluid velocity of 1 km/s in the target because of the inelastic collision between impactor and target. The hydrodynamic motion is followed numerically and pressure-time profiles at different distances (3 mm to 15 mm) from the target surface are recorded. The results shown in Fig. 6.3

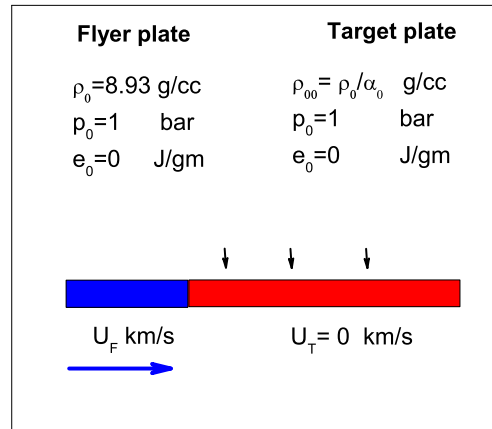


Figure 6.1: Simulation geometry for plate impact problems. Thicknesses of impactor and target plates are 3 mm and 20 mm, respectively, for shock attenuation calculations.

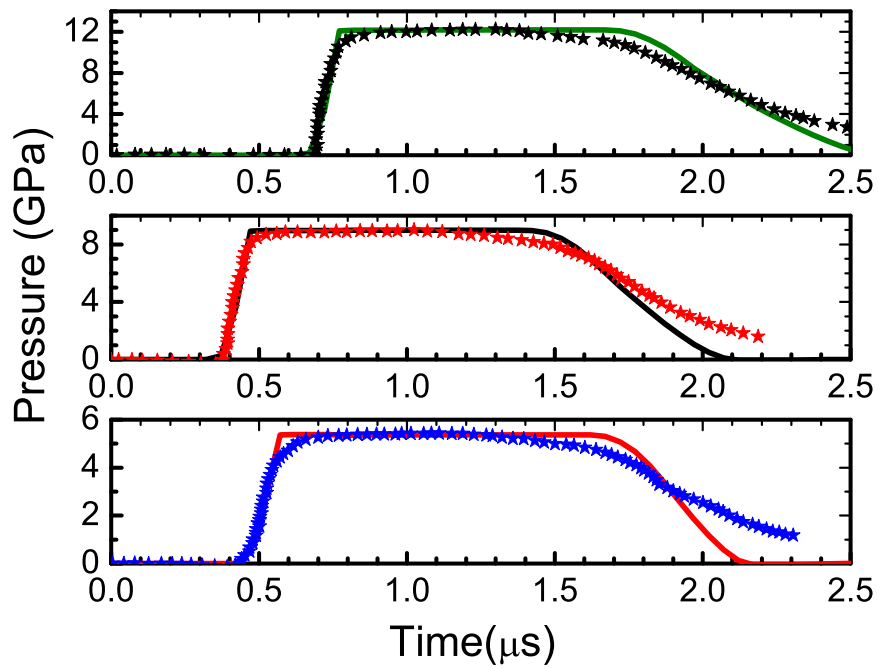


Figure 6.2: Pressure-time profiles: Solid lines are simulation results while symbols denote experimental data [10]. (Top) Impact velocity 0.645 km/s, (middle) Impact velocity 0.468 km/s, (bottom) Impact velocity 0.285 km/s

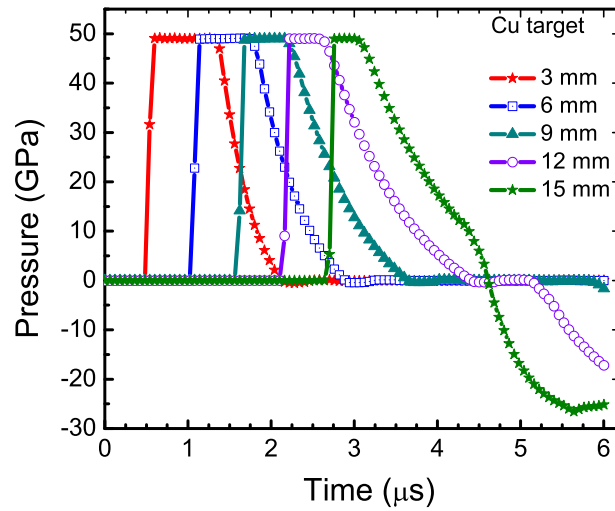


Figure 6.3: Attenuation of shock wave in solid-Cu of 20 mm thickness, impacted with 3 mm thick impactor with velocity 2 km/s. Pressure-time profiles are shown at different locations (see legend) from the impact surface. Note that the peak pressure remains unaltered even up to 15 mm. Negative pressure occur in the last two profiles because of the release wave reaching back from the rear surface.

are almost identical with *Mie-Griineisen EOS and enthalpy-based EOS*. Note that the peak pressure of ~ 49 GPa remains unaltered even up to 15 mm. The pressure pulses show a shock speed of about 5.5 km/s which agrees very well from that obtained from the relation $U_s = 4.14 + 1.408U_p$. Shock pressure computed as $P = \rho_0 U_s U_p$ also agree with the simulation result. This agreement shows the consistency of the simulation. Negative pressure occur in the last two profiles because of the release wave reaching back from the rear surface.

6.5.3 Shock attenuation in Cu with 1.1 porosity

We repeated the simulation with Cu with porosity 1.1 using enthalpy-based EOS. The pressure-time profiles at different locations given in Fig. 6.4 clearly show that shock attenuates even at this low porosity. Now, the maximum pressure reached in the target is reduced to about 43 GPa. Further, the peak pressure attenuates after the shock travels about 13 mm, and the shock velocity is lower compared to that in solid target. The profiles show that shock speed is reduced to 4.8 km/s compared to 5.5 km/s in solid target. Negative pressure occur only in the last profile because of the release wave reaching back from the rear surface is delayed.

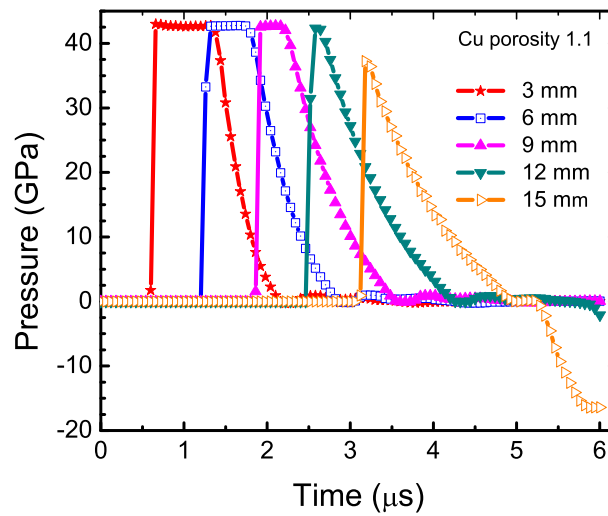


Figure 6.4: Attenuation of shock wave in porous-Cu of 20 mm thickness (porosity 1.1), impacted with 3 mm thick impactor with velocity 2 km/s. Pressure-time profiles are shown at different locations (see legend) from the impact surface. Note that the peak pressure attenuates after the shock travels about 13 mm, and the shock velocity is lower compared to that in solid target. Negative pressure occur in the last profile because of the release wave reaching back from the rear surface.

6.5.4 Shock attenuation in Cu with 1.3 porosity

The simulation discussed above for Cu is again repeated with porosity 1.3. Here also we use the enthalpy-based EOS. The pressure-time profiles at different locations are given in Fig. 6.5, which clearly demonstrate significant attenuation of the shock. Now, the maximum pressure reached in the target is only about 34 GPa and the peak pressure begins to decrease after the shock travels about 7 mm. In fact its value becomes negligible after about 15 mm. The shock velocity is reduced significantly to 3.7 km/s. Negative pressures are not visible at all because the shock wave and consequently the release wave are sufficiently delayed.

6.5.5 Shock pressure vs. fluid speed

As a final check on the simulation package, we repeated the calculations for different impact velocities (up to about 7 km/s) for each of three porosities (1, 1.13 and 1.414) using the enthalpy-based EOS. Maximum shock pressure and fluid speed obtained in the target in each simulation are then recorded. These

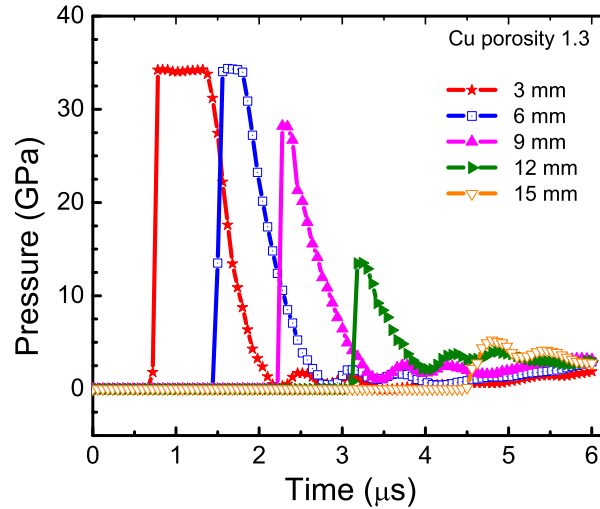


Figure 6.5: Attenuation of shock wave in porous-Cu of 20 mm thickness (porosity 1.3), impacted with 3 mm thick impactor with velocity 2 km/s. Pressure-time profiles are shown at different locations (see legend) from the impact surface. Note that the peak pressure starts to attenuate after the shock travels about 7 mm, and the shock velocity is lower compared to that for porosity 1.1. Negative pressures are not visible because the shock wave and consequently the release wave are delayed.

numerical results are compared with experimental data in Fig. 6.6 [4]. The excellent agreement we have obtained demonstrate the the accuracy of FCT algorithm and enthalpy-based EOS formulation.

6.6 Summary

We have implemented a numerical simulation package for solving one dimensional hydrodynamics equations using the well known FCT algorithm. This scheme was preferred one over the standard finite-difference method because of its second order accuracy, monotone, conservative and positivity preserving properties. We have also implemented the enthalpy-based EOS for simulation of porous materials. As volume is expressed in terms of pressure and energy in this EOS, a root finding algorithm is used to couple it with hydrodynamic cycles. Few simple plate impact simulations have been done to demonstrate the simulation package.

It is important to stress that the enthalpy-based EOS needs only few experi-

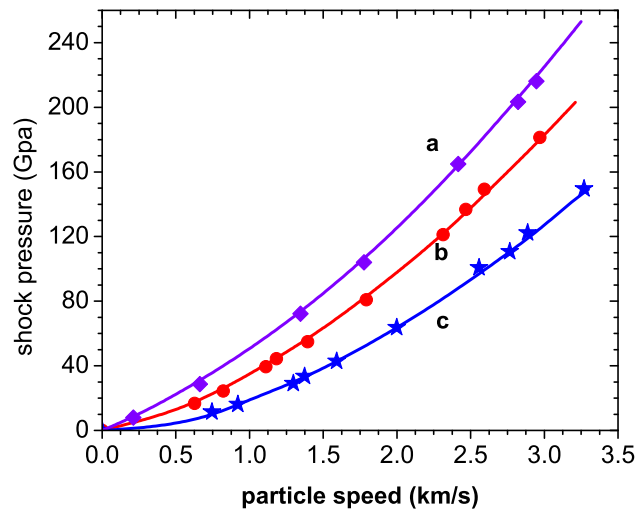


Figure 6.6: Shock pressure vs. fluid speed in Cu. (a) normal solid, (b) porosity 1.13 and (c) porosity 1.414. Lines denote computed results while the symbols are experimental data [4].

mentally measured properties (like density, bulk modules, shock parameters, etc.) of the the *solid at ambient conditions*. Therefore hydrodynamic simulations using this EOS can be used to predict the behavior of porous materials. For example, we have obtained pressure vs. fluid speed curves for three porosities in Cu and compared the results with experimental data. These calculations need to be extended to higher porosities. Another application would be the comparison of time profiles of shock break out velocity. Effect of convergent geometry on compaction and compression of porous materials need to be investigated. Such applications are currently under way and will be reported in future.

Conclusions and future work

7.1 Concluding remarks

The main focus of the research was the development of EOS models for porous materials and application of these models to study shock wave propagation in distended solids. In chapter 1, motivation, background, objective of our study and brief description of research work were discussed.

In chapter 2, a generalized enthalpy-based EOS model, including thermal contribution of electrons, from thermodynamic definitions was developed. The Hugoniot relation across shock front with new EOS and equation for temperature along Hugoniot were solved simultaneously to calculate P-V curve and the corresponding temperature for porous copper at different initial densities. Our model has shown significant difference in Hugoniot data with and without electronic contribution for Cu when $\alpha_0 \geq 2$. The results obtained from our model follow the experimental data. Also, the errors present in earlier attempts, in deriving enthalpy-based EOS with electronic contribution, were brought out.

In chapter 3, we have developed an EOS model for binary mixtures by incorporating proper averaging of zero temperature isotherm and ionic enthalpy parameters for individual components. Although the model assumes equilibrium pressure and material velocity but non-equilibrium thermal effects were added to determine Hugoniot parameters. The extra term in the present model, which arises because of difference in ionic specific enthalpies of individual components of the mixture, could become important in other applications such as shock induced chemical reactions, structural phase transitions, dissociations etc. The binary mixture EOS was applied to various mixtures, including one porous case, and the results agree well with experimental data.

The treatment of porous binary mixtures within the enthalpy-based EOS was done for the *first time*. Also, single component criteria for each component was invoked for the *first time* to obtain non-equilibrium temperatures in binary mixtures.

An EOS model for multi-component mixtures, employing enthalpy-based approach, was proposed in chapter 4. The model was applied to epoxy based composites (with $\sim 15\%$ porosity), where non-equilibrium temperatures of each component were computed using single component criteria, to calculate Hugoniot data. Also the ionic specific enthalpy difference term is important in multi-component mixtures as observed in P-V curve of epoxy based two and three component mixtures. The P vs. U_p and U_s vs. U_p data obtained from our model were consistent with existing experimental data.

In chapter 5, a modified soft sphere model for fluid phase was developed to apply generalized enthalpy-based EOS to higher porosities ($\alpha_0 \geq 3$) when the compressed volume is higher than initial volume V_0 . The liquid-vapor co-existence curve of copper obtained from the model agreed with those from detailed molecular dynamics simulations. Also, we have modeled the effect of energy loss from shock, which occurs due to expansion of the shocked vapor, as a PdV term. The new model was applied to Cu as prototype and accurate results were obtained in a wide range of porosity i.e. from $\alpha_0=2$ to 10. Our approach used accurate models corresponding to fluid phase, and incorporated energy loss due to vapor expansion in a general way (PdV work) for the *first time*.

We have studied shock wave propagation in materials, via numerical simulations of the Euler equations describing conservation laws of mass, momentum and energy. Here the FCT algorithm (which is monotone, conservative, positivity preserving algorithm, and also accurate up to 2nd order with time step) was used in Lagrangian approach to solve system of coupled non-linear conservation equations rather than the conventional finite difference approximation. The algorithm has two stages: a convective stage followed by an anti-diffusive stage. We have simulated impact experiments employing Mie-Gruneisen EOS for normal solid and enthalpy-based EOS for porous sub-

stances. Initial pressure rise, peak pressure and shock duration are accurately modeled in the simulation. The simulation results compared well with analytical estimates. The peak pressure and shock velocity attenuate fast, e.g. porous Cu with low porosity i.e. 1.1 and 1.3, which is consistent with the theory.

7.2 Future scope

There are several problems in the domain of shock wave propagation in porous materials which are to be investigated in more detail using the enthalpy-based EOS. Some of these problems can be briefly as:

- Development of enthalpy-based EOS model for multifunctional energetic materials, e.g. Ni+Al, Ni+Ti mixtures, incorporating the effect of shock induced chemical reactions.
- Treatment of shock and temperature induced transitions like structural phase transitions, molecular dissociation, etc.
- Application to detonation phenomena, which involves shock propagation in multi-component mixtures at high temperatures.
- Comparison of Mie-Grüneisen and enthalpy-based EOS simulations of highly porous materials (using simulation results).
- Numerical simulations to predict shock wave properties and further comparisons with experimental data (e.g. release wave).
- Numerical simulations to include geometric convergence effects in shock propagation in porous materials (as occurring in spherical and cylindrical geometries).

We hope to investigate these research problems as follow up of the work discussed in the thesis.

Bibliography

- [1] STEFAN JOSEF HIERMAIER. *Structures Under Crash and Impact: Continuum Mechanics, Discretization and Experimental Characterization* (Springer, 2008).
- [2] BOEY CHUNG WAI. *Investigation of shock wave attenuation in porous materials: thesis* (2009).
- [3] <http://www.ihed.ras.ru/rusbank/>.
- [4] S.P. MARSH. *LASL Shock Hugoniot Data*. (University of California Press, California, 1980).
- [5] A.V. BUSHMAN, I.V. LOMONOSOV AND K. V. KHISHCHENKO. *Shock wave data base*. (<http://teos.ficp.ac.ru/rusbank>, 2004).
- [6] B. NAYAK AND S.V.G. MENON. "Explicit accounting of electronic effects on the Hugoniot of porous materials." *J. Appl. Phys.*, **119**(12), 125901–125907 (2016).
- [7] L. BURAKOVSKY, D.L. PRESTON. "Analytic model of the Gruneisen parameter for all densities". *Journal of Physics and Chemistry of Solids*, **65**(8-9), 1581–1587 (2004).
- [8] J.H. LI, S.H. LIANG, H.B. GUO, B.X. LIU. *Journal of Alloys and Compounds*, **431**, 23 (2007).
- [9] SAI VENKATA RAMANA A. *Fluid Phase Equilibria*, **361**, 181 (2014).
- [10] ED. C.E. MORRIS. *LOS ALAMOS SHOCK WAVE PROFILE DATA* (University of California Press, Ltd. London, England, 1982).
- [11] W. HERMANN. *J. Appl. Phys.*, **40**, 2490 (1969).
- [12] M.M. CARROLL AND A.C. HOLT. "Static and dynamic pore-collapse relations for ductile porous materials." *J. Appl. Phys.*, **43**(4), 1626–1636 (1972).
- [13] B.M. BUTCHER AND C.H. KARNES. *J. Appl. Phys.*, **40**, 2967–2976 (1969).
- [14] R.R. BOADE. *J. Appl. Phys.*, **41**, 4542–4551 (1970).

- [15] M.R. BAER. *J. Appl. Mech.*, **55**, 36–43 (1988).
- [16] L.S. BENNETT, Y. HORIE, AND M.M. HWANG. *J. Appl. Phys.*, **76**, 3394–3402 (1994).
- [17] D.S. STEWART, B.W. ASAY, AND K. PRASAD. *Phys. Fluids*, **6**, 2515–2534 (1994).
- [18] W.H. GOURDIN. *Prog. Mater. Sci.*, **30**, 39–80 (1986).
- [19] N.N. THADHANI. *Prog. Mater. Sci.*, **37**, 117–226 (1993).
- [20] K. KITAGAWA, ET AL. “Attenuation Properties of Blast Wave Through Porous Layer”. *Shock Waves, 26th International Symposium on Shock Waves, Vol-1*, 73–78 (2009).
- [21] R.L. WILLIAMSON. *J. Appl. Phys.*, **68**, 1287–1296 (1990).
- [22] W. TONG AND G. RAVICHANDRAN. *J. Appl. Phys.*, **74**, 2425–2435 (1993).
- [23] YA.B. ZEL’OVICH AND YU. P. RAIZER. *Physics of Shock Waves and High-Temperature Hydrodynamic Phenomena*, vol. Vol-II (Academic press, New York and London, 1967).
- [24] V.N. ZHARKOV AND V. A. KALININ. *Equations of State for Solids at High Pressures and Temperatures* (Consultants Bureau, New York, 1971).
- [25] CHARLES KITTEL. *Introduction to Solid State Physics* (John Wiley & Sons, Inc., New York, 7th Edition, 1995).
- [26] FUYUKI SHIMOJO, INGVAR EBBSJÖ, RAJIV K. KALIA, AIICHIRO NAKANO, JOSE P. RINO, AND PRIYA VASHISHTA. *PHYSICAL REVIEW LETTERS*, **84**, 3338–3341 (2000).
- [27] SVEN P. RUDIN, M. D. JONES, AND J. D. JOHNSON. *Joint 20 AIRAPT-43 EHPRG, June 27-July 1, Karlsruhe/Germany* (2005).
- [28] KONSTANTIN D. LITASOV, ANTON SHATSKIY, YINGWEI FEI, AKIO SUZUKI, EIJI OHTANI, AND KENICHI FUNAKOSHI. *J. Appl. Phys.*, **108**, 053513 (2010).
- [29] B. Y. THAKORE, A. Y. VAHORA, S. G. KHAMBHOLJA, N. K. BHATT AND A. R. JANI. *Journal of Physics: Conference Series*, **377**, 012064 (2012).
- [30] SAEDEH ARABZADEH, MOHAMAD REZA BENAM. *International Journal of Engineering Research and Applications (IJERA)*, **3**(4), 1604–1606 (2013).
- [31] W.H. LEE AND X.H. YAO. *Computational Materials Science*, **106**, 76–82 (2015).
- [32] ROBERT C. EHEMANN, JEREMY W. NICKLAS, HYOUNGKI PARK, AND JOHN W. WILKINS. *arXiv:1702.04660v1* (2017).

- [33] F. BIRCH. "Elasticity and constitution of the Earth's interior." *J. Geophys. Res.*, **57**(2), 227–286 (1952).
- [34] B.K. GODWAL, S.K. SIKKA AND R. CHIDAMBARAM. *PHYSICS REPORTS (Review Section of Physics Letters)*, **102**, 121–197 (1983).
- [35] J. H. ROSE, J. R. SMITH, F. GUINEA AND J. FERRANTE. *Physical Review B*, **29**, 2963 (1984).
- [36] P. VINET, J. R. SMITH, J. FERRANTE AND J. H. ROSE. "Temperature effects on the universal equation of state of solids." *Physical Review B*, **35**(4), 1945–1953 (1987).
- [37] P. VINET, J. H. ROSE, J. FERRANTE AND J. R. SMITH. "Universal features of the equation of state of solids." *J. Phys. Condens. Matter*, **1**(11), 1941–1964 (1989).
- [38] S.K. SIKKA. *Physics Letters A*, **135**, 129 (1989).
- [39] CHEN LI-RONG AND CHEN QING-HU. *J. Phys.: Condens. Matter*, **3**, 775–780 (1991).
- [40] G. PARSAFAR AND E. A. MASON. *Physical Review B*, **49**, 3049 (1994).
- [41] J. HAMA AND K. SUITO. "The search for a universal equation of state correct up to very high pressures." *J. Phys. Condens. Matter*, **8**(1), 67–81 (1996).
- [42] W B HOLZAPFEL. *Rep. Prog. Phys.*, **59**, 29–90 (1996).
- [43] J. SHANKER, S.S. KUSHWAH AND M.P. SHARMA. *Physica B*, **271**, 158–164 (1999).
- [44] S.K. SAXENA. *Journal of Physics and Chemistry of Solids*, **65**, 1561–1563 (2004).
- [45] P. B. ROY AND S. B. ROY. *Physica B*, **350**, 375–388 (2004).
- [46] R.M. MORE, K. H. WARREN, D.A. YOUNG AND G.B. ZIMMERMAN. *Phys. Fluids*, **31**, 3059 (1988).
- [47] J.D. JOHNSON. *High Pressure Research*, **6**, 277 (1991).
- [48] W.H. HOOVER, G. STELL, E. GOLDMARK AND G.D. DEGANI. *J. Chem. Phys.*, **63**, 5434 (1975).
- [49] D. YOUNG. *A Soft Sphere Model for Liquid Metals*, UCRL-52353 (1977).
- [50] L.H. THOMAS. *Proc. Camb. Phil. Soc.*, **23**, 542 (1927).
- [51] E. FERMI. *Zeits.f. Phys.*, **48**, 73 (1928).

- [52] SHALOM ELIEZER, AJOY GHATAK AND HEINRICH HORA. *Fundamentals of Equations of State* (World Scientific Publishing Co. Pte. Ltd, 2002).
- [53] D.J. MCCLOSKEY. *An analytic formulation of Equations of state, Memorandum RM-3905-PR* (1964).
- [54] J. J. GILVARRY. *PHYSICAL REVIEW*, **96**(4), 934 (1954).
- [55] R. LATTER. *Phys. Rev.*, **99**, 1854 (1955).
- [56] K. K. KRUPNIKOV, M. I. BRAZHNIK, AND V. P. KRUPNIKOVA. *Sov. Phys. JETP*, **15**, 470 (1962).
- [57] S. B. KORMER, A. I. FUNTIKOV, V. D. URLIN, AND A. N. KOLESNIKOVA. "Dynamic compression of porous metals and the equation of state with variable specific heat at high temperatures." *Sov. Phys. JETP*, **15**(3), 477–488 (1962).
- [58] L. DAVISON. *Fundamentals of shock wave propagation in solids* (Springer-Verlag, Berlin, Heidelberg, 2008).
- [59] JEROME B. JOHNSON. "Simple model of shock-wave attenuation in snow". *Journal of Glaciology*, **37**(127), 303–312 (1991).
- [60] J. C. SLATER. *Introduction to Chemical Physics* (McGraw-Hill, New York, 1939).
- [61] J. S. DUGDALE, K. C. MACDONALD. "The Thermal Expansion of Solids". *Phys. Rev.*, **89**, 832 (1953).
- [62] V. YA. VASHCHENKO, V. N. ZUBAREV. "Concerning the Gruneisen Constant". *Sov. Phys. Solid State*, **5**, 653 (1963).
- [63] R.F. TRUNIN. *Shock Compression of Condensed Materials* (Cambridge university press, 1998).
- [64] K.H. OH AND P. A. PERSSON. *J. Appl. Phys.*, **65**, 3852 (1989).
- [65] J.B. JOHNSON. *J. Appl. Phys.*, **78**, 4300 (1995).
- [66] Q. WU AND F. JING. "Thermodynamic equation of state and application to Hugoniot predictions for porous materials." *J. Appl. Phys.*, **80**(8), 4343–4349 (1996).
- [67] M.H. RICE AND J.M. WALSH. "Equation of State of Water to 250 Kilobars." *J. Chem. Phys.*, **26**, 824–830 (1957).
- [68] L. BOSHOFF-MOSTERT AND H. J. VILJOEN. "Comparative study of analytical methods for Hugoniot curves of porous materials." *J. Appl. Phys.*, **86**(3), 1245–1254 (1999).

- [69] GENG HUAYUN, WU QIANG, TAN HUA, CAI LINGCANG, AND JING FUQIAN. *J. Appl. Phys.*, **92**, 5917 (2002).
- [70] GENG HUAYUN, WU QIANG, TAN HUA, CAI LINGCANG, AND JING FUQIAN. *J. Appl. Phys.*, **92**, 5924 (2002).
- [71] L.G. BOLKHOVITINOV AND YU.B. KHVOSTOV. *Nature*, **274**, 882 (1978).
- [72] T. HATANO. *Phys. Rev. Lett.*, **92**, 015503–1 (2004).
- [73] L. SOULARD, N. PINEAU, J. CLEROUIN AND L. COLOMBET. *J. Appl. Phys.*, **117**, 115901 (2015).
- [74] B.L. HOLIAN, T.C. GERMANN, J.B. MAILLET, C.T. WHITE. *Phys. Rev. Lett.*, **89**, 285501–1 (2002).
- [75] K. NAGAYAMA AND S. KUBOTA. *J. Phys. Cond. Matt. Conf. Series.*, **500**, 052032 (2014).
- [76] X.F. ZHANG, L. QIAO, A.S. SHI, J. ZHANG AND Z.W. GUAN. “A cold energy mixture theory for the equation of state in solid and porous metal mixtures”. *J. Appl. Phys.*, **110**(1), 013506–1–013506–10 (2011).
- [77] Q. ZHOU, P. CHEN, D. MA AND K. DAI. *J. Appl. Phys.*, **114**, 023509 (2013).
- [78] D. GRADY, G. FENTON AND T. VOGLER. *The 12th Hypervelocity Impact Symposium, Procedia Engineering*, **58**, 110 (2013).
- [79] G. FENTON, D. GRADY AND T.J. VOGLER. *The 12th Hypervelocity Impact Symposium, Procedia Engineering*, **58**, 724 (2013).
- [80] J.R. ASAY AND D.B. HAYES. *J. Appl. Phys.*, **46**, 4789 (1975).
- [81] J.M. WALSH AND R.H. CHRISTIAN. “Equation of State of Metals from Shock Wave Measurements.” *Phys. Rev.*, **97**(6), 1544–1556 (1955).
- [82] K. NAGAYAMA. *J. Phys. Soc. Japan*, **63**, 3737 (1994).
- [83] G.I. KERLEY. *User’s Manual for PANDA II- A Computer Code for Calculating Equation of State, Sandia Report, SAND88-229.UC-405* (1991).
- [84] Y. WANG, A. AHUJA, B. JOHANSSON. *Shock Compression of Condensed Matter -2001, edited by M.D. Furnish, N.N. thadhani and Y. Horie (AIP, 0-7354-0068-7/02)*, p. 67 (2002).
- [85] L. V. AL’ TSHULER, S. B. KORMER, A. A. BAKANOVA, AND R. F. TRUNIN. *SOVIET PHYSICS JETP*, **11**(3), 573 (1960).
- [86] A.K. KAPILA, R. MENIKOFF, J.B. BDZIL, S.F. SON AND D.S. STEWART. “Two-phase modeling of deflagration-to-detonation transition in granular materials: Reduced equations.” *Phys. Fluids*, **13**, 3002–3024 (2001).

- [87] G.E. DUVALL AND S.M. TAYLOR. "Shock parameters in a two component mixture." *J. Composite Materials*, **5**(2), 130–139 (1971).
- [88] B.R. KRUEGER AND T. VREELAND. "A Hugoniot theory for solid and powder mixtures." *J. Appl. Phys.*, **69**(2), 710–716 (1991).
- [89] S.L. GAVRILYUK AND R. SAUREL. "Rankine-Hugoniot relations for shocks in heterogeneous mixtures." *J. Fluid Mech.*, **575**(1), 495–507 (2007).
- [90] A.N. DREMIN AND I.A. KARPUKHIN. "Method of determination of shock adiabat of the dispersed substances." *Zhurnal Prikladnoi Mekhaniki i Tekhnicheskoi Fiziki (in Russian)*, **1**(3), 184–188 (1960).
- [91] YU.F. ALEKSEEV, L.V. AL'TSHULER AND V.P. KRUPNIKOVA. "Shock compression of two-component paraffin-tungsten mixtures." *J. Appl. Mech. Tech. Phys.*, **12**(4), 624–627 (1971).
- [92] R. SAUREL, O. LE METAYER, J. MASSONI AND S. GAVRILYUK. "Shock jump relations for multiphase mixtures with stiff mechanical relaxation." *Shock Waves.*, **16**(3), 209–232 (2007).
- [93] R.G. MCQUEEN, S.P. MARSH, J.W. TAYLOR, J.N. FRITZ AND W.J. CARTER. *High Velocity Impact Phenomena*. edited by R. Kinslow (Academic, New York, 1970).
- [94] S.S. BATSANOV. *Effects of Explosions on Materials: Modification and Synthesis Under High-Pressure Shock Compression*. (Springer, Berlin, 1994).
- [95] O.E. PETEL AND F.X. JETTE. "Comparison of methods for calculating the shock hugoniot of mixtures." *Shock Waves.*, **20**, 73–83 (2010).
- [96] X.F. ZHANG, A.S. SHI, J. ZHANG, L. QIAO, Y. HE AND Z.W. GUAN. "Thermochemical modeling of temperature controlled shock-induced chemical reactions in multifunctional energetic structural materials under shock compression." *J. Appl. Phys.*, **111**(12), 123501–1–123501–9 (2012).
- [97] D.A. YOUNG, E.M. COREY. "A new global equation of state for hot, dense matter." *J. Appl. Phys.*, **78**(6), 3748–3755 (1995).
- [98] J.L. JORDAN, D. DATTELBAUM, L. FERRANTI, G. SUTHERLAND, M. BAER, W. RICHARDS, S. SHEFFIELD, R.D. DICK AND N.N. THADHANI. *AIP Conf. Proceedings*, **1195**, 1253 (2009).
- [99] R.E. SETCHELL AND M.U. ANDERSON. *J. Appl. Phys.*, **97**, 083518 (2005).
- [100] R.E. SETCHELL, M.U. ANDERSON AND S.T. MONTGOMERY. *J. Appl. Phys.*, **101**, 083527 (2007).
- [101] J.C.F. MILLETT, N.K. BOURENE AND D. DEAS. *J. Phys. D: Appl. Phys.*, **38**, 930 (2005).

- [102] J.L. JORDAN, L. FERRANTI, R.A. AUSTIN, R.D. DICK, J.R. FOLEY, N.N. THADHANI, D.L. MCDOWELL AND D.J. BENSON. *J. Appl. Phys.*, **101**, 093520 (2007).
- [103] J.L. JORDAN, D. DATTELBAUM, G. SUTHERLAND, D.W. RICHARDS, S.A. SHEFFIELD, AND R.D. DICK. *J. Appl. Phys.*, **107**, 103528 (2010).
- [104] G.A. COX AND J.R. MAW. *J. Phys.: Conference Series.*, **500**, 142007 (2014).
- [105] A.D. RESNYANSKY. *Phys. Rev. B*, **93**, 054103 (2016).
- [106] B. NAYAK, S.V.G. MENON. *Shock Waves*, DOI 10.1007/s00193-017-0717-9.
- [107] B. NAYAK, S.V.G. MENON. *AIP Advances*, **7**, 045113 (2017).
- [108] P.R. LEVASHOV, V.E. FORTOV, K.V. KHISHCHENKO AND I.V. LOMONOSOV. *Shock Compression of Condensed Matter-1999*, Ed. M.D. Furnish, L.C. Chhabildas and R.S. Hixson, **89** (2000).
- [109] K.S. HA, H.Y. JEONG, Y.M. KWON, W.P. CHANG, D.H. HAHN AND Y.B. LEE. *Transactions of Korean Nuclear Society Spring Meeting, Chuncheon, Korea, May 25-26*. (2006).
- [110] P.R. LEVASHOV, V.E. FORTOV, K.V. KHISHCHENKO AND I.V. LOMONOSOV. *Shock Compression of Condensed Matter-2001*, Ed. M.D. Furnish, N.N. Thadhani and Y. Horie, **71** (2002).
- [111] J.W. SHANER. *High Pressure Research*, **4**, 561 (1990).
- [112] T.R. MATTSSON AND M.P. DESJARLAIS. *Equation of state and electrical conductivity of stainless steel*, SAND-2004-5253 (2004).
- [113] R. FURTH. *Proc. Roy. Soc.*, **A183**, 87 (1944).
- [114] H. ZHEN AND G.J. DAVIES. *Phys. Stat. Solidi (a)*, **78**, 595 (1983).
- [115] SUN JIUXUN. *J. Phys., Cond. Matt.*, **17**, L 103 (2005).
- [116] F.D. STACEY. *Rep. Prog. Phys.*, **68**, 341 (2005).
- [117] STANLEY MINSHALL. "Properties of Elastic and Plastic Waves Determined by Pin Contactors and Crystals." *J. Appl. Phys.*, **26**, 463–469 (1955).
- [118] M. H. RICE. "Capacitor Technique for Measuring the Velocity of a Plane Conducting Surface." *Rev. Sci. Instrum.*, **32**, 449–451 (1961).
- [119] R. A. GRAHAM, F. W. NEILSON AND W. B. BENEDICK. "Piezoelectric Current from Shock-Loaded Quartz.—A Submicrosecond Stress Gauge." *J. Appl. Phys.*, **36**, 1775–1783 (1965).

- [120] G. E. INGRAM AND R. A. GRAHAM. "Quartz Gauge Technique for Impact Experiments." *On Detonation, Pasadena, California, August 1970 (Office of Naval Research ACR-184)*, pp. 369–386 (1970).
- [121] P. J. A. FULLER AND J. H. PRICE. "Electrical Conductivity of Manganin and Iron at High Pressures." *Nature*, **193**, 262–263 (1962).
- [122] J. N. FRITZ AND J. A. MORGAN. "An Electromagnetic Technique for Measuring Material Velocity." *Rev. Sci. Instrum.*, **44**, 215–221 (1973).
- [123] J. A. MORGAN AND J. N. FRITZ. "Sound Velocity on SiO₂, Hugoniot". *High Pressure Science and Technology*, K. D. Timmerhaus and M. S. Barber, Eds., *Metallurgical Society Conferences, Boulder, Colorado, July 25-29*, **Vol. 2**, 109–117 (1977).
- [124] B. HAYES AND J. N. FRITZ. "Measurement of Mass Motion in Detonation Products by an Axially Symmetric Electromagnetic Technique". *Fifth Symposium (International) on Detonation, Pasadena, California, August (Office of Naval Research ACR-184, 1970)*, pp. 447–454 (1970).
- [125] W. C. DAVIS. "Magnetic Probe Measurements of Particle Velocity Profiles". *Sixth Symposium (International) on Detonation, Coronado, California, August 24-27. (Office of Naval Research ACR-221, 1976)*, pp. 637–641 (1976).
- [126] YA.B. ZEL'OVICH AND YU. P. RAIZER. *Physics of Shock waves and High-Temperature Hydrodynamic Phenomena*, vol. volume-I (Academic press, New York, 1966).
- [127] J. P. BORIS, A. M. LANDSBERG, E. S. ORAN AND J. H. GARDNER. *LCPFCT: Flux-Corrected Transport Algorithm for Solving Generalized Continuity Equations* (NRL/MR/6410-93-7192, NAVAL RESEARCH LABORATORY, 1993).
- [128] PHILIP L. BROWNE. *Derivation of the Equations of Conservation of Mass, Momentum and Energy of Compressible Fluid Mechanics in both Lagrangian and Eulerian forms from an Integral viewpoint* (LA-10588-MS, Los Alamos National Laboratory, 1986).
- [129] L. D. LANDAU AND E.M. LIFSHITZ. *Fluid Mechanics* (Pergamon Press, New York, 1987).
- [130] J. VONNEUMANN AND R. D. RICHTMYER. "A Method for the Numerical Calculation of Hydrodynamic Shocks." *J. Appl. Phys.*, **21**, 232–237 (1950).
- [131] J. P. BORIS AND D. L. BOOK. "Flux-corrected transport. I. SHASTA, a fluid transport algorithm that works." *J. Comput. Phys.*, **11**, 38–69 (1973).
- [132] J. P. BORIS AND D. L. BOOK. "Solution of Continuity Equations by the Method of Flux-Corrected Transport." *Methods in Computational Physics.*, **16**, 85–129 (1976).

- [133] J. P. BORIS AND D. L. BOOK. "Flux-corrected transport. III. Minimal-error FCT algorithms." *J. Comput. Phys.*, **20**, 397–431 (1976).
- [134] D. L. BOOK, J. P. BORIS AND K HAIN. "Flux-corrected transport II: Generalizations of the method." *J. Comput. Phys.*, **18**, 248–293 (1975).
- [135] E. S. ORAN AND J. P. BORIS. *Numerical Simulation of Reactive Flow*, vol. Chapter 8 (Elsevier, New York, 1987).
- [136] F. MILINAZZO, Y. OVED, R.M. CLEMENTS AND P.R. SMY. "Blast wave computations using the flux-corrected transport algorithm". *J. Phys. D: Appl. Phys.*, **12**, 1039–1049 (1979).
- [137] Zs. REGALY. "General Purpose Hydrodynamic Code". <https://www.researchgate.net/publication/252273922>. (2004).
- [138] D.A. JONES, G. KEMISTER AND R.A.J. BORG. "Numerical Simulation of Detonation in Condensed Phase Explosives". *DSTO-TR-0705, Aeronautical and Maritime Research Laboratory AR-010-605* (1998).
- [139] V. G. SHCHETININ. "Calculation of the state parameters of condensed substances at high pressures and temperatures". *Combustion, Explosion and Shock Waves*, **27**(4), 426–432 (1991).
- [140] M. A. MEYER. *DYNAMIC BEHAVIOR OF MATERIALS* (WILEY-INTERSCIENCE PUBLICATION, New York, 1994).
- [141] G. E. DUVALL AND G. R. FOWLES. *High Pressure Physics and Chemistry*, vol. Vol. 2 (Academic Press, New York, 1963).